Fakultät für Luftfahrt, Raumfahrt und Geodäsie (LRG)

Exploit satellite altimetry to improve coastal tide estimation

Gaia Piccioni

Vollständiger Abdruck der von der Fakultät für Luftfahrt, Raumfahrt und Geodäsie der Technischen Universität München zur Erlangung des akademischen Grades eines

Doktor-Ingenieurs (Dr.-Ing.)

genehmigten Dissertation.

Vorsitzender:

Prof. Dr.-Ing. Uwe Stilla

Prüfende der Dissertation:

1. Prof. Dr.-Ing. Florian Seitz
2. Prof. Dr. Ole Baltazar Andersen

Die Dissertation wurde am 28.05.2020 bei der Technischen Universität München eingereicht und durch die Fakultät für Luftfahrt, Raumfahrt und Geodäsie am 25.01.2021 angenommen.

Abstract

The combination of high tides with extreme sea level events jeopardizes our coasts and our society. Therefore, the ability to model and predict ocean tides is crucial for coastal management. Despite the latest striking improvements, the coast still remains a challenging zone for tide modeling. Satellite altimetry data play a key role in ocean tidal estimation, as they provide precise information on sea level, which is regularly integrated in most of the modern tide models, dramatically enhancing their performance. Coastal regions are challenging environments for satellite altimetry as well, however the recent large efforts in these areas brought to the development of several dedicated altimetric products, which improved sea level estimations up to few kilometers from the shore. The purpose of this thesis is to illustrate the work done to update the DGFI-TUM's EOT11a ocean tide model, with specific focus on accuracy improvement at coastal areas. For this reason, the latest altimetric products dedicated to coastal applications are exploited, such as the ALES retracker. The potential of coastal altimetry to improve tidal estimates is tested in a specific study that shows that the use of ALES along track can reduce errors on individual tidal constituents of more than 2 cm at single tide gauge sites. The updated EOT model, the EOT19p, is derived using 27 years of altimetry data and it is based on a multi-mission weighted least-squares approach. EOT19p is currently available on limited regions, and the assessment against in situ data shows an improvement of 35.39% in the North Sea, and 20.07% in the Malay Archipelago with respect to EOT11a, and the lowest median absolute differences occur for single tidal constituents against the state-of-the-art tide models.

Acknowledgements

Someone once told me that writing a PhD thesis is nothing else than "write the story of your research of the last three years". In a few pages you will read about it, but before that, I would like to specify that a PhD research is not only made of calculations, scripts, and failed experiments, but also of cooperation between people. Therefore, I hereby want to thank all people who contributed to mine.

First of all, thanks to my supervisor Florian Seitz, who gave me the possibility to work on this interesting project. He has been supportive and flexible in all my choices, giving helpful and practical advices that facilitated my research and my employment at DGFI-TUM.

I am really grateful to my mentor Denise Dettmering, who has been my reference point in this work. She has always been ready for advice or opinion exchange, improving dramatically the quality of my work, and making me grow technically and professionally.

My first contact with tides wouldn't have been so smooth without the fundamental help of Wolfgang Bosch, who shared his experience and contributed to my research with suggestions and constructive criticism also during his retirement.

Particularly helpful for me during all my PhD was Christian Schwatke, who is an exceptional researcher and programmer and the backbone of DGFI-TUM OpenADB Toolbox (and beyond). He managed to teach me a new programmming language, a bit of computer science, and he heavily contributed to my work with his knowledge of in-house datasets and functions.

I want to thank the (coastal) altimetry and tides communities, who gave me the enthusiasm to continue this research, and from whom I learnt a lot during dedicated conferences and workshops. In particular, I am grateful to Richard Ray and Philip Woodworth, who encouraged my work and gave me fruitful advices.

Special thanks go to Jérôme Benveniste, for his motivational speech about my PhD; it was really what I needed to start writing this thesis!

My deepest gratitude goes to Marcello Passaro, who is a bright young researcher, and the person who directly and indirectly taught me most. As a colleague, office mate, and friend, he showed me how to think critically, the power of networking, the curiosity towards new research frontiers, and the struggle to be a young researcher. He shared his knowledge about

oceanography and altimetry, and we learnt together new things - and new German words - showing that the best way to do research is to remain humble and curious.
Finally, a big thank you goes to DGFI-TUM colleagues and ex-colleagues, who warmly welcomed me in the group, and became supportive and affectionate friends.

Preface

During these three years, I published three peer-reviewed papers as first author in collaboration with other colleagues. Part of them (text, figures, and tables) are rewritten in this this thesis. The same has been done with part of the texts I wrote in the frame of the DFG-funded TIDUS project - in which I was shortly involved - and the OpenADB website - for which I wrote a short description of about the altimetric missions.
Different colored symbols indicate the beginning and the end of the text belonging to the single articles. In particular:

- ●: Piccioni G., Dettmering D., Passaro M., Schwatke C., Bosch W., Seitz, F. (2018) Coastal Improvements for Tide Models: The Impact of ALES Retracker. Remote Sens., 10, 700. *doi:10.3390/rs10050700*.
- ▲: Piccioni G., Dettmering D., Bosch W., Seitz, F. (2019) TICON: TIdal CONstants based on GESLA sea-level records from globally located tide gauges. Geosci. Data J.; 00:1-8. *https://doi.org/10.1002/gdj3.72*.
- ■: Piccioni G., Dettmering D., Schwatke C., Passaro M., Seitz F. (2019) Design and regional assessment of an empirical tidal model based on FES2014 and coastal altimetry, Advances in Space Research. *https://doi.org/10.1016/j.asr.2019.08.030*.

Contents

Acknowledgements **iii**

Preface **v**

1 Introduction **1**

2 Ocean tides **4**

2.1 Tide generating potential and Equilibrium Tide 4

2.2 Tidal constituents as periodic signals 7

2.2.1 Astronomical arguments 9

2.2.2 Nodal corrections 10

2.3 Methods of tidal estimation 11

2.3.1 Harmonic method 12

2.3.2 Response method 12

2.3.3 Laplace tidal equations 14

2.4 State of the art of ocean tide models 15

3 Sea level from satellite altimetry **21**

3.1 The basic principle of radar altimetry 21

3.2 From range to sea level 23

3.2.1 Range 24

3.2.2 Dry troposperic correction 25

3.2.3 Wet troposperic correction 26

3.2.4 Ionospheric correction 26

3.2.5 Dynamic Atmospheric correction 27

3.2.6 Ocean tide correction 27

3.2.7 Load tide correction 27

3.2.8 Solid Earth and Polar tide correction 28

3.2.9 Sea State Bias 28

3.2.10 Mean Sea Surface 29

3.3 Issues at the coast . . . 29
3.4 Altimetry missions . . . 33
3.5 Monitoring tides with altimetry . . . 35

4 The creation of an improved tidal model 40
4.1 SLA collection and weighting . . . 41
4.1.1 SLA data . . . 41
4.1.2 SLA weighting . . . 41
4.2 The method of weighted least squares (WLS) . . . 44
4.3 Reconstruction of full tidal signal . . . 49
4.4 The error of the fit . . . 51
4.5 Additional studies . . . 54
4.5.1 The cap size choice: innovative failures . . . 54
4.5.2 Focus on the coast: the along-track test . . . 56

5 Validation: data and methods 59
5.1 Evaluation methods . . . 59
5.2 Construction of a validation dataset . . . 60
5.2.1 TICON . . . 60
5.2.2 TICON validation . . . 68
5.2.3 The complete DGFI-TUM in situ dataset . . . 68

6 Results and discussion 72
6.1 Comparison of global models . . . 72
6.2 Regional analysis of EOT19p model . . . 77
6.2.1 Tidal elevation differences . . . 77
6.2.2 Comparison against in situ data . . . 78
6.3 Additional studies . . . 83
6.3.1 The along-track test . . . 83
6.3.2 Tests with alternative cap size choice . . . 91

7 Conclusion and future work 93
7.1 Conclusion . . . 93
7.2 Future work . . . 94

Appendix A 97

Bibliography 98

List of Figures

2.1 The Earth-Moon system. 5
2.2 Scheme of displacement of equilibrium water surface related to tide-generating force and the normal of the Earth's gravity force. 7
2.3 M2 18.61-year amplitude modulation at Newlyn station. 11
2.4 Amplitude of M2 tidal constituent, from FES2014 model. 17
2.5 Phase of M2 tidal constituent, from FES2014 model. 18

3.1 Design of radar footprints. 22
3.2 Pulse-limited footprint at different times. 22
3.3 Sketch of fundamental geophysical heights in altmetry. 24
3.4 Altimeter measurement principle. Credit: `https://www.aviso.altimetry.fr/en/techniques/altimetry/principle/pulses-and-waveforms.html`. . 24
3.5 Ideal Brown ocean waveform. 25
3.6 FES2014 ocean tide correction for cycle 40 of Jason-1 mission. 28
3.7 Scheme of altimetric observation in proximity of the coast. 30
3.8 Waveforms at coastal areas observed with ERS-2 mission. 31
3.9 Percentage of Jason-1 cycles with ≥ 0.9 correlation with tide gauges. 31
3.10 Timeline of altimetry missions available from OpenADB. 35
3.11 Example of altimetry track coverage Around the Equator. 36
3.12 Schematic of signal shift between the first sample at t_1 and the second sample at t_2. 37
3.13 Example of aliased signal. 37

4.1 Distribution of grid nodes for a regular grid of 1/4 degree resolution and a grid based on the geodesic polyhedron, used to derive EOT19p. 42
4.2 Grid node with SLA Gaussian weighting representation using the radius at the Equator of 165 km. 43
4.3 Flowchart of VCE iteration. 49
4.4 Weights of Jason-1 mission according to VCE in percentage. Credit: Piccioni et al., 2019b. 50

4.5 Weights in percentage for Jason-1 against distance to coast. 50
4.6 Visual comparison between the internal error σ_0 (in cm) of the weighted least squares and the bathymetry map of the North Sea. 55
4.7 The internal error σ_0 plotted against ocean depth, with zoom on depths below 400 m. 56
4.8 Number of observations of Jason-series missions plotted against depth in the North Sea. 56
4.9 Comparison between σ_0 values obtained with fixed cap size and the ones computed with depth-dependent cap size. 57
4.10 Schemes of the algorithm and wanted result of selective mask. 57
4.11 Results of selective cap in the North Sea. 58

5.1 Overview of the length (in years) of the GESLA time series 61
5.2 Overview of missing data in GESLA records 61
5.3 Difference of timeseries length before and after flagging rejection. 62
5.4 Overview of missing data in GESLA records after removing the flagged data. 63
5.5 Percentage of missing data plotted against the time series length. 63
5.6 Geographical distribution of TICON data. 64
5.7 Geographical distribution of RSS differences between TICON and FES2014 for 923 tide gauges. 70
5.8 RSS differences between TICON and FES2014 for tide gauges located in the North Sea. 71
5.9 RSS differences between TICON and FES2014 for tide gauges located in the Malay Archipelago. 71

6.1 SD of major tidal constituents from semi-empirical and assimilative hydrodynamic models. 74
6.2 SD of M2 and K1 tidal constituents from semi-empirical and assimilative hydrodynamic models, OSU12 excluded. 75
6.3 SD of M2 and K1 tidal constituents from semi-empirical and assimilative hydrodynamic models, OSU12 and DTU16 excluded. 75
6.4 SD of M2 tidal constituent between STORMTIDE, HIM, and HYCOM models. 76
6.5 SD2014 and SD2019 for M2 tidal constituent over North Sea. 78
6.6 SD2014 and SD2019 for M2 tidal constituent over the Malay Archipelago. . . 79
6.7 SD2014 and SD2019 averaged values with respect to distance to coast for M2 tidal constituent, in the North Sea and in the Malay Archipelago. 79
6.8 RSS relative improvement of EOT19p with respect to EOT11a at single in situ stations in the North Sea. 81

6.9 RSS relative improvement of EOT19p with respect to EOT11a at single in situ stations in the Malay Archipelago. 81
6.10 Difference in the number of observations between ALES and SGDR at each node against the distance to coast. 84
6.11 Difference of σ_0 values between SGDR minus ALES at each node against the distance to coast, and against difference in number of observations between ALES and SGDR. 85
6.12 Geographical distribution of the ΔRSS (in cm) for the closest nodes to the tide gauge of interest. 86
6.13 Difference of RMS for major constituents at the CNTG. 87
6.14 Difference of RSS against distance to coast and the closest tide gauge of interest. 88
6.15 Absolute ΔRMS of major constituents at the CNTG against the distance to coast. 89
6.16 RMS values for M2 constituent computed with ALES solutions for tracks 111 (ascending) and 92 (descending). 91
6.17 ΔRSS absolute values for the closest node to the tide gauge against the sea state. 92
6.18 ΔRSS values at in situ stations for $EOT_{FC} - EOT11a$, $EOT_{VC} - EOT11a$, and $EOT_{SM} - EOT11a$. 92

List of Tables

2.1 Mass and distances of Earth, Moon and Sun. 6
2.2 Examples of nodal corrections for main constituents. 11

3.1 Time variability of geophysical corrections in open ocean and at the coast. . . 33
3.2 Aliasing periods of main tidal constituents for Jason- and ERS-type missions in days. 38
3.3 Rayleigh periods of main tidal constituents for Jason-type mission in days. . . 38

4.1 List of corrections used to compute SLA for tidal estimation residuals. 42

5.1 Part of the TICON dataset for the station of Port Angeles, Washington, USA. 67
5.2 RMS and RSS differences between TICON and FES2014 averaged on 923 tide gauges. 69
5.3 RMS and RSS differences between TICON and FES2014 averaged for tide gauges in the Malay Archipelago. 69

6.1 Global SD of modern models in cm, with OSU12 and without OSU12. 75
6.2 Comparison of SD2014 and SD2019 in the North Sea. 79
6.3 Comparison of SD2014 and SD2019 in the Malay Archipelago. 80
6.4 Comparison of MAD for EOT19p and EOT11a in the North Sea. 82
6.5 Comparison of MAD for EOT19p and EOT11a in the Malay Archipelago. . . 82
6.6 MAD comparison between existing models in the North Sea. Values are in cm. 83
6.7 MAD comparison between existing models in the Malay Archipelago. Values are in cm. 84
6.8 Average of RMS for major constituents for the closest points to the tide gauges. 86
6.9 Average of RMS computed for major constituents at the closest points to the tide gauges, after dividing the tracks according to their position with respect to the coast. 90
6.10 Comparison of RMS and RSS values of EOT_{FC}, EOT_{VC}, and EOT_{SM} results with $EOT11a$ and $FES2014$ models in Bristol Channel area. Results in cm. . 92

Chapter 1

Introduction

Ocean tides are a phenomenon familiar to many. They can be generally defined as periodic oscillations of sea level, caused by the gravitational attraction between the Earth and the Sun and Moon. These oscillations are characterized by different amplitudes and phases according to their location in the world. Tides are severely affected by the ocean bottom topography and coastal geometry, and therefore the description of their movements is more complex than its standard definition. The first mathematical descriptions of ocean tides were formulated in the first half of the XVIII century by Bernoulli, MacLaurin, and Euler, who based their theories on Newton's gravitation law, developed fifty years earlier (Treccani, 2017). With its static theory of tides, also called the *Equilibrium theory*, Bernoulli associated the Earth to a perfect sphere, and its deformation due to tides as a prolate spheroid, and he provided the first predictions of tides in ports with predominant semi-diurnal phenomena (Cartwright, 1999). The introduction of fluid dynamics by Laplace in the late XVIII century made the description of tides more sophisticated. Nowadays, hydrodynamic tide models are still based on Laplace's differential equations of tides. Another approach to derive tidal parameters is the harmonic analysis of sea level timeseries, introduced by Lord Kelvin in the XIX century, and further extended by Darwin, 1899 and Doodson, 1921. Tides are described by sinusoids that are associated to a linear function of astronomical frequencies, that change according to the time of their observation. In 1966 an alternative concept has revolutionised tidal computation: Munk and Cartwright, 1966 theorised that the response of the ocean to gravity is a slow-varying function that allows to describe tidal movements of similar frequencies with a single function.

With the advent of satellites in the XX century, the description of tides further improved, as they allow regularly sampled observations in space and time, with a quasi-global coverage. The harmonic analysis and the responsive method are applied to satellite observations to derive another tide model category: the so-called empirical or semi-empirical models. With satellite onboard altimeters it is possible to observe the sea level with an accuracy

of few centimeters (Bonnefond et al., 2011), and it has been shown that since 1992 (which corresponds to the launch of TOPEX/Poseidon, the first long-lived altimetry mission with an unprecedented accuracy for sea-level measurements) tide models got an enhancement of approximately 5 cm over the previous models (Shum et al., 1997). Tide models represent a critical feature for altimetry itself, as altimetric measurements need to be corrected for tidal signal in order to separate the tidal-related variability of sea level from the anomalies coming from the ocean dynamic topography. Therefore, more accurate tide models result in more reliable altimetric sea level retrievals.

But above all, the ability to predict tides represents a crucial matter for our society. Millions of people live and work at the coast, and are everyday exposed to hazards coming from the sea. In certain regions, tidal events combined with extreme meteorological conditions are responsible for severe flooding and consequent safety and environmental issues. At present, ocean tide models have a high performance in open ocean, while at coastal and shallow areas significant errors are still found, as the complexity of bathymetry and littoral geometries remain still a challenge. Large efforts focused on improving tide description in these areas have been made throughout the last decade, and brought a dramatic progress for shallow-water tides, with a consequent larger agreement among different models, and a clear improvement on the single tidal constituents. However, a lower performance is still observed at the coast, resulting in large discrepancies between models and in situ observations. For models assimilating satellite measurements, such situation may be due to a poor availability and quality of altimetric data, that are also highly influenced by the presence of land (Gommenginger et al., 2011), patches of water at very low sea state within the altimeter footprint (Passaro et al., 2014), or ice, at higher latitudes (Andersen and Piccioni, 2016). In these areas, the returned altimetry echo assumes shapes that are considerably different from the typical open ocean radar return, and therefore the signal needs to be fitted with a dedicated algorithm (called retracker). With the exploitation of these recent advances in data pre-processing, dedicated coastal products are now available and are able to improve sea level estimations up to few kilometers from the shore (Cipollini et al., 2017).

In this thesis it is illustrated the research carried out by the author throughout the last three years, which was aimed to update and improve the DGFI-TUM's Empirical Ocean Tide (EOT) model with respect to its latest version EOT11a. The version derived in this thesis is called EOT19p where p stands for preliminary. In EOT11a information from a hydrodynamic model is combined with tidal estimates obtained through harmonic analysis of multi-mission altimetric data. EOT11a is known to have high performance on a global scale, but showed still issues in shelf and coastal waters (Savcenko and Bosch, 2012). It became a natural consequence to focus this research on such critical regions, and study the impact of coastal altimetric data on tidal estimates. So, this work have been summarized

in three main research questions:

- What is the impact of altimetric coastal dedicated products on tidal estimates?
- Which alternative solutions to EOT11a algorithm focused on coastal tides are relevant in terms of computational-time and tidal-estimation performance?
- What is the performance of the best algorithm found with respect of in situ data, EOT11a and state-of-the-art models?

Structure of the dissertation

The thesis is divided in three main parts. The first one is dedicated to the theoretical background: in chapter 2, the mathematical principles behind ocean tides are illustrated, together with the methods for tide modeling and the state of the art of ocean tide models; chapter 3 describes the fundamentals of satellite altimetry, the way how the sea level is derived from altimetric measurements, the issues related to coastal observations, and the ones related to retrieve ocean tide signals. The second part is about the theoretical algorithms and considerations made to derive the EOT tide model and its validation routines. In particular, in chapter 4 the method used to derive the EOT model is explained in detail, and additional studies supporting the final version of the models are presented; chapter 5 shows how the validation dataset and methods were derived. In the last part, results are shown and discussed: in chapter 6, tide models are analysed and compared. The main section (6.2) regards the regional analysis of EOT model, however, results on additional studies, and the analysis of state-of-the-art global models are also included. Conclusions can be found in chapter 7.

Chapter 2

Ocean tides

Ocean tides are an effect of gravitational forces exerted between the Earth and other celestial bodies. The Sun and the Moon are the main responsible of tides on Earth, and cause sea level variations according to their position in the sky. These variations are the result of periodic phenomena, that can be described by sinusoidal signals and astronomical expressions. In this chapter the bases of ocean tides are illustrated, with highlights on the main expressions used nowadays in many tidal estimation algorithms. In section 2.1, the expression of Equilibrium tide is derived from the tide generating potential. The spherical harmonic expansion of the Equilibrium Tide is used to build the periodic signals that describe tidal movements; in order to understand how the Equilibrium tide is related to these signals, one example is given in section 2.2. Sections 2.1 and 2.2 are based on notes taken from (Pugh and Woodworth, 2014a), which is cited herein once, for an easier reading. Finally, in section 2.3, different methods for tidal estimation are listed and illustrated.

2.1 Tide generating potential and Equilibrium Tide

The principle behind ocean tides is the Newton's law of universal gravitation. A particle of mass m_1 attracts a particle of mass m_2 with a force that is directly proportional to the product of their masses, and inversely proportional to the square of their distance R:

$$F = G \cdot \frac{m_1 m_2}{R^2} \tag{2.1}$$

with G the gravitational constant of value $6.674 \cdot 10^{-11} m^3 \cdot kg^{-1} \cdot s^{-2}$. This principle can be extended to two celestial bodies, such as the Earth and the Moon, and whose distance is the distance between their center of mass. In figure 2.1 a sketch of the Earth-Moon system is shown, with O and Q the respective centers of mass, that correspond to the center of the celestial bodies for simplification. The tide-generating force is defined as differential force, as it corresponds to the difference between the force exerted on a point on the Earth's surface

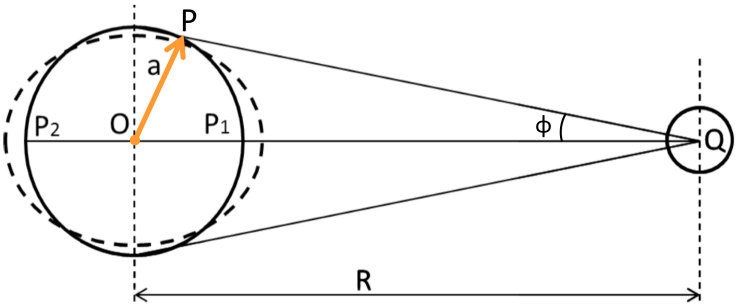

Figure 2.1: The Earth-Moon system.

and the force exerted at the center of the Earth (Doodson and Warburg, 1941). Therefore, the force exerted at point P1 can be expressed as):

$$F_{P1} = G \cdot m_1 m_2 \left[\frac{1}{(R-a)^2} - \frac{1}{R^2} \right] \tag{2.2}$$

$$F_{P1} = G \cdot \frac{m_1 m_2}{R^2} \left[\frac{1}{\frac{1}{R^2}(R-a)^2} - 1 \right] \tag{2.3}$$

$$F_{P1} = G \cdot \frac{m_1 m_2}{R^2} \left[\frac{1}{(1-\frac{a}{R})^2} - 1 \right] \tag{2.4}$$

And with $\frac{1}{(1-\frac{a}{R})^2} \sim 1 + 2\frac{a}{R}$ because a, the mean Earth Radius is circa 6371 km, which is very small with respect to the distance Earth-Moon R, of 384400 km:

$$F_{P1} = 2G \cdot \frac{m_1 m_2 a}{R^3} \tag{2.5}$$

The same formula can be used to calculate the tidal force at P2:

$$F_{P2} = G \cdot m_1 m_2 \left[\frac{1}{R^2} - \frac{1}{(R+a)^2} \right] \tag{2.6}$$

that results as the opposite force:

$$F_{P2} = -2G \cdot \frac{m_1 m_2 a}{R^3} \tag{2.7}$$

The same expressions can be applied to the system Earth-Sun. It is worth to mention that the gravitational effect of the Moon is around twice the one of the Sun. This can be easily checked by knowing the basic information about these celestial bodies (listed in table (2.1); for example, at P1 the tidal force due to the Moon is $6.57 \cdot 10^{18}$ N, which is 2.2 times larger than the one due to the Sun, with $F_{P1} = 3.02 \cdot 10^{18}$ N.

Tidal forces are also expressed in terms of gravitational potential, which is defined, as the work needed to attract a particle of unit mass located in P (figure 2.1) towards the Moon (with mass m_l) that has a distance $\overline{QP}$:

$$\Omega_P = -\frac{Gm_l}{\overline{QP}} = -\frac{Gm_l}{R^2} \left[1 - 2\frac{a}{R^2}\cos\phi + \frac{a^2}{R^2} \right]^{-\frac{1}{2}} \tag{2.8}$$

Datum	Value
Earth mass	$5.9722 \cdot 10^{24}$ kg
Moon mass	$7.35 \cdot 10^{22}$ kg
Sun mass	$1.9884 \cdot 10^{30}$ kg
Distance Earth-Moon	384400 km
Distance Earth-Sun	149600000 km

Table 2.1: Mass and distances of Earth, Moon and Sun.

being the term in square brackets the result of the cosine law to derive the distance $\overline{QP}$, divided by R^2. The location P forms an angle (the lunar angle, ϕ) with respect to the Earth-Moon line $\overline{OQ}$. The term in brackets can be expanded using the Legendre polynomials $P_1(\cos\phi) = \cos\phi$ and $P_2(\cos\phi) = \frac{1}{2}(3\cos^2\phi - 1)$:

$$\Omega_P = -\frac{Gm_l}{R^2}\left[1 + \frac{a}{R}P_1(\cos\phi) + \frac{a^3}{R^3}P_2(\cos\phi) + ...\right]^{-\frac{1}{2}} \tag{2.9}$$

(higher terms of the expansion are neglected because $\frac{a}{R} << 1$); ϕ depends on astronomical variables, that are the declination of the Moon, the latitude of P, and the hour angle of the Moon (respectively D_l, ϕ_P, and C_P):

$$\cos\phi = \sin\phi_P \sin D_l + \cos\phi_P \cos D_l \cos C_p \tag{2.10}$$

The tidal potential is used to derive the expression of the so-called Equilibrium Tide, that is defined as: the sea surface elevation due to tidal forces if the Earth were ideally covered by only water with a depth that allows instantaneous response. Despite its ideal condition, the Equilibrium Tide represents an important element to derive expressions needed in tidal analysis. The tidal force needed to move a particle of mass m towards the Moon can be expressed as the derivative of the potential along the x direction:

$$-m\frac{\delta\Omega_P}{\delta x} = mg\tan\alpha \tag{2.11}$$

where α is the angle of the force with respect to the gravity force that is normal to the Earth (see figure 2.2).

The displacement due to this force can be defined as $\frac{\delta\zeta}{\delta x} = \tan\alpha$, that can be equalized to 2.11:

$$\frac{\delta\Omega_P}{g\delta x} + \frac{\delta\zeta}{\delta x} = 0 \tag{2.12}$$

which is, integrating on a finite area whose volume is conserved:

$$\zeta = -\frac{\Omega_P}{g} = \frac{Gm_l}{gR^2}\left[1 + \frac{a}{R}P_1(\cos\phi) + \frac{a^3}{R^3}P_2(\cos\phi)\right]^{-\frac{1}{2}} \tag{2.13}$$

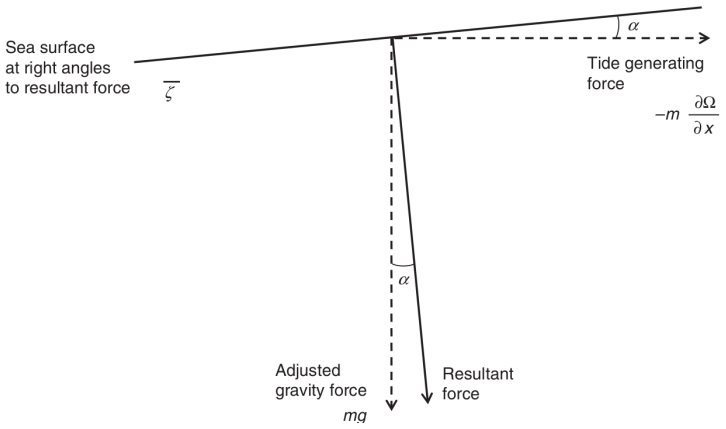

Figure 2.2: Scheme of displacement of equilibrium water surface related to tide-generating force and the normal of the Earth's gravity force. Credit: (Pugh and Woodworth, 2014a).

and replacing $G = \frac{ga^2}{m_e}$ (from the gravitational force on a particle of mass m on Earth's surface, with m_e the Earth's mass: $mg = G\frac{mm_e}{a^2}$), and $\cos\phi$ from equation 2.10, the expression of the Equilibrium Tide is:

$$\zeta = a\frac{m_l}{m_e}\left(\frac{a}{R}\right)^3\left[C_0(t)\left(\frac{3}{2}\sin^2\phi_P - \frac{1}{2}\right) + C_1(t)\sin 2\phi_P + C_2(t)\cos^2\phi_P\right] \tag{2.14}$$

with:

$$\begin{aligned} C_0(t) &= \left(\frac{a}{R}\right)^3\left(\frac{3}{2}\sin^2 D_l - \frac{1}{2}\right) \\ C_1(t) &= \left(\frac{a}{R}\right)^3\left(\frac{3}{4}\sin^2 D_l \cos C_P - \frac{1}{2}\right) \\ C_2(t) &= \left(\frac{a}{R}\right)^3\left(\frac{3}{4}\cos^2 D_l \cos 2C_P - \frac{1}{2}\right) \end{aligned} \tag{2.15}$$

the coefficients that depend on astronomical coordinates that vary with time, and define the long-period, diurnal, and semi-diurnal tidal species i.e. the occurrence of high-water (or low-water) per day due to tides. Diurnal tides have one episode per day, semi-diurnal have two, and long-period tides can occur with periods that last for days or months.

2.2 Tidal constituents as periodic signals

Tides are a periodic phenomenon that can be represented as a sum of N sinusoidal signals with amplitude H_n, phase g_n, and frequency ω_n:

$$\sum_{n=1}^{N} H_n \cos(\omega_n t - g_n) \tag{2.16}$$

Each signal is caused by a defined effect, called constituent, of the Sun, the Moon, or their combination, and their position with respect to the Earth. The frequency ω_n of the single constituent can be represented by a sum of similar frequencies, called basic astronomical

frequencies ($\omega_{1...6}$), that are the rate of change of six astronomical arguments (Tamura, 1987): the time angle in lunar days, the Moon's geocentric mean ecliptic longitude, the Sun's geocentric mean ecliptic longitude, the longitude of lunar perigee, the mean longitude of the ascending node, and the longitude of the perihelion (τ, s, h, p, N, and p' respectively):

$$\omega_n = i_1\omega_1 + i_2\omega_2 + i_3\omega_3 + i_4\omega_4 + i_5\omega_5 + i_6\omega_6 \tag{2.17}$$

Integers $i_{1...6}$ (often called Doodson numbers, e.g. Foreman and Henry, 1989) and the basic astronomical frequencies needed to describe each constituent are derived from the harmonic expansion of the Equilibrium Tide's coefficients. For instance, the semi-diurnal tidal species coefficient $C_2(t)$, can be expanded in combination with astronomical coordinates:

$$\begin{aligned} C_2(t) = \psi\,[\cos(2\omega_0 t + 2h - 2s) + \frac{7}{2}e\cos(2\omega_0 t + 2h - 3s + p) \\ + \frac{1}{2}e\cos(2\omega_0 t + 2h - s - p + 180^\circ)] \end{aligned} \tag{2.18}$$

where ψ is a coefficient dependent on D_l, a and the mean lunar distance; ω_0 is the rate of change of the mean solar day, and e is the Earth's orbit eccentricity. The cosine arguments in square brackets represent three tidal constituents, called M2, N2 and L2. The first term: $(2\omega_0 t + 2h - 2s)$, tells us that M2 changes in time according to frequencies: $2(\omega_0 + \omega_3 - \omega_2)$, that correspond to twice the rate of change of τ, $2\omega_1 = 28.9842\ ^\circ/hour$ (cfr. table 3.2 in Pugh and Woodworth, 2014a). With similar reasoning, one can derive also the frequencies of constituent N2:

$$2\omega_1 - \omega_2 + \omega_4 = 28.4397\ ^\circ/hour$$

and L2:

$$2\omega_1 + \omega_2 - \omega_4 = 29.5285\ ^\circ/hour$$

For M2 it is thus easy to see that the Doodson numbers are: [2 0 0 0 0 0 0]; for N2: [2 −1 0 1 0 0], and for L2: [2 1 0 −1 0 0]. Integer i_1 defines the tidal species, i_2 the group within the species, and i_3 the tidal constituent. In general, $i_{2...6}$ vary between -5 and 5, but sometimes they can be summed by 5 units to avoid negative numbers (Doodson, 1921). Another convention is related to the use of time in solar days, instead of lunar days, which brings to [2 −2 2 0 0 0 0] for M2 (Schureman, 1971). Another observation to be done is that the L2 cosine argument contains also the 180° term, which is called Doodson extended number, and it is used as correction, so that cosine and sine terms are all positive. The symbols used to name tidal constituents are called Darwin symbols (Darwin, 1889), and are always a combination of numbers and letters. The numbers indicate the constituent's tidal species, while the letters are used since the last decades of the XIX century, and are related to the old concept of "phantom satellites" introduced by Laplace to describe the effect of the Moon, the Sun, and their combined effect on tidal movements (Cartwright, 1999). Doodson numbers, frequencies, and Doodson extended numbers of tidal constituents

are listed in tidal catalogues, together with their tidal potential coefficients. An example is the HW95 catalogue (Hartmann and Wenzel, 1995), that contains the tidal potential of 12935 waves due to the Moon, the Sun and other planets like Venus, Jupiter, Mars, Mercury and Saturn.

2.2.1 Astronomical arguments

Tide generating potential has been computed over decades by several researchers. Among the most famous examples, it is worth to mention Doodson, 1921, Cartwright and Tayler, 1971, Wenzel, 1997, and Tamura, 1987. In their works, the six aforementioned astronomical arguments are derived according to different conventions. In this project, the formulae used are based on the MERIT standards (e.g. Teisseyre, 2013), and illustrated in Tamura, 1987:

$$\tau = GMST + \pi - s$$

$$s = 218.3166 + 4812678.8119 \cdot t_{MJD} - 0.1466 \cdot t_{MJD}^2 + 0.00185 \cdot t_{MJD}^3 - 0.000153 \cdot t_{MJD}^4$$

$$h = 280.4664 + 360007.6974 \cdot t_{MJD} + 0.0303 \cdot t_{MJD}^2 + 0.00002 \cdot t_{MJD}^3 + 0.000065 \cdot t_{MJD}^4$$

$$p = 83.3532 + 40690.1363 \cdot t_{MJD} - 1.0321 \cdot t_{MJD}^2 - 0.0124 \cdot t_{MJD}^3 + 0.00052 \cdot t_{MJD}^4$$

$$N = -(234.9554 + 19341.3626 \cdot t_{MJD} - 0.2075 \cdot t_{MJD}^2 - 0.00213 \cdot t_{MJD}^3 + 0.000165 \cdot t_{MJD}^4)$$

$$p' = 282.9373 + 17.1945 \cdot t_{MJD} + 0.04568 \cdot t_{MJD}^2 - 0.0000177 \cdot t_{MJD}^3 - 0.000033 \cdot t_{MJD}^4$$

It can be noticed that the mean longitude of the ascending node of the Moon, N, has a negative sign. This is because this formula refers to the *negative* mean longitude of the ascending node. The astronomical arguments are represented by a constant angle and other three terms that indicate the linear, and higher-order variations in time t_{MJD} of the single coordinates (here, decimals are truncated for better visualization). The variable t_{MJD} is the time expressed in millennia of Modified Julian Days (MJD). This expression differs with respect to Tamura, 1987, who used centuries of MJD. MJD is defined as $MJD = JD - 2400000.5$, where JD is the Julian Day, that starts at 12:00 on the 1st of January 4713 B.C. (Petit and Luzum, 2010). The Greenwich Mean Sidereal Time (GMST) used to compute τ is defined as the "Greenwich hour angle of the mean equinox defined by a conventional relationship to Earth Rotation Angle or equivalently to Universal Time (UT1)" (Petit and Luzum, 2010). In this work GMST is derived using the relationship with UT1, according to e.g. (Seidelmann et al., 1992). Starting from the time of interest in JD, the Greenwich Mean Sidereal

Time in seconds is calculated at first for UT1 = 0:

$$GMST0 = 24110.54841 + 8640184.812866 \cdot T + 0.093104 \cdot T^2 - 0.0000062 \cdot T^3 \quad (2.19)$$

with T the integer time in Julian centuries ($I(JD)$) starting from 12:00 on the 1st of January 2000 (i.e.: $T = \frac{I(JD)-2451545}{36525}$). In order to compute the elapsed time between UT1=0 and the event of interest, the ratio of the mean sidereal time to UT1:

$$r = 1.002737909350795 + 5.9006 \cdot 10^{-11} \cdot T - 5.9 \cdot 10^{-15} \cdot T^2 \quad (2.20)$$

should be multiplied to the fraction of the day of interest:

$$GMST_{mod} = r(MJD - I(MJD)) \quad (2.21)$$

so that the difference of few minutes between UT1 and the mean sidereal day is accounted. GMST is obtained by adding equation 2.21 to equation 2.19 in days:

$$GMST = \frac{GMST0}{84600} + GMST_{mod} \quad (2.22)$$

Finally, it is worth to mention that the coefficients used to describe the astronomical arguments change according to a defined epoch of reference, and are periodically recalculated to account for variations in Earth's rotation.

2.2.2 Nodal corrections

The Moon's declination has a modulation over a period of 18.61 years that affect all lunar tidal constituents. An example is shown in figure 2.3 for M2; the amplitude at Newlyn station is computed every year through 80 years of data, and shows clear periodic variations due to the 18.61-year nodal cycle. Such issue can be accounted for by using two corrections, namely, nodal corrections, for amplitude and phase of the tidal signal (f_n and u_n respectively). Therefore the periodic function that describes the tidal height due to one n constituent becomes: $f_n H_n \cos(V_n + \omega_n t + u_n - g_n)$, with V_n the argument or phase of the equilibrium tide, i.e. the constant term in the astronomical argument equations. In fact, according to (Le Provost, 2001), one can rewrite $V_n + \omega_n t$ as:

$$\omega_n t + V_n = i_1\tau + i_2 s + i_3 h + i_4 p + i_5 N + i_6 p' \quad (2.23)$$

The nodal corrections can be derived from the orbital elements N and p, and can be easily found in literature for the main constituents (see examples in table 2.2). However, in case of overtides or compound tides, these corrections must be calculated following rules, illustrated in e.g. the International Hydrographic Organization (IHO, 2006). Overtides are constituents that occur at multiples times with respect to their base frequency, like M4 or M6, that have double and triple the frequency of M2; compound tides are constituents with

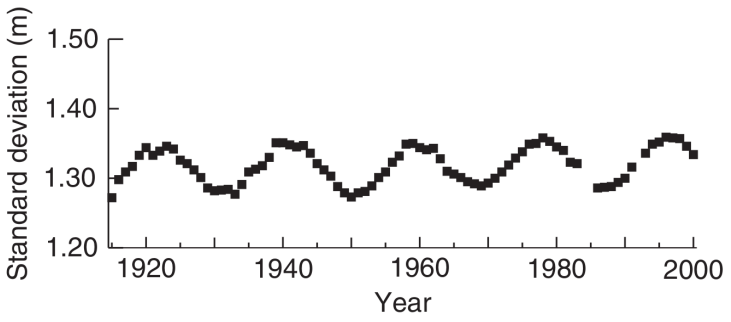

Figure 2.3: M2 18.61-year amplitude modulation at Newlyn station. Credit: (Pugh and Woodworth, 2014a)

frequencies that are a linear combination of interacting tides - for example, MS4 is given by the interaction between M2 and S2 (Andersen et al., 2006). For these constituents, u_n is the result of a sum of all tidal contributors, while f_n comes from their multiplication. For example, let's consider the compound tide 3MS2, that is generated by interaction between M2 and S2 constituents, and has frequency 26.952313 $^\circ/hour$, that is the difference between tidal frequencies of 3 times M2 and twice S2: $3 \cdot 28.984104 - 2 \cdot 30$. The value of nodal corrections is then:

$$f_{3MS2} = f_{M2}^3 \cdot f_{S2}^2 = f_{M2}^3$$

$$u_{3MS2} = 3 \cdot u_{M2} - 2 \cdot u_{S2} = 3 \cdot u_{M2}$$

because $f_{S2} = 1$ and $u_{S2} = 0$. The same principle applies for overtides.

Constituents	f_n	u_n
M2, N2, $\mu 2$	$1.000 - 0.037 \cos N$	$-2.1^\circ \sin N$
K1	$1.006 - 0.115 \cos N$	$-8.9^\circ \sin N$
S2	1.000	0.0°
Q1, O1	$1.009 - 0.187 \cos N$	$10.8^\circ \sin N$
K2	$1.024 - 0.286 \cos N$	$-17.7^\circ \sin N$
Mm	$1.000 - 0.130 \cos N$	0.0°
Mf	$1.043 - 0.414 \cos N$	$-23.7^\circ \sin N$

Table 2.2: Examples of nodal corrections for main constituents. Credit: (IHO, 2006).

2.3 Methods of tidal estimation

Tides can be derived by solving inverse and direct problems. With empirical models, the inverse problem is solved when tidal harmonic constants are found, starting from a set of observations (usually sea level measurements). This is the case of harmonic and responsive

methods. Hydrodynamic models instead, find tidal constants by solving the direct problem of Laplace Tidal Equations (LTE). In this section a summary of the aforementioned methods is summarized.

2.3.1 Harmonic method

The harmonic method is based on the principle that sea level timeseries contain information on tides, that can be described as a sum of sines and cosines. In section 2.2 it has been shown that the tidal height $\zeta(t)$ can be expressed as a sum of N tidal constituent signals:

$$\zeta(t) = \sum_{n=1}^{N} f_n H_n \cos(\omega_n t + V_n + u_n - g_n) \tag{2.24}$$

This equation can be rewritten, according to the sum of trigonomeric functions, as:

$$\zeta(t) = \sum_{n=1}^{N} [A_n \cdot f_n \cos(\omega_n t + V_n + u_n) + B_n \cdot f_n \sin(\omega_n t + V_n + u_n)] \tag{2.25}$$

where:

$$A_n = H_n \cos(g_n) \tag{2.26}$$

$$B_n = H_n \sin(g_n) \tag{2.27}$$

are the unknown in-phase and quadrature coefficients that can be derived using the least-squares. H_n and g_n can be then obtained from:

$$H_n = \sqrt{A_n^2 + B_n^2} \tag{2.28}$$

$$g_n = tan^{-1}\left(\frac{B_n}{A_n}\right) \tag{2.29}$$

This method is used in this project, and it is illustrated in more detail in chapter 4.

2.3.2 Response method

The response method is based on the principle that tides are the part of sea level that respond to a gravitational unit impulse $V(t - s\Delta t)$ at time t (Munk and Cartwright, 1966):

$$\zeta(t) = \sum_{s=-S}^{S} w(s) V(t - s\Delta t) \tag{2.30}$$

where Δt is a certain time lag increment and s is the number of lags; $w(s)$ are weights that represent the remaining effect at time t of the ocean's response to a unit impulse at time $(t - s\Delta t)$ (Smith, 1999). The Fourier transform of $w(s)$ is called admittance, and it is defined as the ratio between impulse and response in the frequency domain f, which is the frequency expressed in cycles per day, (Munk and Cartwright, 1966):

$$Z(f) = \int_0^{\infty} w(\Delta t) e^{-2\pi i f \Delta t} d\Delta t = \frac{H(f)}{G(f)}$$

Where H and G in this case are respectively the sea level response and the gravitational impulse in the frequency domain:

$$H(f) = \int_{-\infty}^{\infty} \zeta(t) e^{-2\pi i f t} dt$$

$$G(f) = \int_{-\infty}^{\infty} c(t) e^{-2\pi i f t} dt$$

and the complex function $c(t) = a(t) + ib(t)$ represents the coefficients of the spherical harmonic expansion of gravitational potential $V(t)/g$. $Z(f)$ is a complex function ad it is also defined by coefficients $Z(f) = X(f) + iY(f)$:

$$X(f) = \sum_{s=-S}^{S} u(s)\cos(2\pi f s\Delta t) + v(s)\sin(2\pi f s\Delta t)$$

$$Y(f) = \sum_{s=-S}^{S} u(s)\cos(2\pi f s\Delta t) - v(s)\sin(2\pi f s\Delta t)$$

where $u(s)$ and $v(s)$ are the complex coefficients of weights: $w(s) = u(s) + iv(s)$, and are relative to a certain tidal band tb and not for e.g. single constituents. In fact, the fundamental assumption of the response method is the so-called *credo of smoothness*, that states that the oceanic response to tidal forcing at adjacent frequencies within a certain tidal band are nearly the same. This is especially true in deep oceans where tides within diurnal and semi-diurnal bands have 30% of correlation on a 10-degree resolution (Smith, 1999). So, for each tidal band, it is found only one complex admittance defined by $w(s)$. $w(s)$ can be derived through least squares from equation 2.30, that can be rewritten in terms of complex coefficients (Munk and Cartwright, 1966):

$$\zeta(t) = \sum_{tb} \sum_{s=-S}^{S} u_{tb}(s)a(t - s\Delta t) + v_{tb}(s)b(t - s\Delta t)$$

Finally, the amplitude and phase can be derived from: ((Cartwright and Ray, 1991)):

$$H(f) = \tilde{H}(f)\sqrt{X_{tb}^2(f) + Y_{tb}^2(f)}$$

$$g(f) = |\pi \cdot tb| - \tan^{-1}\left(\frac{Y_{tb}(f)}{X_{tb}(f)}\right)$$

where $\tilde{H}(f)$ are the known amplitudes associated to the tide potential illustrated in (Cartwright and Tayler, 1971) and (Cartwright and Edden, 1973). With this approach, amplitude and phase of the major tidal constituents of each tidal band – usually M2, S2, N2, K2, 2N2 for the semi-diurnal, and K1, O1, Q1 for the diurnal bands – are derived (Le Provost, 2001). Minor tidal constituents can be inferred through admittance interpolation (usually linear, or quadratic) of major constituents:

$$Z_n = \sum_{k=1}^{p} \alpha_k^n Z_k$$

where Z_n is the complex admittance of a minor constituent n, Z_k the complex admittances of major constituents and p the interpolation order; α_k^n is the interpolation coefficient that varies according to p. For instance, constituent J1 can be inferred through linear admittance estimates based on O1 and K1; α_k^{J1} are :

$$\alpha_1^{J1} = \frac{f_{J1} - f_{O1}}{f_{K1} - f_{O1}} \qquad \alpha_2^{J1} = \frac{f_{K1} - f_{J1}}{f_{K1} - f_{O1}}$$

Z_n can be decomposed in real and imaginary parts, and expressed in terms of tide potential and tidal height coefficients. Following (Petit and Luzum, 2010) (equation 6.16), one can derive the in-phase and quadrature coefficients of minor tides. And for J1 the formulae become:

$$A_{J1} = \frac{f_{J1} - f_{O1}}{f_{K1} - f_{O1}} \frac{\tilde{H}_{J1}}{\tilde{H}_{O1}} A_{O1} + \frac{f_{K1} - f_{J1}}{f_{K1} - f_{O1}} \frac{\tilde{H}_{J1}}{\tilde{H}_{K1}} A_{K1}$$

$$B_{J1} = \frac{f_{J1} - f_{O1}}{f_{K1} - f_{O1}} \frac{\tilde{H}_{J1}}{\tilde{H}_{K1}} B_{O1} + \frac{f_{K1} - f_{J1}}{f_{K1} - f_{O1}} \frac{\tilde{H}_{J1}}{\tilde{H}_{K1}} B_{K1}$$

In this work, the admittance method has been applied to derive the height of minor constituents, which was added to major constituent heights according to equation 2.25, in order to predict the total tidal height. The total tidal height is the quantity used as tidal correction for altimetry data. More details about ocean tide correction for altimetry can be found in section 3.2.6.

2.3.3 Laplace tidal equations

The Laplace method is based on Laplace equations on the motion of a fluid subject to gravity. In 1779, Laplace calculated also the tide-producing force, that is intended as a gravitational force whose effect on the Earth is symmetrical about the line of attraction between the Earth and the attracting body (Moon or Sun), and pulls the ocean into an ellipsoidal shape with major axis along this line (Gill, 2016). LTE are solved numerically to derive ocean tides, and are the basis for hydrodynamic tide models. Usually, LTE are solved on a mesh, and are coupled with other drivers that describe the ocean environment, such as friction or wind forcing. LTE standard mathematical expressions are displayed here for completeness, however no further details are given, as the author's work was focused on harmonic method (and admittance, for what concerns tidal prediction). LTE are derived from the continuum equations of mass and momentum conservation, under the following assumptions (Hendershott, 1981): a perfect fluid, uniform rotation that causes small disturbances, a spherical Earth, geocentric gravitational field and uniform horizontally and in time, rigid ocean bottom, and shallow ocean in which both the Coriolis acceleration the vertical component of the particle acceleration are neglected. LTE expressions according to (Hendershott, 1981) are:

$$\frac{\partial u}{\partial t} - 2\Omega \sin\theta v = -\frac{\partial}{\partial \phi}\left(\frac{\zeta - \frac{\Gamma}{g}}{a\cos\theta}\right)$$

$$\frac{\partial v}{\partial t} - 2\Omega \sin\theta u = -\frac{\partial}{\partial \theta}\left(\frac{\zeta - \frac{\Gamma}{g}}{a}\right)$$

$$\frac{\partial \zeta}{\partial t} + \frac{1}{a\cos\theta}\left[\frac{\partial uD}{\partial \phi} + \frac{\partial vD\cos\theta}{\partial \theta}\right] = 0$$

where ϕ ad θ are longitude and latitude with corresponding velocity components (u, v), ζ the ocean surface elevation, Γ the tide-generating potential, D the ocean depth, a the Earth's spherical radius, g the gravitational attraction, and Ω the Earth's angular rate of rotation. The first two equations represent the horizontal acceleration of the water mass on a rotating Earth as a consequence of the tidal disturbance Γ, while the third equation is the mass continuity equation, which shows that a net flux of water for a certain area of height D must be in balance with the variation of water level (Smith, 1999). LTE are extended to shallow water, using the assumption that motions have large horizontal scales compared to water depth and therefore lie in hydrostatic balance (Arbic et al., 2012).

2.4 State of the art of ocean tide models

The last, and most comprehensive, assessment on global ocean tide models was made by Stammer et al., 2014 (henceforth St14), and contains a review of global ocean tide models available at that time, with assessment exercises on global and regional scales. St14 takes in consideration 15 tide models, divided according to their common features: 7 data-constrained models, 2 historical models, and 6 purely hydrodynamic models. Data-constrained models involve data exploitation, and are divided into semi-empirical models, i.e. based on prior models and adjusted with data (usually altimetry), and barotropic hydrodynamic models, that are based on hydrodynamic expressions (like purely hydrodynamic models) constrained by assimilated data from e.g. altimetry or tide gauges. The global differences between models for M2 constituent showed that data-constrained models have similar behaviour in open ocean (below 3 mm), but high disagreement at coastal, shelf, and Polar regions, with values larger than 1 cm. Differences are mainly due to interpolation techniques, missing data in critical regions (the Arctic Sea, because covered by ice, and the coast), and eddy energy aliasing. Comparisons with tide gauge data showed root sum squares (RSS) errors around 1 cm in deep ocean, 5 cm in shelf waters, and 6 cm at the coast. These results have dramatically improved since the assessment of Shum et al., 1997 (henceforth Sh97), in which the disagreement between models for M2 was 2-3 cm in deep ocean, and their best RSS was of 2.5 cm in the same area. Large improvements were observed for shallow water results, going from 23 cm in Sh97 to 3.5 cm for M2 constituent. Part of these improvements are coming from the more and more frequent use of altimetry as tide model constraint. A clear evidence are the purely hydrodynamic models, that, despite advances in understanding the ocean physics and in numerical strategies, still remain much less accurate

than data-constrained models (for M2 constituent, the best purely hydrodynamic model gives 4.27 cm error, against 0.5 cm of data-constrained models). As St14 authors argue, it must be specified that these improvements in models are also given by more accurate in situ data and databases. Ray, 2013 shows that data selection criteria and processing choices, can reduce the difference between in situ data and tide models. He compares a newly compiled bottom pressure gauge dataset (later used in St14), with the ST102 dataset used in in Sh97, obtaining a difference of 0.51 cm with GOT4.8 tide model M2 constituent, against 1.45 cm obtained with ST102. Another consideration must be done for coastal results in St14. RSS are obtained using 56 tide gauges distributed on global scale. Certainly, the number of in situ data was the best possible at that time, but unfortunately not enough, as large areas like South America, South East Asia, and India are left out. Also, as a consequence of data scarcity in critical regions, it can happen that few locations with large errors may affect the final assessment through RSS errors. In September 2018, during the "25 Years of progress in radar altimetry" Symposium, F. Lyard, in his review about tide models, pointed out that model improvements have a different pace according to the constituent. For example, it is expected that improvements of constituents with long aliasing period (e.g. K1 with 6 or 12 months aliasing, see section 3.5) may be smaller than constituents whose aliasing period lasts for few days. By studying the sea level anomaly variance reduction, he showed that large errors are still found in front of Bangladesh coast, in Indonesia, around Antarctica for M2 and K1, and in the Gulf of Mexico for K1. Apart from the Polar regions, where altimetry data are scarce or poor, Lyard found out that tide models in the Western Pacific remain still noisier than the Atlantic, probably because signals coming from internal tide are not separated from the barotropic tidal signal [1]. Current studies on tide models are mainly focused on two aspects: the improvement of coastal and polar tidal estimation, and a better description of internal tide signals. For the first issue, modelists work on the enhancement of bathymetry and coastline resolution, as well as assimilation techniques (e.g. Cancet et al., 2016). On the other side, the current studies in internal tides have shown that baroclinic tide models can be used as altimetry corrections, in order to remove short-scale tidal variability (this concept has been illustrated by R. Ray, during the "25 Years of progress in radar altimetry" Symposium 2018). However, improvements in tide models are still affected by intrinsic limitations due to altimetry data, whose instrumental noise, orbit determination and repetition, are problematic for tide determination.

[1] Strictly, "barotropic" means that the pressure is constant on surfaces of constant density (Gill, 2016). When we speak about barotropic (or surface) tides, it is intended tides associated with the sea surface. Internal, or baroclinic tides are forced by barotropic tidal currents that move water layers of different density, according to the topography of the ocean (Pugh and Woodworth, 2014a).

Existing models

Since St14, new versions of ocean tide models were released. In this section a short description on current models available (and eventually mentioned in this thesis) is given. Tide models are usually released as a set of regular grids, with different resolutions that can go from 1/2 to 1/30 degree in both longitude and latitude directions. Pairs of grids give information on harmonic constants (amplitude and phase, or in-phase and quadrature coefficients) of single constituents - generally grids for the main 8 constituents (M2, S2, N2, K2, K1, O1, Q1, P1) are available. At each grid point (or node) one finds information on longitude, latitude, and e.g. amplitude. It is possible that hydrodynamic models (e.g. FES2014) are computed on a mesh, characterized by an irregular distribution of grid points, that guarantees a finer resolution at coastlines or in critical areas. However, because the exploitation of such grids is computationally demanding, these models are often released on a regular grid. Figures 2.4 and 2.5 show an example of tidal grids of model FES2014, for M2 tidal constituent.

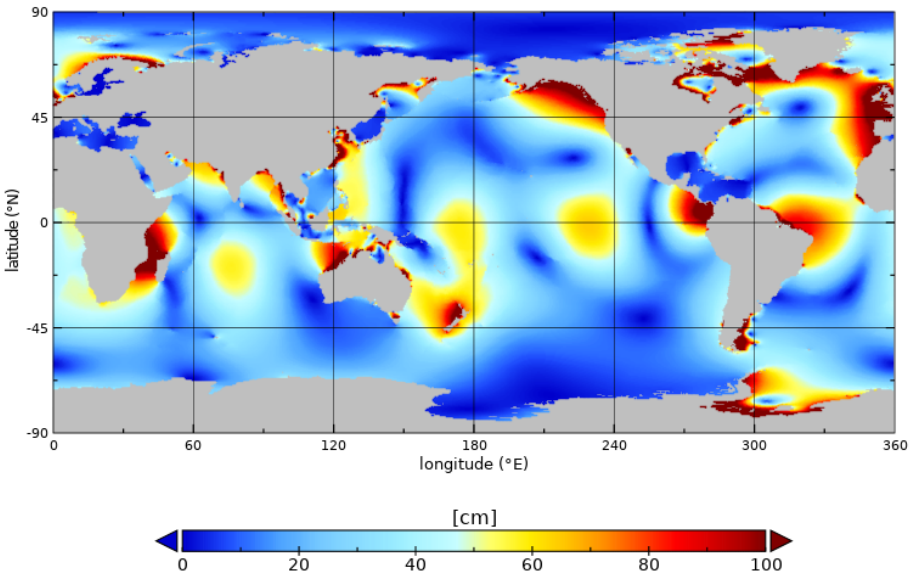

Figure 2.4: Amplitude of M2 tidal constituent, from FES2014 model.

The currently existing models, that will be mentioned throughout this thesis are:

- DTU16: it is the latest version of the Danish Technical University (DTU) tide model series. It is a semi-empirical model based on altimerer data provided by the Radar Altimeter Database System (RADS) for missions TOPEX/Poseidon (T/P), Jason-1, Jason-2, SARAL/AltiKa in the Arctic, and ERS-1 to improve the model at high latitudes. FES2012 ocean tide model is used as background model (Cheng and Andersen, 2017). The residual tidal signal is estimated along track through the responsive method, and then interpolated onto FES2012 grid using the dynamic interpolation

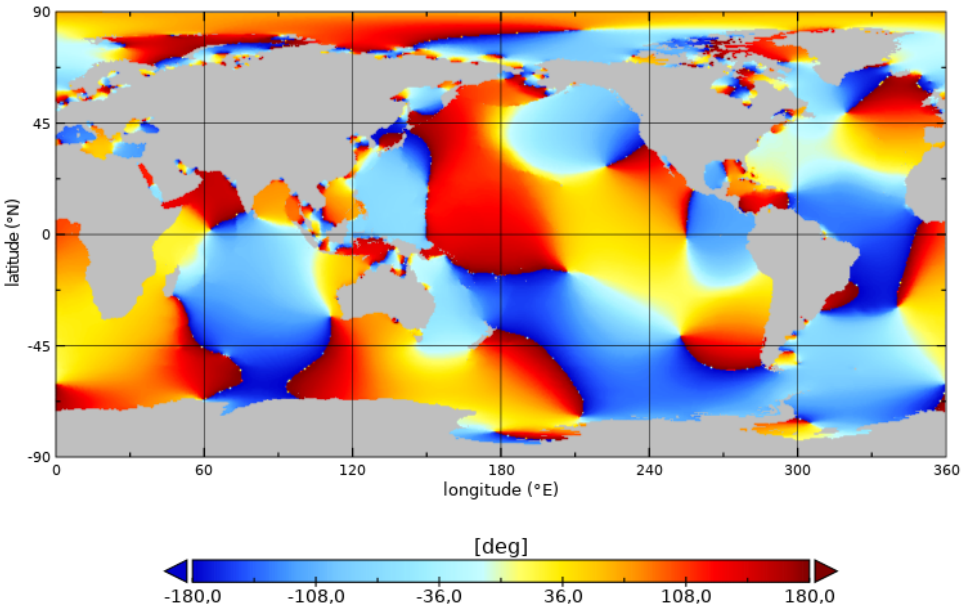

Figure 2.5: Phase of M2 tidal constituent, from FES2014 model.

method (Andersen, 1999), that takes into account the water depth. The latter, is defined according to DTU10 bathymetry model. DTU16 provides grids for 8 major tidal constituents: M2, S2, N2, K2, K1, O1, Q1, and P1.

- EOT11a: the Empirical Ocean Tide model has been released in 2012 by (Savcenko and Bosch, 2012) and it is the latest global version of DGFI-TUM EOT series. The model has a resolution of 1/8 degree, and harmonic constants for constituents: M2, S2, N2, K2, 2N2, K1, O1, Q1, P1, S1, Mf, Mm and M4. Tides are estimated through least-squares harmonic analysis performed on altimetric residuals of FES2004 tide model. Multi-mission altimetry data are interpolated on FES2004 grid, and the least-squares is combined with a Variance Component Estimate (VCE) so that missions are weighted according to their performance (more details about EOT technique can be found in chapter 4).

- GOT4.10: in the Goddard Ocean Tide (GOT) series tidal constituents are estimated with standard harmonic analysis for constituents Q1, O1, S1, K1,N2, M2, S2, K2, and M4. Smaller constituents are inferred from admittances. The tidal analysis is computed on altimetry residuals relative to a combined background model, that includes several global, regional, and local tide models (Ray et al., 2011). The latest version is GOT4.10, in which only data from Jason-1 and Jason-2 were used, with no T/P data. In shallow areas, it is recommended to use version 4.8 (R. Ray, personal communication). However, because of their coarse spatial resolution of 1/2 degree, GOT models are not considered to be the best option to investigate tides in shallow seas or coastal

areas.

- HAMTIDE11a: the Hamburg direct data Assimilation Methods for TIDEs (HAMTIDE) model has spatial resolution 1/8 degree and it is a global model based on the generalized inverse methods for tides developed at the University of Hamburg (Zahel, 1995). Solutions are constrained by 15 years of satellite altimeter data (missions: T/P and Jason-1) compiled by DGFI-TUM (Bosch et al., 2009). The constituents provided are: M2, S2, N2, K2, K1, O1, Q1, P1, and 2N2.

- OSU12v1.1: OSU12 ocean tide model is an empirical barotropic model, with spatial resolution of 1/16 degree. The model computes response tidal analyses on multi-missions radar altimeter data, including T/P, Jason-1, Geosat Follow On (GFO) and Envisat, with time coverage between October 1992 and January 2009. Version 1.0 of this model has no empirical solutions beyond ±66 degree latitude bounds, therefore GOT4.7 is patched at higher latitudes (Fok, 2012). Version 1.1 was kindly provided by H. Fok, with the help of C. K. Shum, and they explained that this new version still needs to be updated with new data, and corrected for errors found in the prior model.

- FES2014: it is the last version of the FES (Finite Element Solution) tide developed by LEGOS, NOVELTIS and CLS, within a CNES funded project. FES2014 is based on the T-UGO model, which solves tidal barotropic equations through spectral configuration. In addition, the model assimilates altimeter observations and in situ data. Altimetry data are assimilated as along-track and crossover timeseries, from missions: T/P, Jason-1, Jason-2, ERS-1, ERS-2, and Envisat. The in situ dataset used in the model comprises 600 stations, among which: the WOCE coastal database, open ocean bottom-pressure recorders (BPR) used in St14, open ocean BPR in Antarctica from LEGOS, Arctic database by Kowalik and Proshutinsky, 1993, BHI and LEGOS, 4 tide gauge stations of R. Ray's shelf dataset located in Florida (Mathilde Cancet, personal communication). FES2014 is characterized by an accurate bathymetry and a refined mesh (a total of ~ 2.9 million nodes) useful to describe coastlines and shallow-water regions. FES2014 is released as global regular grids with 1/16 degree resolution of 34 tidal constituents: 2N2, EPS2, J1, K1, K2, L2, La2, M2, M3, M4, M6, M8, Mf, MKS2, Mm, MN4, MS4, MSf, MSqm, Mtm, μ2, N2, N4, ν2, O1, P1, Q1, R2, S1, S2, S4, Sa, Ssa, T2.

- TPXO8: TPXO is a series of ocean tide fully-global models derived using the representer-based variational scheme (Egbert and Erofeeva, 2002) to assimilate altimetry and in situ data into a global shallow-water model. Harmonic constants are computed from along-track observations from 685 T/P and Jason cycles (up to 2011), and 114 cycles of T/P on its interleaved orbit; at high latitudes ERS/Envisat data were also used to

improve lunar tides (St14). In the same area, tide gauge data were also assimilated, including 83 around Antarctica by King and Padman, 2005 and 289 in the Arctic by Kowalik and Proshutinsky, 1993. TPXO8 tidal grids are the result of a combination of a basic global solution, with resolution of 1/6 degree, and local solutions, with 1/30 degree resolution. The global grids are provided with a final resolution of 1/30 degree, for tidal constituents: M2 S2 N2 K2 K1 O1 P1 Q1 M4. Grids of minor constituents (MF, MM, MN4, and MS4) are also provided, with a resolution of 1/6 degree.

- STORMTIDE: this purely hydrodynamic model has been developed within the framework of the German consortium project STORM, whose aim is to develop a high-resolution ocean circulation and tide model (Müller et al., 2014). STORMTIDE has a horizontal resolution of 5-10 km (it is released as tripolar grid with 0.1 degree resolution) and it provides grids for 8 tidal constituents: M2, N2, S2, K2, K1, Q1, P1, O1, and P1. Tides are derived by lunisolar tidal potential of second degree, described by analytical ephemerides. The global model is forced by climatological wind stress and heat fluxes. Tides are forced by an ephemeral forcing, where the positions of the sun and moon are computed at each time step of model simulation.

- HYCOM: tidal estimates obtained from the HYbrid Coordinate Ocean Model simulations have a nominal horizontal resolution of 1/12.5 degree, distributed on a tripolar grid (St14). HYCOM simulation was done simultaneously to resolve barotropic tides, baroclinic tides, and an eddying general circulation on a horizontally uniform two-layer stratification with only tidal and surface seawater (buoyancy) forcing (Arbic et al., 2010).

- HIM: the Hallberg Isopycnal Model is a isopycnal coordinate, primitive equation ocean model whose simulations employ a parameterized topographic wave drag that represent tidal energy loss in regions of rough topography (St14). Tidal estimates are released with resolution of 1/8 degree and latitude coverage between 86 degrees South and 82 degrees North.

In chapter 6 the aforementioned models are compared.

Chapter 3

Sea level from satellite altimetry

3.1 The basic principle of radar altimetry

With the radar altimeter it is possible to measure the distance between its position and an intercepted target. The physical principle behind this instrument is based on the simple relationship between speed, time and space: the altimeter emits an electromagnetic signal that interacts with the target - in this case, the surface of the Earth - and it is reflected back to the instrument. The distance (or range) R between the altimeter and the target is computed with the following equation:

$$R = \frac{cT}{2} \tag{3.1}$$

T is the time that the signal needs to travel from the altimeter to the target and its way back to the altimeter. The signal has a speed c which is equal to the speed of light in vacuum ($\sim 3 \cdot 10^8$ m/s). Altimeters illuminate the target producing a footprint that varies in shape and extent according to both instrument and ground features. Most of the altimeters have a pulse-limited footprint, with exception of laser altimeters, that are beam-limited, and the latest Delay-Doppler altimeters (Raney, 1998 and Cipollini and Snaith, 2015). In figure 3.1 the three types of footprints used in altimetry are shown. A beam-limited footprint is defined by the choice of the beamwidth, which is inversely related to the antenna diameter (cfr. equation 22 in Fu and Cazenave, 2001). In order to resolve smaller ground features, a narrow beamwidth is needed, and consequently a larger antenna diameter of few meters, which is unfeasible for practical reasons. That's why microwave altimeters operate with a pulse-limited design, that require a smaller antenna (e.g. 1.5 m for T/P, Fu and Cazenave, 2001), and the size of the footprint is defined by the pulse length of the emitted signal. A short pulse of duration τ (a few nanoseconds), illuminates the ground according to figure 3.2. At time t_1 the signal is emitted, and it reaches the ground at time t_2, forming a small circle that expands at t_3. At time t_4 the last part of the signal is reflected back. The

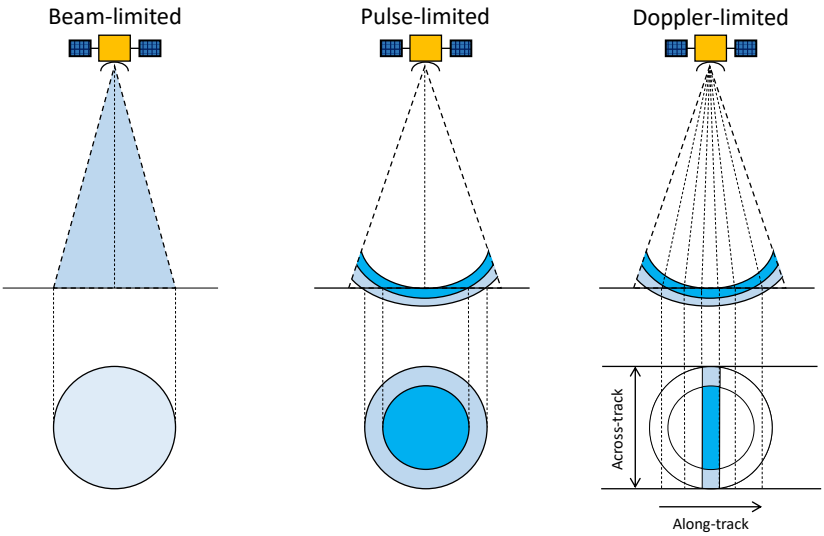

Figure 3.1: Design of radar footprints.

total footprint can be reconstructed by sampling individual echoes at the different time steps. In reality, the extent of pulse-limited footprints is of 3-5 km diameter, but at high sea states, it can reach values above 10 km (Chelton et al., 1989). The latest missions such

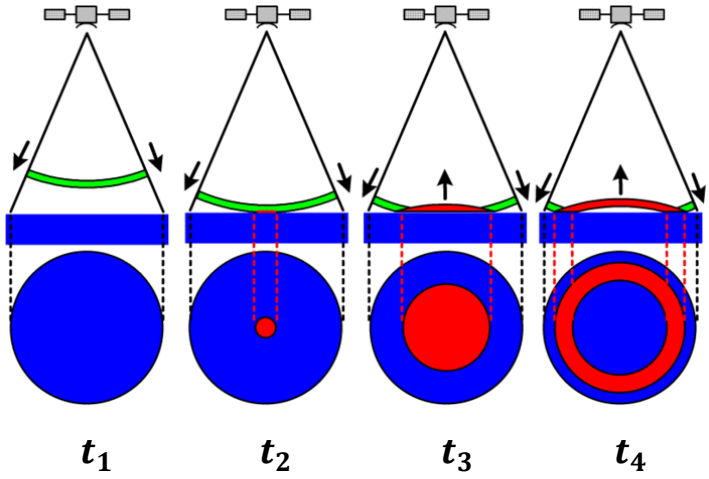

Figure 3.2: Pulse-limited footprint at different times t_1, t_2, t_3, t_4. The red area is the illuminated area on the ground at a certain time step. Modified from: `https://www.aviso.altimetry.fr/en/techniques/altimetry/principle/pulses-and-waveforms.html`.

as CryoSat-2 and Sentinel-3, can operate with a Doppler-limited design, which is effectively beam-limited along-track, with footprint dimension determined by signal processing (Raney and Phalippou, 2011), and pulse-limited across-track. Along-track, there is an independence on sea state, because the footprint size is narrowed down to circa 300 m, while across-track

the size is of around 5 km. The author wants to specify that for experiments discussed in this thesis, only data from missions with conventional (pulse-limited) altimeters were exploited; details about the missions used can be found in paragraph 3.4.

Altimeters usually work at microwave frequencies, that allow signal transmission through atmosphere, with penetration of clouds and haze. The microwave spectrum goes from 300 GHz to 300 MHz (or from 1 mm to 1 m wavelength, e.g. Hitchcock, 2004); in particular, altimeters operate between 2 and 18 GHz, encompassing S, K, X, and K bands (Fu and Cazenave, 2001). Despite atmosphere's lower opacity for microwaves, the signal is still attenuated by different factors that affect the final range value. These propagation effects are due to the presence of dry gases, water vapour, and ionospheric electrons. R depends also on other drivers, such as ocean and Earth tides, and atmosphere loading on water targets. In paragraph 3.2 the range computation and all the aforementioned geophysical effects are discussed in more detail. Usually altimetry data are transmitted to the ground at 20 Hz (e.g. Cipollini et al., 2017), with exceptions for few missions like Envisat and SARAL/AltiKa, that work at 18 Hz rate. This means that, given the satellite speed of ~7 km/s, observations occur every ~350 m. Data are then released with a 20 Hz rate, or averaged every 20 measurements and made available at 1 Hz. The latter solution requires less memory storage and it is more convenient to handle; however, for coastal or inland water applications, high-rate solutions are preferred even if they provide noisier measurements than 1-Hz data, as they provide denser spatial coverage and allow to get closer to the shore.

3.2 From range to sea level

Satellite altimeters fly over the Earth with an orbital height h_{sat}, referenced to an ellipsoid whose characteristics may slightly change according to the mission. For example, ERS missions are referenced to WGS84 ellipsoid, while Jason missions are based on T/P ellipsoid, and their radii differ of 0.7 m (Rosmorduc et al., 2016). The difference between h_{sat} and R (corrected for all the geophysical effects previously mentioned before), gives the sea surface height (SSH). The sea level, as intended in climatic analyses such as Stocker et al., 2013, is the SSH referenced to the Mean Sea Surface (MSS) and it is called Sea Level Anomaly (SLA) or sea level height anomaly, see figure 3.3. SLA is represented according to Andersen and Scharroo, 2011:

$$SLA = h_{sat} - R - \sum h_{geo} - h_{MSS} \tag{3.2}$$

where h_{geo} is the sum of the heights of all geophysical corrections and h_{MSS} is the MSS height. In the following sections the single terms used to derive SLA values are described.

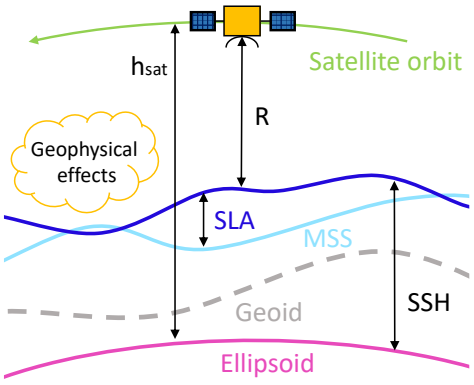

Figure 3.3: Sketch of fundamental geophysical heights in altmetry.

3.2.1 Range

The radar antenna collects the returning echoes from the ground as a timeseries of signal power, which is called waveform (see figure 3.4). For most of the missions, the timeseries is divided in discrete samples of 3.125 ns called gates (Passaro et al., 2014). The waveform contains geophysical information of the target that can be retrieved using retracking algorithms (Passaro, 2015). Retracking is a process that fits the waveform using algorithms that can be empirical (e.g. based on statistical properties of the waveform), or derived from the physical knowledge of the signal. The type of signal received by the satellite changes accord-

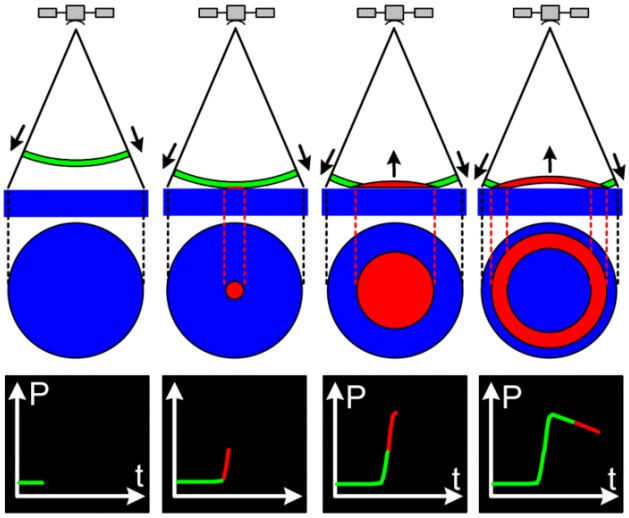

Figure 3.4: Altimeter measurement principle. Credit: `https://www.aviso.altimetry.fr/en/techniques/altimetry/principle/pulses-and-waveforms.html`.

ing to the target observed, and therefore retracking algorithms (or retrackers) must adapt according to the type of waveform to be analyzed. For example, over the open ocean, most waveforms are fitted using the Brown-Hayne model (Brown, 1977). In figure 3.5 an ideal

Brown waveform is shown; waveforms are characterized by a first rising part (leading edge), and a descending part, the trailing edge. Both provide information about the external environment - for instance, the slope of the leading edge is related to the significant wave height (SWH) - or other instrumental parameters, e.g. the altimeter mispointing (Gommenginger et al., 2011). The leading edge is important to derive the range. It must be clarified that a first estimate of the range is already given by the onboard tracker (whose purpose is to keep the reflected signal within the altimeter analysis window (Gommenginger et al., 2011)), but for higher accuracy, the waveform is analyzed on the ground and retracked. With the retracker, the mid-point of the leading edge, that represents the sea surface mean position at nadir (Passaro, 2015), is retrieved. The position of the mid-point of the leading edge with respect to the tracking reference point is called epoch. Finally, the retracked range R is found by adding the epoch to the tracking reference point.

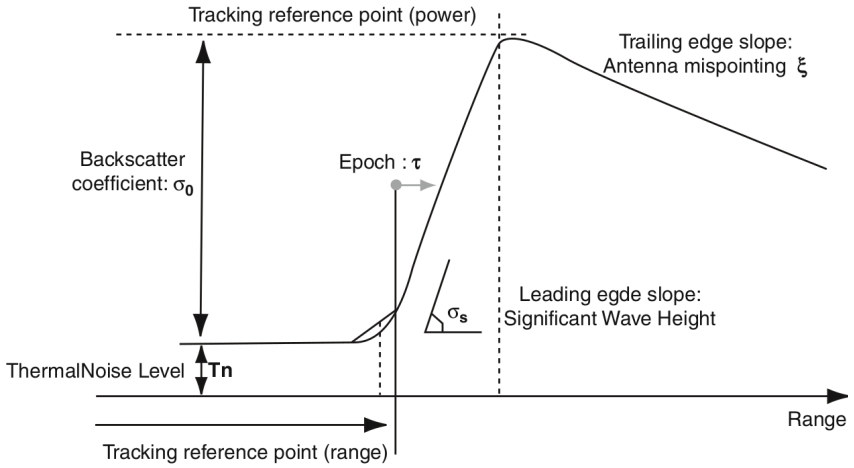

Figure 3.5: Ideal Brown ocean waveform. Credit: Gommenginger et al., 2011.

3.2.2 Dry troposperic correction

This correction is used to compensate the signal refraction due to dry gases in the atmosphere, and it can be derived by relating the air density to pressure at sea level P_0 (Andersen and Scharroo, 2011):

$$h_{dry} \approx -0.2277 P_0 (1 + 0.0026\ cos2\varphi) \tag{3.3}$$

there is also dependence on latitude φ, due to gravity. The mean magnitude of h_{dry} is circa 2 metres, with small variations (few cm) in time and space (Scharroo, 2018), and negligible changes in proximity of land. The values of this correction are determined by meteorological (operational) models, such as ECMWF and NOAA/NCEP, or reanalysis models, such as the ERA-Interim, all characterized by a temporal resolution of 6 hours. Despite different spatial resolution (16 km, 2.5-by-1.25 degrees) operational models show same accuracy, confirming

a low variability of the dry troposphere (Andersen and Scharroo, 2011). However, reanalysis models are often preferred over operational models because of their long-term stability, with neither parametrisation nor variation in algorithms.

3.2.3 Wet troposperic correction

The wet tropospheric correction h_{wet} is applied to account for the atmospheric refraction due to water vapour. h_{wet} is described as Scharroo, 2018:

$$h_{wet} \approx -6.36 IWV \tag{3.4}$$

with IWV the vertically Integrated Water Vapour density, dependent on the atmospheric temperature (for more details, please see Obligis et al., 2011). The wet tropospheric correction is highly variable in space and time: it goes from few mm in cold, dry air, to 50 cm in hot, wet air. The correction can be derived using operational and reanalysis models (the same as for the dry tropospheric correction), but also exploiting observations from microwave radiometers mounted aboard satellite payloads. Onboard radiometers allow to instantaneously monitor rapid changes in the wet troposphere; however, this correction is affected by radiometer's drift and calibration errors (Scharroo et al., 2004), and because of their large footprint (10-40 km, Scharroo, 2018) observations are contaminated by the presence of the coast, already within a distance of 30 km (Cheng et al., 2015).

3.2.4 Ionospheric correction

The presence of free electrons and ions in the ionosphere delays the altimeter radar pulse through the whole atmosphere column between the satellite and the Earth's surface (Andersen and Scharroo, 2011). The magnitude of the correction is proportional to the vertical Total Electron Content (TEC), and inversely proportional to the altimeter frequency f (Scharroo, 2018):

$$h_{ion} \approx -0.4025 \frac{TEC}{f^2} \tag{3.5}$$

The ionospheric correction can be derived from altimeter data: since T/P mission, most of altimeters operate dual-frequency, so that with the second frequency band (generally a C-band), one can measure the ionospheric path delay. Alternatively, models based on other observations like GPS or DORIS are used, such as NIC09 (Scharroo and Smith, 2010) or GIM (Jee et al., 2010). The ionosphere correction has an average magnitude of 8 cm, with variations that depend on the position of the Earth with respect to the Sun - in fact, the largest values are encountered around the geomagnetic equator - and the Solar activity itself, with highest variations occurring during the day.

3.2.5 Dynamic Atmospheric correction

The atmospheric pressure causes the movement of the sea surface, that reacts as an "inverse barometer". The wind and other dynamic atmospheric changes - including the loading due to solar atmospheric tides S1 and S2 (Ray and Ponte, 2003, Ray and Egbert, 2004) - generate additional effects that are all included in the Dynamic Atmospheric Correction (DAC). The current AVISO DAC series are models based on the combination of an inverse barometer model at low resolution with a barotropic model (the 2 Dimensions Gravity Waves model, MOG-2D) forced by pressure and wind at high spatial and temporal resolution (0.25 by 0.25 degrees per 6-hour resolution).

3.2.6 Ocean tide correction

Altimetric tide corrections are expressed as heights, that are the sum of effects of single tide constituents at a certain location and time (equation 2.25). In general, tide corrections are derived from tide constituent grids interpolated on the location of each altimetry observation, and predicted using, for instance, the astronomical expressions shown in chapter 2. Tidal corrections are usually smaller in open ocean, along open ocean coastlines and in close seas like the Mediterranean; high tides occur at in semi-enclosed seas, funnel-shaped entrances of bays and estuaries, and continental shelves (Haigh, 2017). An example of ocean tide correction can be seen in figure 3.6, that shows values obtained with FES2014 tide model for the complete cycle 40 of Jason-1 mission. In the last years, models were known to have a global accuracy of 1-2 cm (Andersen and Scharroo, 2011), while at shelf and coastal areas, errors were still between 10-to-20 cm (Ray, 2008). However, more recent global models, such as FES2014, has shown dramatic improvements at critical areas, reaching an accuracy of few cm at the coast (Carrère et al., 2015).

3.2.7 Load tide correction

The load tide is an effect sensed by altimeters, and it is defined as the loading of the water column on Earth's crust. It is approximated as the 4% of the ocean tide signal (Cheng and Andersen, 2011), and can reach values of 10 cm (Ray and Sanchez, 1989). Tidal loading effects can be computed with formalisms like the one described in Francis and Mazzega, 1990, that use the Green's function approach. An alternative method is illustrated in Ray and Sanchez, 1989 and Cartwright and Ray, 1991, and exploits the concept of admittance (section 2.3.2).

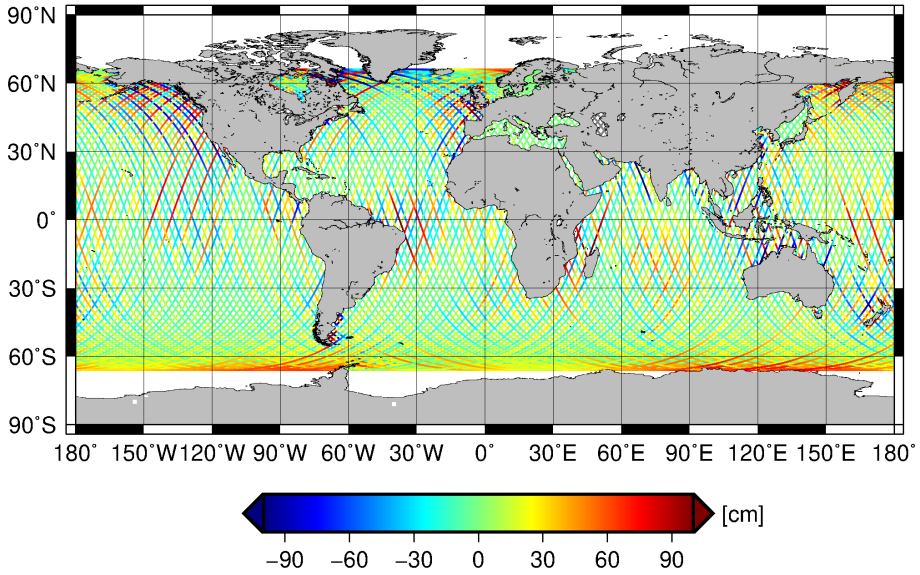

Figure 3.6: FES2014 ocean tide correction for cycle 40 of Jason-1 mission.

3.2.8 Solid Earth and Polar tide correction

The solid Earth tide is the response of the Earth to gravitational forces, and it is proportional to the tidal potential as described in Cartwright and Tayler, 1971. Its magnitude is around ±20 cm (Andersen and Scharroo, 2011), and it is described by highly accurate models that account for diurnal and semi-diurnal gravitational effects of Sun and Moon (Scharroo, 2018). The Pole tide correction accounts for the variation of the centrifugal force caused by changes in the Earth's axis (Polar motion), and it reaches its maximum at 45 degrees latitude (Scharroo, 2018). Also in this case, the models (e.g. Wahr, 1985) predicting this effect are highly accurate (Andersen and Scharroo, 2011).

3.2.9 Sea State Bias

The Sea State Bias (SSB) correction accounts for three different contributions: the electromagnetic bias, due to higher reflections of wave troughs, causing an overestimation of the range; the skewness bias due to the assumption that the targets in the illuminated area have a Gaussian distribution, while in reality it is characterized by a non-zero skewness (Passaro et al., 2018); and the tracker bias, related to the way returning echoes are tracked (Pires et al., 2019). The SSB correction can be modeled using parametric and non-parametric techniques dependent on wind and significant wave height; it has a mean value of 5-10 cm, with variations of 1 cm, at low- and mid-latitudes, and 20 ±5 cm at high latitudes (Andersen and Scharroo, 2011).

3.2.10 Mean Sea Surface

The MSS is defined as the height of the sea surface averaged in time. MSS models (like DTU18MSS, CLS15) are generally based on several years of multi-mission altimetric observations that are averaged and filtered in order to remove the sea surface variability, while maintaining the highest spatial resolution possible (Andersen and Knudsen, 2009). The current models achieve 1/60 degree resolution, and exploit at least 20 years of altimetry data (e.g. Andersen and Scharroo, 2011, and Schaeffer et al., 2016). The MSS values range between -105 m in India and 85 m in the North East of New Guinea, with an accuracy of 10-20 cm (Andersen et al., 2018).

3.3 Issues at the coast

Coastal dynamics are highly variable at scales much lower than in the open ocean, and thus extremely complex to model. For this reason, pure ocean models are often combined with remote sensing (e.g. altimetry and radar imagery) or in-situ observations to improve their solutions at the coast (Wilkin et al., 2005). The advantage of using altimetry is to have a global coverage, also in areas hard to reach with in-situ instrumentation. However, observing the coast with altimeters remains still a challenge. As the satellite approaches shallow waters, waveforms resemble no more to a typical Brown ocean waveform, and change according to two main drivers (Gómez-Enri et al., 2010):

- the sea state: unbroken wave crests, white caps, and calm water patches, are characterized by high reflectance that cause peaky waveforms; these phenomena are not constant in space and time, and occur close to the shore (Scozzari et al., 2012).

- the presence of land: in transition between ocean and land, waveforms can be contaminated by land returns, while the satellite nadir is still over the ocean. Land echoes are registered at certain gates, causing irregular sampling at the trailing edge, figure 3.7. Land samples increase toward the leading edge while the satellite gets closer to the coast. Land echoes depend on the nature of the terrain and the geometry of the coast, which make this issue highly variable and difficult to describe by retracking algorithms Gommenginger et al., 2011.

Other drivers, such as the presence and the condition of sea ice or leads, are related to Polar regions, and are not the focus of this work. More information can be found in e.g. Müller et al. (2017). An example of coastal waveforms is described in Gommenginger et al., 2011 (see figure 3.8), and compares Brown ocean waveforms detected by ERS-2 mission (3.8a) with the ones found when both ocean and land surfaces are illuminated (3.8b-f). Peaky waveforms, due to highly reflective water patches, have similar shapes as 3.8h. It is clear that with such

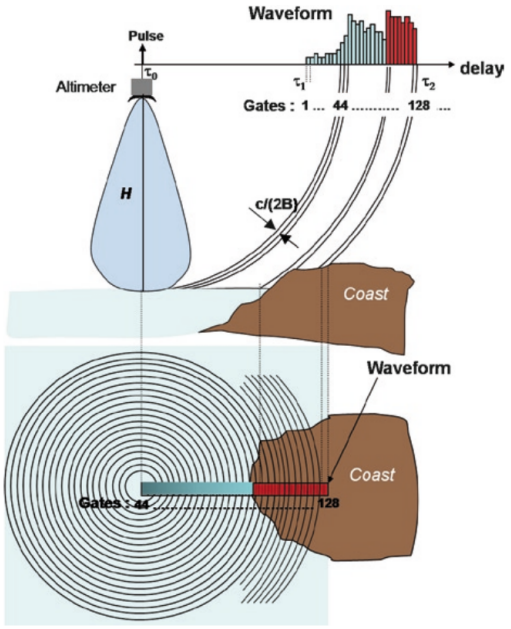

Figure 3.7: Scheme of altimetric observation in proximity of the coast. Credit: Gommenginger et al., 2011.

waveform variety, typical retracking algorithms are prone to fitting errors, and consequently in range estimation. In the last decades, major focus on coastal issues led to development of ad-hoc retracking algorithms, that are able to derive ranges with higher accuracy than ordinary retrackers, or from waveforms that would be discarded when severely affected by land returns. A successful example, is the Adaptive Leading Edge Subwaveform (ALES) retracker (Passaro et al., 2014), which restricts the application of Brown-Hayne model to only a portion of the fitted radar echo (selected according to a first estimation of the sea state) in order to guarantee the precision of the measurement also in the open ocean, while avoiding spurious reflections typical of the coastal zone. The fact that ALES can be used homogeneously over open ocean and coastal areas is crucial, as it avoids potential internal bias that can be introduced with using different retracking methods (Passaro, 2015). The reliability of this retracker has been proven in a number of applications such as the regional estimation of the seasonal cycle and trend of the sea level (Passaro et al., 2015 and Passaro et al., 2016). With reliability, it is meant a higher amount of data, while maintaining high quality open ocean standards of precision and accuracy at locations as close as possible to the coast. In figure 3.9, an example is shown for Jason-1, track 161 of its interleaved orbit, processed with different retracking algorithms and compared with a tide gauge in the North Adriatic (Passaro et al., 2014). The plot compares the percentage of cycles that have correlation ≥ 0.9 with respect to in situ timeseries (left y-axis), obtained with ALES (in red), SGDR standard product (in blue), and CTOH 1 Hz product (cyan round markers), against the distance to the coast (green curve, referenced to the right y-axis), and along

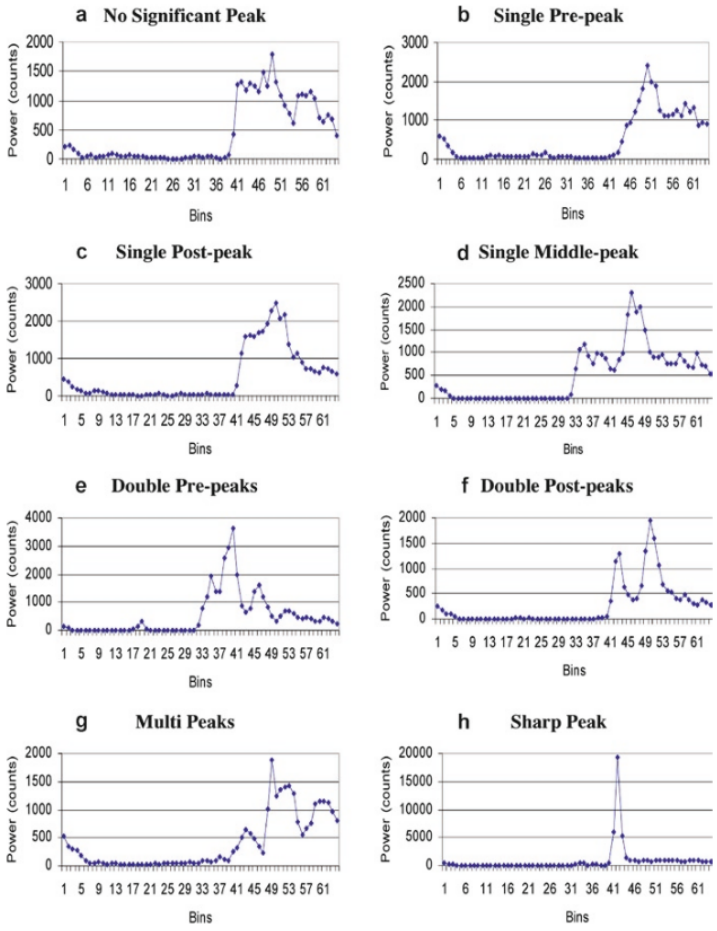

Figure 3.8: Waveforms at coastal areas observed with ERS-2 mission. Credit: Deng, 2004.

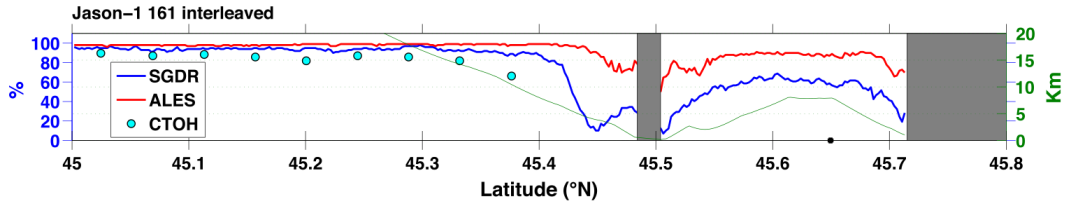

Figure 3.9: Percentage of Jason-1 cycles with ≥ 0.9 correlation with tide gauges. Results are for ALES (red), SGDR standard product (blue), and CTOH 1 Hz product (cyan round markers). Land areas are in grey and the distance to coast is in green. Credit: Passaro et al., 2014.

the latitude (x-axis); the grey areas represent land. From this plot it is possible to see that within 5 km from the coast of the island,located at 45.5N, ALES maintains an amount of cycles with high-quality data above 70% over 89 cycles analyzed; while with the standard product, the number of good-quality cycles is rapidly reduced below 7 km to the coast. A similar situation occurs between 45.5N and 45.7N. At the coast, also single altimetry corrections are problematic, as they are characterized by higher variability and magnitude than in open ocean, and during years, dedicated solutions have been proposed to mitigate coastal issues. In table 3.1 the variability in time of the main geophysical corrections in open ocean is compared with the ones at the coast. The wet tropospheric correction is one of the largest sources of error in coastal altimetry, as higher variations at coastal areas are not properly described by models, or observed (because of large radiometer footprints that are contaminated by the presence of land, Fernandes et al., 2015). A valid solution, provided by Fernandes and Lázaro, 2016 as GNSS Derived Path Delay Plus (GPD+) model, is to combine different sets of data, coming from onboard radiometers or GNSS coastal and island stations, with ECMWF operational and reanalysis models, in order to guarantee, and give the best estimate of wet tropospheric values at the coast. Other difficulties are found in SSB modeling at coastal areas, where issues are related to changing wave shapes and wind propagation, and the interaction with bathymetry and coastal geometry (Andersen and Scharroo, 2011); particular attention is dedicated nowadays on this topic (for example, see PISTACH and WaveWatch3 projects, or Tran et al., 2006). Ocean tides are the most significant parameter to correct at the coast, as they can reach magnitudes with several meters, and are subject to non-linear phenomena related to water depth, that causes signal resonance, and therefore overtides and compound tides (Andersen, 1999). Tide corrections are the result of tidal heights predicted from tide models that lose accuracy of several cm at the coast - for instance, M2 constituent from a gridded tide model has an accuracy of around 0.5 cm in open ocean, against 4.5 cm at the coast (St14). However, substantial improvements have been achieved since St14; an example is the FES2014 model, that refined its finite element mesh for a better description of bathymetry and coastal geometry, or the EOT model described in this work, that exploits coast-dedicated altimetry products to improve residual tidal estimation (more details about this topic are given in chapter 4). Other solutions to coastal issues came from progress in instrumentation; the Synthetic Aperture Radar (SAR), exploits the Doppler-limited design already mentioned in 3.1, that improves resolution along track, resulting in a valuable solution close to the coast. However, it must be mentioned that this advantage occurs according to satellite orientation with respect to the coast, as across-track SAR footprint remains pulse-limited. SAR technology is also combined with across-track interferometry to derive the location from where the scatter originated (this configuration is named SARIn; more details and applications about this technique

Correction	Open Ocean	Coast
Dry troposphere	0-2	0-2
Wet troposphere	5-6	5-8
Ionosphere	2-5	2-5
DAC	5-15	5-15
SSB	1-4	2-5
Tides	0-80	0-500

Table 3.1: Time variability of geophysical corrections in open ocean and at the coast. Values in cm. Credit: Andersen and Scharroo, 2011.

can be found in Di Bella, 2019). Both SAR and SARIn configurations, together with the ordinary pulse-limited mode, operate aboard CryoSat-2 mission. A further improvement in the SAR concept is the fully focused coherent processing of its returned signal, that allows to distinguish specific targets within highly heterogeneous scenes, like in case of coastal zones (Egido and Smith, 2017). Finally, in September 2021 the Surface Water Ocean Topography (SWOT) mission will be launched. Its payload will carry a wide-swath interferometric altimeter, that consists of a nadir-looking altimeter and two SAR antennas. The mission will provide high-resolution observations between 250 m to 2 km, that allow coastal current and storm surge monitoring (Morrow et al., 2018).

3.4 Altimetry missions

Altimetry missions are now operating since 41 years. It was in June 1978 when the first altimetry mission, SeaSat, was launched. After this date, a sequence of missions, born from the international collaboration through agencies, was developed to respond to different scientific needs, and continuously monitor our planet through years. The NASA-CNES Jason-series, starting with T/P mission, was built with the main purpose of improving our understanding of oceans. It was launched in August 1992, and operated for over 13 years (until January 2006), delivering data with an accuracy of 4.2 cm (NASA, 2013). The satellite flew on a near-circular, non- Sun-Synchronous orbit with altitude of 1336 km, coverage of $\pm$66 degrees, and a repeating period of 9.9156 days (AVI-NT-02-101-CN, 1996). In September 2002, its orbit was shifted midway between the previous tracks (interleaved or interlaced orbit). This operation allowed a cross-calibration with NASA's Jason-1 satellite, which replaced T/P in on its same former orbit (SALP-MU-M5-OP-13184-CN, 2016). (A first calibration between the two missions took place during the tandem phase, in which T/P and Jason-1 followed the same orbit separated by a short-time distance). After May 2012, Jason-1 moved into a geodetic orbit, after a tandem phase with Jason-2, that started

in June 2008 in which the satellites flew on the same orbit, one after the other, with 1-minute time distance (SALP-MU-M-OP-15815-CN, 2011). From October 2016 Jason-2 is in an interleaved orbit, while the newer mission, namely Jason-3, continues operating on the former ground-track (SALP-MU-M-OP-16118-CN, 2018). Jason-3 was launched in January 2016 (SALP-MU-M-OP-16118-CN, 2018), and is still ongoing. The Jason-series is currently providing data at same locations with an uninterrupted timeseries of circa 27 years. Another successful mission series was realized by ESA. The first European Remote-Sensing Satellite (ERS-1) was launched in July 1991 and it was the most advanced European satellite for the Earth observation. In particular, this mission provided information of ocean and atmosphere in the microwave spectrum, and several applications were found also for ice and land. ERS-1 is characterized by a Sun-synchronous near-circular polar orbit, with 98.55 degree inclination (coverage of ±81.45 degrees) and altitude of 782 -785 km (ESA, 1993). During the first phases of the mission, ERS-1 had a high-frequency repeat cycle of 3 days, which changed to a 35-day repeating orbit during the mapping phase. ERS-1 ended in March 2000, after few additional phases. In 1995 ERS-2 replaced the satellite on its same nominal track until September 2011 (REA-UG-PHB-7003, 2014). Like ERS-1, ERS-2 had a repeat cycle of 35 days during the mapping phase. Since March 2002, the Environmental Satellite (EnviSat) flew on the same orbit as ERS-2. EnviSat is the largest civilian Earth Observation satellite ever built, and its mission objectives covered a wide range of disciplines, for both meteorological and climatic studies: EnviSat gathered information on regional and global scale phenomena, strongly contributing to a better understanding of oceans, atmosphere, vegetation, Earth crust, hydrology, and ice processes (Batoula, 2009). In May 2012, EnviSat mission was officially declared terminated. The ESA missions observed the Earth for circa 20 years. Besides these two mission blocks, many more satellites were launched after 2002, such as ICESat and CryoSat-2 for cryosphere studies, Saral/AltiKa to monitor oceans in Ka frequency band, and the latest Sentinel-series, part of the European Commission Copernicus programme. In figure 3.10, all altimetry missions are represented in a timeline manner. The missions used in this work are highlighted in red. All missions shown are available under request on DGFI-TUM's OpenADB online database (https://openadb.dgfi.tum.de/en/). In OpnADB you can also find a more detailed description of the single missions (with similarities with the current section, as it was written by the author of this thesis), and further information about single mission phases. Some missions were not included in this work, because of a combination of the following reasons:

1. pathological aliasing: the choice of Sun-synchronous orbits is convenient in terms of energy efficiency; however, it makes impossible to derive information on Sun-related tidal constituents such as S2 (further details in section 3.5).

2. long- or non-repeating orbit: typical of missions' geodetic phases, that are characterized by long repeating periods of e.g. 406 days for Jason-1, or CryoSat-2, which features a repeat period of 369 days.

3. lower data quality: this is the case of old missions like GeoSat or GFO.

4. the lack of ad-hoc data: particularly for the latest missions, some geophysical corrections, or ALES range, were not available; this point often combines with point 1 (e.g. Sentinel-3 and Saral/AltiKa).

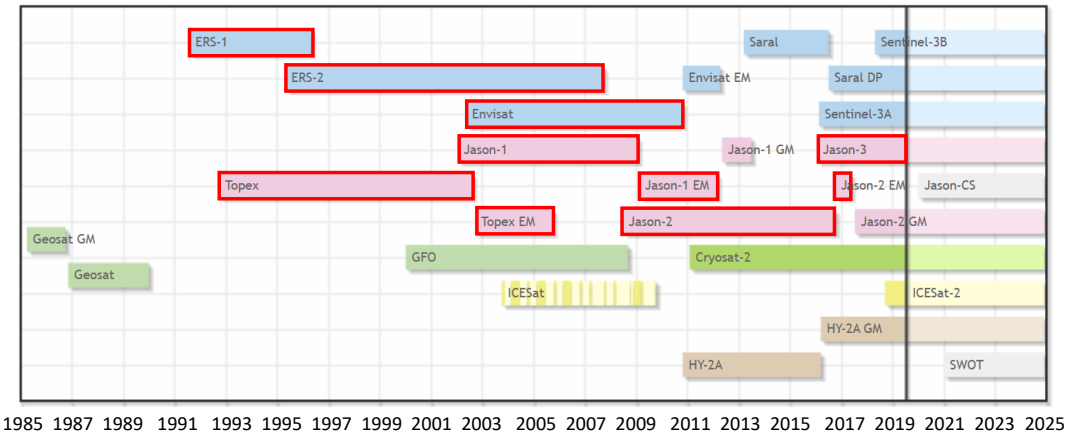

Figure 3.10: Timeline of altimetry missions available from OpenADB. The missions used in this work are highlighted in red. Image modified from: https://openadb.dgfi.tum.de/en/missions.

The missions chosen guarantee not only a significant coverage in time, but also in space, in terms of observation density. In figure (3.11) Jason-series, both first-phase and interlaced-phase, and ERS-series tracks, are shown for an ocean area chosen around the equator. With only ~1-degree distance between two consecutive tracks, ERS satellites compensate the Jason coverage, whose tracks are around one 3 degrees apart. This is an aspect that becomes crucial at coastal areas, where the presence land makes altimetry coverage more difficult.

3.5 Monitoring tides with altimetry

With altimetry it is possible to reconstruct the tidal signal through the analysis of sea level timeseries, regularly sampled in time at every repeating pass on the same location. According to the Nyquist sampling theorem, a signal is correctly sampled if the sampling frequency f_s is at least twice than the maximum frequency of the signal f_m (Chitode, 2008),

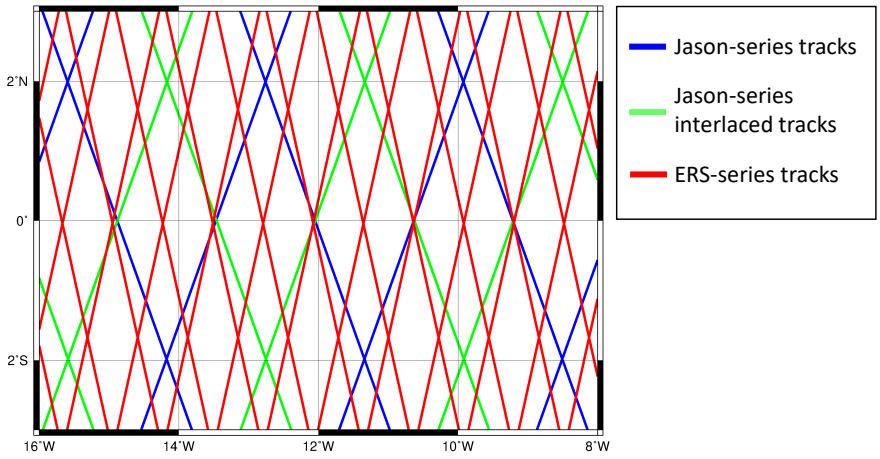

Figure 3.11: Example of altimetry track coverage Around the Equator. Image created using CTOH nominal track data (http://ctoh.legos.obs-mip.fr/data/altimetry).

that is:

$$f_s \geq 2f_m \tag{3.6}$$

When this condition does not hold, the signal is aliased, i.e. not properly represented (Stewart, 2004). With satellite altimetry, every location is observed with a repeat period of 9.9156 days for the Jason-type missions, and 35 days for the Envisat-type missions. It is then clear that tidal signals of major constituents observed with altimeters are under-sampled, and therefore aliased. However, the reconstruction of the full tidal signal with satellite altimetry is still possible, if the observation period of the mission is long enough. The minimum observation period to reconstruct tidal constituent signals is called alias period T_a, and it is computed in the following way. First of all, we have to define the phase shift of the tidal signal $\Delta\phi_t$, that gives information about the change of the signal phase in a certain interval $\Delta t = t_2 - t_1$. The value of $\Delta\phi_t$ directly depends on Δt and the frequency ω of the signal:

$$\Delta\phi_t = \omega\Delta t \tag{3.7}$$

If we want to sample the signal every Δt (Δt would correspond to e.g. 9.9156 days for a Jason-type mission), larger than the signal period:

$$T_s = \frac{2\pi}{\omega} \tag{3.8}$$

we need to compute how much the signal has shifted between t_1 and t_2. This is done by deriving the remainder (MOD) of T_s within Δt (figure 3.12):

$$MOD(T_s) = \Delta t - I(\frac{\Delta t}{T_s}) \tag{3.9}$$

With I(x) the integer of quantity x. And using the definition of equations 3.7 and 3.8 one can write:

$$\Delta\phi_a = \frac{2\pi}{T_s} MOD(T_s) \tag{3.10}$$

That is the phase shift of the aliased period:

$$T_a = \frac{2\pi}{\Delta\phi_a}\Delta t \tag{3.11}$$

In figure 3.13 an example of aliased signal (red curve) of M2 tidal signal with unitary

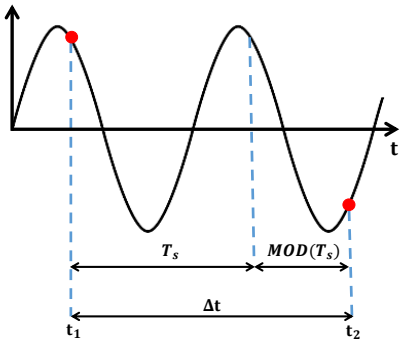

Figure 3.12: Schematic of signal shift between the first sample at t_1 and the second sample at t_2.

amplitude (in light blue) is shown for T/P rate of sampling (the vertical black lines highlight the time of sampling). It is easy to observe a much longer period for the aliased signal. Because the alias period depends on both sampling and signal frequencies, T_a changes for every mission type and tidal constituents. In table 3.2 alias periods of the main tidal constituents are shown for Jason- and ERS-series missions. Another issue to face with

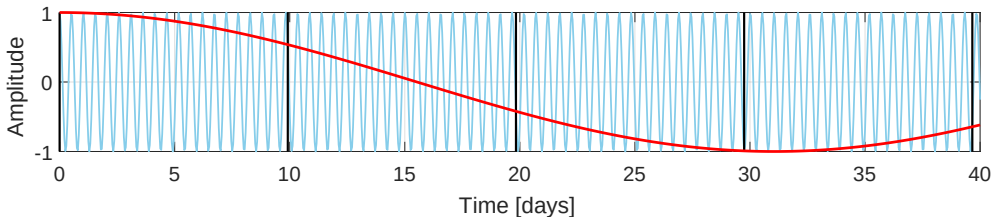

Figure 3.13: Example of aliased signal. The light blue sinusoid is M2 constituent signal with unit amplitude, while the red curve is the signal reconstructed with T/P-type satellites, with sampling every 9.9156 days. The time of sampling is highlighted with vertical black lines.

altimetry, and related to aliasing is the separation of tidal constituent signals. According to Rayleigh criterion, in order to be able to resolve two tidal signals, a minimum length of timeseries is required, which is called Rayleigh (or synodic) period T_r (Godin, 1972). The idea is that two signals can be separated from each other if the timeseries analysed is so long that the signals differ in phase by one cycle (Smith, 1999):

$$\mid \phi_{a1} - \phi_{a2} \mid \;\geq\; \frac{2\pi}{T_r} \tag{3.12}$$

Constituent	Jason-series	ERS-series
M2	62	94
S2	58	∞
K2	86	182
N2	49	97
2N2	22	392
S1	117	∞
O1	45	75
K1	173	365
P1	88	365
Q1	69	133
M4	31	135

Table 3.2: Aliasing periods of main tidal constituents for Jason- and ERS-type missions in days, rounded to integers.

That becomes, according to equation 3.7:

$$|\frac{1}{T_{a1}} - \frac{1}{T_{a2}}| \geq \frac{1}{T_r} \tag{3.13}$$

Of course, in order to separate tidal constituents with altimetry, we need to consider aliasing phases and periods (ϕ_{a1}, ϕ_{a2}, T_{a1}, T_{a2} respectively). In table 3.3 an example of Rayleigh periods for Jason-type missions is shown. Talking about tide gauge tidal analysis, (Pugh

	M2	S2	N2	K2	K1	O1	P1	Q1
M2	-	1084	245	220	97	173	206	594
S2	-	-	316	183	89	206	173	384
N2	-	-	-	116	69	594	112	173
K2	-	-	-	-	173	97	3355	349
K1	-	-	-	-	-	62	183	116
O1	-	-	-	-	-	-6	94	134
P1	-	-	-	-	-	-	-	316

Table 3.3: Rayleigh periods of main tidal constituents for Jason-type mission in days, rounded to integers. Credit: (Andersen and Knudsen, 1997).

and Woodworth, 2014b) argue that the Rayleigh criterion can be too restrictive, especially when instrumental noise and the background meteorological noise are low. So, it is useful in tidal analyses of continental shelf data from middle and high latitudes, but finer resolution is feasible in ideal conditions such as tropical regions. This concept of noise has been extended

also to satellite altimetry; in fact, (Foreman et al., 2009) propose another version of the Rayleigh period expression that accounts for a signal-to-noise ratio (SNR):

$$\mid \phi_{a1} - \phi_{a2} \mid \quad \geq \quad \frac{2\pi}{T_r\sqrt{SNR}} \tag{3.14}$$

with SNR the ratio of the tidal variance to the non-tidal variance of the signal.

Chapter 4

The creation of an improved tidal model

The Empirical Ocean Tide model is a series of global tide model that provide harmonic constants of tidal constituents, on grids with a typical resolution of 7.5 minutes of degree, that can be changed according to the user's need. The concept behind EOT (and all semi-empirical models) is based on the assumption that SLA data, despite being already corrected for tides with a so-called background (or prior) model, still contain residual tidal signals. Amplitude and phase of residual signals can be computed from SLA timeseries, and then be used to correct the background model (i.e. the SLA tide correction, cf. 3.2.6) and obtain a better tidal estimation. In case of EOT, timeseries analysis is done through harmonic analysis of multi-mission altimetry SLA values, derived using ocean and load tide corrections provided by FES-series tide models. In this project, the EOT strategy has been followed, with focus on improving tidal estimations at the coast. For this reason, the latest altimetric data, dedicated to coastal applications are used. Besides altimetric data, the main novelties introduced with respect to the last version of EOT (EOT11a), are: an updated background model, FES2014, known for its high performances in shallow and coastal waters thanks to an improved bathymetry model and refined mesh; a new grid for tidal residual computation, whose advantage is to reduce computational time while maintaining a good resolution; a latitude-variable radius of interest to select SLA observations, in order to mitigate the issue of dense data distribution at high latitudes. The resulting model is a preliminary, regional version, and it is called EOT19p. The EOT19p method follows few steps that are illustrated in detail in this chapter: for each grid point (or node) SLA data are firstly collected and weighted (section 4.1), then residual tidal constants are computed using weighted least-squares (WLS) combined with Variance Component Estimation (VCE) (sections 4.2); finally, FES2014 grids of tidal constants are corrected for the computed residuals (4.3). In section

4.4 description and comments on the error computation is illustrated, and in section 4.5 additional studies for coastal issue mitigation are shown.

4.1 SLA collection and weighting

4.1.1 SLA data

■ Multi-mission observations at 1-Hz frequency were used to derive residual tidal estimations. The data are taken from DGFI-TUM's Open Altimeter Database (OpenADB: `https://openadb.dgfi.tum.de`) that contains the original Geophysical Data Records (GDR) and derived higher-level products. In total, circa 27 years of data are exploited, from missions: TOPEX/Poseidon, Jason-1, Jason-2, Jason-3, Jason-series extended missions, ERS-1 phase C and phase G, ERS-2 and Envisat. SLA values are computed according to Andersen and Scharroo, 2011, and coastal corrections are applied where available. In case of missing coastal products, standard products are applied. ALES range and Sea State Bias are not provided for the TOPEX/Poseidon mission, therefore the original Sensor Data Records (SDR) are used. The Dynamic Atmospheric Correction based on the ECMWF ERA-INTERIM reanalysis (DAC-ERA, Carrère et al., 2016) inverse-barometer model is missing in the last cycles of Jason-2 (and its extended phase) and for Jason-3, and it is then replaced by DAC-MOG2D (DAC - 2 Dimensions Gravity Waves model) model (Carrère and Lyard, 2003). The parameters and the models used, together with their references, are listed in table 4.1 ■. It must be added that the choice of the products is also a compromise between higher coastal performance, and an improved compatibility among different missions. In fact, the NOAA Ionosphere Climatology 2009 (NIC09,Scharroo and Smith, 2010) ionospheric correction and the Vienna Mapping Function version 3 (VMF3, Landskron and Böhm, 2018) dry tropospheric correction were the most suitable models to exploit, as they are available for all missions, and they have higher performance at the coast than observation-based corrections (Denise Dettmering, personal communication). Finally, SLA data were corrected for radial errors. Radial errors are systematic errors due to several causes such as oscillator drifts or orbit errors, and affect altimeter range estimates (Bosch et al., 2014). With DGFI-TUM's multi-mission cross-calibration (described in detail in Dettmering and Bosch, 2010), it is guaranteed further consistency between different missions.

4.1.2 SLA weighting

■ Instead of a regular grid, residual tidal estimates are computed on a triangular grid based on the geodesic polyhedron (e.g. Wenninger, 2014). The grid nodes are therefore vertices of triangles, and the distance between each other ranges between 27 and 33 km. This grid type was preferred over a regular one, mainly to reduce computational time: the number

Parameter	Model	Reference
Range and Sea State Bias	ALES	Passaro et al., 2014
Inverse barometer	DAC-ERA	Carrère et al., 2016
Wet troposphere	GPD+	Fernandes and Lázaro, 2016
Dry troposphere	VMF3	Landskron and Böhm, 2018
Ionosphere	NIC09	Scharroo and Smith, 2010
Ocean and Load tide	FES2014	Carrère et al., 2015
Solid Earth and Pole Tide	IERS 2010	Petit and Luzum, 2010
Mean Sea Surface	DTU18MSS	Andersen et al., 2018

Table 4.1: List of corrections used to compute SLA for tidal estimation residuals.

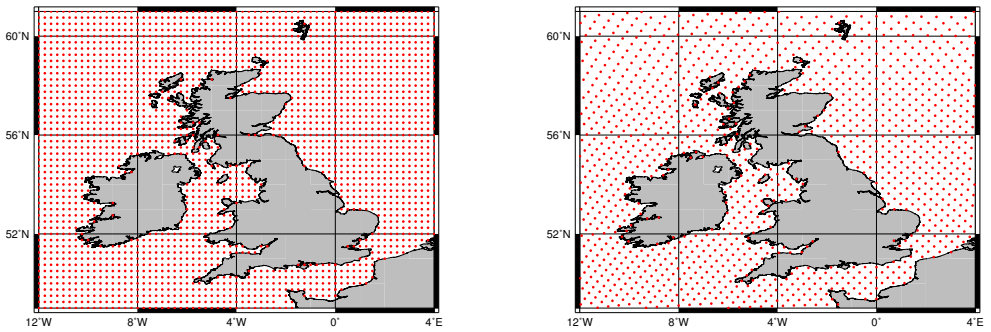

(a) (b)

Figure 4.1: Distribution of grid nodes for a regular grid of 1/4 degree resolution (a) and a grid based on the geodesic polyhedron, used to derive EOT19p (b).

of nodes involved is much smaller than a regular grid; in fact, a regular grid of 1/4 degree resolution contains 684977 nodes excluding nodes on land, against the 463667 nodes needed for the geodesic polyhedron. Also, the node distribution and mutual distance is such that the coastline and high latitudes are better described. In figure 4.1 the two grid types are compared. For each grid node SLA values are collected within a variable radius ψ_{max}. The radius changes linearly in function of latitude φ:

$$\psi_{max}(\varphi) = 165 - 1.5\,|\varphi| \tag{4.1}$$

At the Equator the radius measures 165 km, while e.g. at $\pm 66^{o}$ (the inclination of Jason-series missions) the radius is of ca. 66 km. This choice was inspired by Andersen and Knudsen, 1997, to compensate a greater data density at high latitudes. Only SLA values within ± 2.5 m situated farther than 3 km from the coast are considered. Usually, with standard products, it is suggested a minimum distance to the coast of 6 km. However, given the already demonstrated results of ALES retracker and the other latest coastal products (e.g. Fernandes and Lázaro, 2016), one could *dare* to get 3 km closer to the shore. A weight is assigned to all accepted SLA values, so that observations far from the grid node

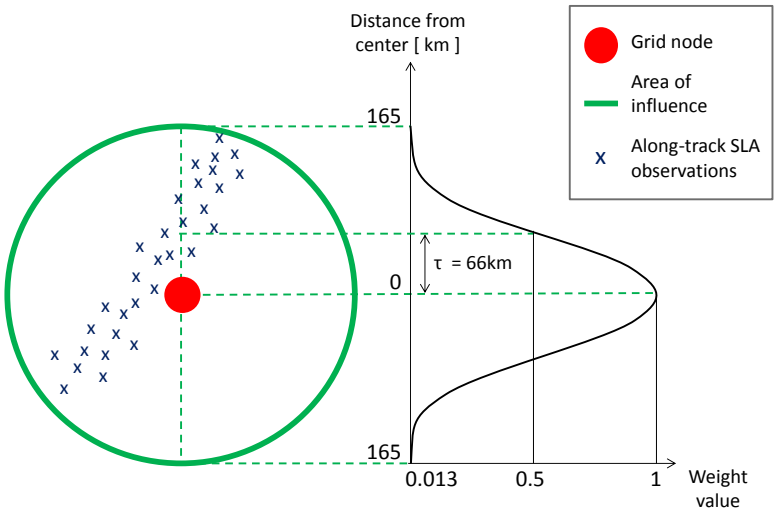

Figure 4.2: Grid node with SLA Gaussian weighting representation using the radius at the Equator of 165 km. The crosses represent the location of satellite observations at one-mission track. Credit: Piccioni et al., 2019b

have smaller impact on the local tidal estimation. Weights w_i of each observation i are derived according to the Gaussian function illustrated in Savcenko and Bosch, 2012, which is dependent on the distance to the node ψ_i :

$$w_i = e^{-\beta\psi_i^2} \tag{4.2}$$

β is defined as:

$$\beta = \frac{\ln 2}{\tau^2} \tag{4.3}$$

with $\tau = 0.4\psi_{max}$. The quantity τ is called half-weight width and determines the steepness of the Gaussian function. Namely, it defines the distance from the node for which the weight has value 0.5; in this case the value of τ is 66 km, as ψ_{max} = 165 km. In figure 4.2 the sketch of SLA collection and weighting is shown ■. It must be mentioned that in EOT11a, τ was slightly smaller, as the factor multiplied with ψ_{max} was 0.3 (τ = 49.5 km). A factor of 0.4 makes the steepness of Gaussian function more gentle, so that data farther from the node have higher weight - it has been tested that in certain cases, this may be helpful in proximity of land, especially for coasts with complex geometry. The weights are used to compute the weighted mean of SLA belonging to the same track, which are then exploited to compute tidal constants via least squares. This method reduces the computational time of the program with respect to the use of single SLA data, but it also mitigates correlation issues in the least squares estimation (Savcenko and Bosch, 2012), (see section 4.2).

4.2 The method of weighted least squares (WLS)

The least squares approach is widely used in several disciplines to solve inverse problems. From a series of observations of a certain phenomenon, it is possible to reconstruct the causes of such phenomenon. In tidal analysis, the least squares are applied to the harmonic formulae, in order to derive information on single constituents (amplitude and phase), starting from SLA observations. The method of least squares is based on the principle that repeated k measurements y_i can be described as a linear combination of j unknown variables multiplied by known scalars $d_{j,k}$:

$$y_i = d_{1,i}x_1 + d_{2,i}x_2 + \ldots + d_{j,i}x_j + \varepsilon_i$$

so that the sum of the square errors ε_i is minimum (Brandt, 2014):

$$\sum_{i=1}^{k} \varepsilon_i^2 = \sum_{i=1}^{k} \left[y_i - (d_{1,i}x_1 + d_{2,i}x_2 + \ldots + d_{j,i}x_j) \right]^2 = min$$

that can be written in the alternative matrix form :

$$\sum_{i=1}^{k} \varepsilon_i^2 = (Y - DX)^2 = min$$

with X, Y the vectors $(x_1,\ x_2,\ \ldots,\ x_j)$ and $(y_1, y_2,\ \ldots,\ y_k)$ respectively, and D is the so-called design matrix that has dimension $[j,\ k]$:

$$D = \begin{bmatrix} d_{1,1} & d_{2,1} & \ldots & d_{j,1} \\ d_{1,2} & d_{2,2} & \ldots & d_{j,2} \\ \ldots & \ldots & \ddots & \ldots \\ d_{1,k} & d_{2,k} & \ldots & d_{j,k} \end{bmatrix}$$

The sum of the square errors (or residuals) can be rewritten as the scalar product between two vectors (Heij et al., 2004):

$$\sum_{i=1}^{k} \varepsilon_i^2 = e'e = (Y - DX)'(Y - DX) = -Y'DX - D'X'Y + D'X'DX = min$$

and rearranged as:

$$\sum_{i=1}^{k} \varepsilon_i^2 = Y'Y - 2X'D'Y + D'X'DX = min$$

And the minimum of this function is found if its derivative is set to 0. Therefore:

$$\frac{\partial\left(\sum_{i=1}^{k} \varepsilon_i^2\right)}{\partial X} = -2D'Y + 2D'DX = 0$$

That gives the normal equation:

$$D'DX = D'Y$$

with the unknowns in X that can be then obtained from:

$$X = (D'D)^{-1}D'Y$$

The previous expressions represent the Ordinary Least Squares method (OLS). The Gauss-Markov theorem states that, under certain conditions, OLS is the Best Linear Unbiased Estimator (BLUE), that means that OLS estimators (unknowns X) are unbiased and their variance is smaller than any other estimator. The five conditions to have a BLUE are the following (Wooldridge, 2008):

1. Parameter linearity: the dependent variable Y can be described as a linear function of the independent variables (or regressors) D
2. Random sampling: data must be randomly sampled from the population
3. Exogeneity: errors are independently distributed and are not correlated with the regressors
4. Zero conditional mean: the expected value, or the mean, of the error is 0
5. Homoskedasticity: the variance of the error is constant for every observation

If we refer to this work, OLS can't be a BLUE. In fact, exogeneity in geophysical data is not often possible, as they are spatially correlated and errors are subject to autocorrelation, as shown in e.g. Passaro, 2015. Also, observations are not homoskedastic, as their error may not be constant (Marcos et al., 2011). In general, the first issue is mitigated by setting up an error variance-covariance matrix whose off-diagonal elements are the covariance between two observations. This approach is highly demanding in terms of computation power, because this kind of matrices have dimension [k, k], which can be very large, if a multi-mission dataset is used. Of course, optimization strategies and specific coding libraries (e.g. the Fortran LAPACK library) are available for such purposes, however, the huge amount of data to process - repeatedly at each node - still remains an issue. For example, for one node located in open ocean, the cap size of 330 km can contain 47 1-Hz observations of only one track; for the Jason series, 47 observations must be multiplied by 904 repetition cycles (904 is the sum of cycles of: T/P, Jason-1, Jason-2, and Jason-3 missions), that gives: 42488 observations. For a cap size of such dimensions 2-to-4 Jason tracks, and 6-to-8 ERS-like tracks may be included, the number of observations - and thus, the dimension of the covariance matrix - increases considerably. therefore, an alternative was found by Savcenko and Bosch, 2012, who computed the average of SLA observations along the same track and cycle in order to reduce spatial and temporal correlation.
The second issue is solved by introducing a weight matrix W:

$$W = \begin{bmatrix} w_{1,1} & 0 & \dots & 0 \\ 0 & w_{2,2} & \dots & 0 \\ \dots & \dots & \ddots & \dots \\ 0 & 0 & \dots & w_{k,k} \end{bmatrix}$$

that is, a diagonal matrix, whose elements $w_{i,i}$ are usually the reciprocal of the variance of each observation error, i.e. they are directly dependent on observations accuracy (Van de Geer, 2005). In this case, $w_{i,i}$ are computed according to equation 4.2, and are the maximum weights obtained for one track, relative to the averaged SLA value. The OLS can therefore be extended in a more generalized form, that is, the Weighted Least Squares (WLS), whose normal equation can be derived with similar steps as for OLS:

$$D'WDX = D'WY \tag{4.4}$$

and the vector of unknowns can be obtained using:

$$X = (D'WD)^{-1}D'WY \tag{4.5}$$

In context of this work, the WLS is used to compute amplitude and phase of each constituent, starting from SLA observations (here, one observation is called y_i) and the time t_i of their acquisition. One SLA observation of mission m can be described by the linear relation:

$$y_i = z_m + at_i + \sum_{n=1}^{N} [A_n \cdot f_n \cos(\omega_n t + V_n + u_n) + B_n \cdot f_n \sin(\omega_n t + V_n + u_n)] \tag{4.6}$$

that is the combination of the tidal height (equation 2.25) with the linear trend a of the timeseries and the mean sea level z_m obtained for each mission. A_n and B_n are the unknown in-phase and quadrature coefficients that give information on amplitude H_n and phase g_n of each tidal constituent (equations 2.28 and 2.29). A_n, B_n, a, and z_m are the unknowns to be estimated via least squares. Their number varies according to the number of missions and constituents considered. The new EOT exploits data from 11 missions, and computes amplitude and phase for 15 tidal constituents (M2, S2, N2, K2, 2N2, O1, K1, Q1, P1, S1, M4, MM, MF, SA, SSA). Therefore, the number of unknowns, is 42 ($11 + 1 + 2 \cdot 15$), which is also the size of vector X, that has the form:

$$X = \begin{bmatrix} z_{TP} & z_{J1} & \dots & z_{EN} & a & A_{M2} & B_{M2} & \dots & A_{SSA} & B_{SSA} \end{bmatrix}'$$

With superscripts: TP, $J1$, and EN indicating missions T/P, Jason-1, and Envisat (the other missions are left out in this expression for simplicity), while $M2$ and SSA represent the tidal constituents. Finally, the design matrix D is:

$$D = \begin{bmatrix} 1 & 0 & \dots & 0 & t_1 & \Theta_{M2}(t_1) & \Psi_{M2}(t_1) & \dots & \Theta_{SSA}(t_1) & \Psi_{SSA}(t_1) \\ 1 & 0 & \dots & 0 & t_2 & \Theta_{M2}(t_2) & \Psi_{M2}(t_2) & \dots & \Theta_{SSA}(t_2) & \Psi_{SSA}(t_2) \\ \vdots & \vdots & \vdots & \vdots & \vdots & \vdots & \vdots & \vdots & \vdots & \vdots \\ 1 & 0 & \dots & 0 & t_k & \Theta_{M2}(t_k) & \Psi_{M2}(t_k) & \dots & \Theta_{SSA}(t_k) & \Psi_{SSA}(t_k) \end{bmatrix} \tag{4.7}$$

For simplification, Θ_n and Ψ_n in D represent:

$$\Theta_n(t_i) = f_n \cos(\omega_n t_i + V_n + u_n)$$

$$\Psi_n(t_i) = f_n \sin(\omega_n t_i + V_n + u_n)$$

The first columns of D contain factors (1 or 0) to be multiplied with the single z_m terms. The D matrix in equation 4.7 describes the linear operators of only one mission (i.e. only the first column of z_m elements has value 1). In fact, a normal equation is set up for each mission, and then the WLS is solved in combination with the Variance Component Estimation.

It is important to mention that the inverse of the matrix product $D'WD$ (equation 4.5) is actually a Moore-Penrose pseudo-inverse matrix (Penrose, 1955). This generalized approach has been adopted because both D and W matrices may contain very small values (due to small astronomical angles or data weights) that can give rank deficiency of matrix $D'WD$, and consequently the WLS problem could have an infinite number of solutions. For this reason, it is applied the minimum norm principle, that states that any complete orthogonal factorization of matrix $A = D'WD$ can give a numerical solution of X that minimizes the sum of the square errors (or the norm-2 of the errors) and it is unique (Golub and Van Loan, 2013). The orthogonal factorization used in this work is the Singular Value Decomposition, that decomposes matrix A as a product of matrices (Lauffenburger and Dedon, 2006):

$$A = U\Sigma V'$$

where U and V are orthogonal square matrices, whose columns are the eigenvectors of AA' of and $A'A$ respectively, and Σ is a diagonal matrix whose elements correspond to the singular values of A (i.e. the square roots of eigenvalues of AA' or $A'A$) arranged in descending order. (In general, if A had dimension $j_1 \times j_2$ with $j_1 \neq j_2$, U would have dimension $j_1 \times j_1$ and V $j_2 \times j_2$. In this case, A is square and both matrices have same dimension as A). The pseudo-inverse matrix is defined as:

$$A^+ = V\Sigma^+ U$$

where the elements of Σ^+ are the reciprocal of the non-zero elements of Σ.

Variance Component Estimation (VCE)

With VCE it is possible to combine different datasets from one or more techniques, with using a relative weight according to the performance of the single dataset. An application of this approach is found in Koch and Kusche, 2002, who combined data from two missions with different measurements techniques (GOCE and GRACE) to derive information on the Earth gravity field. Another example is given in Bosch et al., 2014, in which VCE is used to compute a multi-mission cross-calibration of altimetric missions. In this section, the specific VCE procedure used for EOT tidal estimation is described. More details about VCE and its full mathematical discussion can be found in Teunissen and Amiri-Simkooei, 2008. Let's

start rewrite the WLS normal equation (equation 4.4) for one mission m as:

$$N_{x,m}X_m = N_{y,m}$$

where $N_{x,m}$ and $N_{y,m}$ are:

$$N_{x,m} = D_m^{'} W_m D_m$$

$$N_{y,m} = D_m^{'} W_m Y_m$$

The principle of VCE says that it is possible to combine observations from different datasets in one normal equation (hereafter referred as main normal equation):

$$N_x X = N_y$$

with terms N_x and N_y equal to the weighted sum:

$$N_x = \sum_{m=1}^{M} \frac{1}{\sigma_m^2} N_{x,m}$$

$$N_y = \sum_{m=1}^{M} \frac{1}{\sigma_m^2} N_{y,m}$$

M is the total number of missions involved, and $\frac{1}{\sigma_m^2}$ are the weights applied to each mission dataset; σ_m^2 are the variances of the least squares, generally defined as (e.g. Eicker, 2008):

$$\sigma_m^2 = \frac{\varepsilon_m^{'} W_m \varepsilon_m}{r_m}$$

where the numerator is the definition of WLS, i.e. the sum of the square errors of each mission, with X, the solution obtained with the main normal equation:

$$\varepsilon_m^{'} W_m \varepsilon_m = (D_m X - Y_m)^{'} W_m (D_m X - Y_m)$$

and the denominator represents the partial redundancy of the system, defined as:

$$r_m = k_m - \frac{1}{\sigma_m^2} tr(N_{x,m} N_x^{-1})$$

The partial redundancy is a sort of partial degree of freedom of the system related to a certain dataset. In fact, the sum of all r_m gives the degree of freedom of the main normal equation, which should be equal to (Koch and Kusche, 2002): $\sum r_m = k - j$. As it can be observed, with computing σ_m^2, we are measuring how large is the error of X relative to the normal equation of each mission. VCE is an iterative process, as both X and the term σ_m^2 are unknown. The iteration can be summarized as follows (figure 4.3, from left to right): a random value is assigned to each σ_m^2. Here, the initial value of σ_m^2 is set up as M, so that all missions have equal weights $\frac{1}{M}$. Then the normal terms of the single missions are weighted and summed together to form the main normal equation. The WLS is implemented, and finally the new variance σ_m^2 is computed for each mission. The new σ_m^2 can be replaced

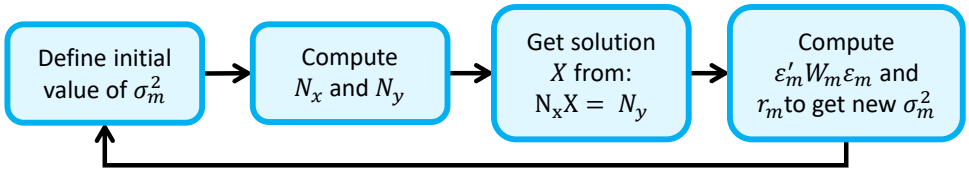

Figure 4.3: Flowchart of VCE iteration.

to form the new weights and the new normal equations. After few iterations, the solution converges, and the weight of the single mission is available. ■ The advantage of VCE is that tidal estimates of single missions are weighted according to their performance: the higher is the least-squares variance of one mission, the lower is its weight on the final tidal estimation. This is important in case of a multi-mission approach, where sun-synchronous, or short missions, (which can be problematic for tidal constituent resolution or separation), have a lower impact on the final result. With VCE it is possible to see the contribution of single missions at coastal areas; an example is shown in figure 4.4, where the weights of Jason-1 are shown for the Malay Archipelago region. The weights are expressed in percentage over a total of 11 missions. It can be observed that the highest impact of this mission is at the coast, and around small islands or peninsulas. The track-shaped features in open ocean are typical for the Jason-series missions, because of their lower coverage with respect to e.g. ERS-type missions, and therefore tend to have lower weights, especially at Equatorial latitudes. The fact that Jason-1 has more weight at the coast is not necessarily due to a larger amount of available observations - as it may be justified by the inverse proportionality between variance and number of observations - but to an actual higher performance of the mission. This can be seen in figure 4.5, where the weights of Jason-1 at each node (round markers) are plotted against the distance to coast, and the color of the markers represent the number of observations. Within 200 km to the coast, the nodes with ~ 500 observations show weights larger than $10 - 15\%$, while nodes with > 700 observations can have weights lower than 10% ■.

4.3 Reconstruction of full tidal signal

Residual in-phase and quadrature components are finally restored to FES2014 full tidal signal. First of all, in-phase and quadrature components of FES2014 are derived according to equations 2.26 and 2.27. Then, both FES2014 and residual components are interpolated onto a common regular grid with resolution of 1/8 degree, which is the final grid with which EOT is released. Residual in-phase and quadrature components are restored to FES2014 using the definition of the sum of two sinusoids with same frequency (Anderson, 2006), where

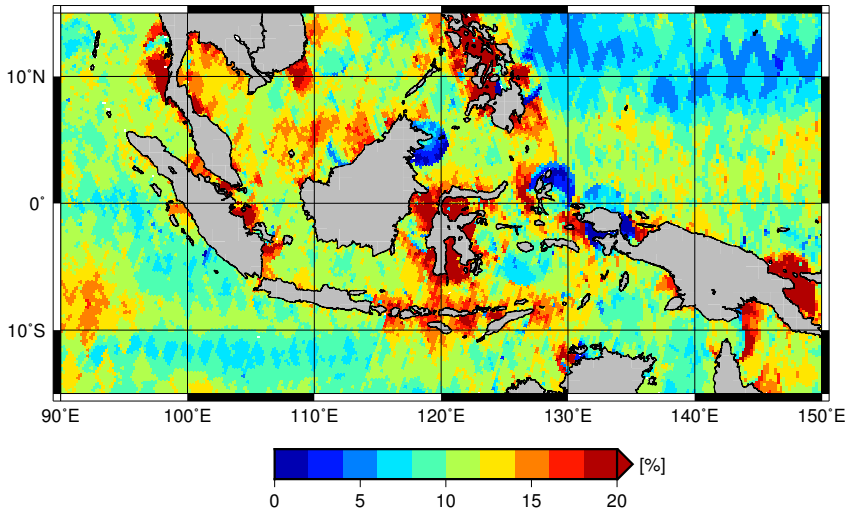

Figure 4.4: Weights of Jason-1 mission according to VCE in percentage. Credit: Piccioni et al., 2019b.

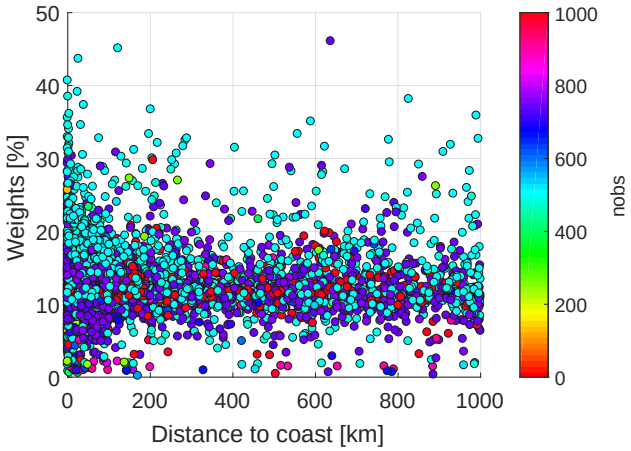

Figure 4.5: Weights in percentage for Jason-1 against distance to coast. The markers represent the nodes, and their color shows the mission's number of observations available at each node. Credit: Piccioni et al., 2019b.

the total amplitude is:

$$H_{total} = \sqrt{(H_{res}\cos g_{res} + H_{FES}\cos g_{FES})^2 + (H_{res}\sin g_{res} + H_{FES}\sin g_{FES})^2}$$

and the total phase is:

$$g_{total} = \tan^{-1}\left(\frac{H_{res}\sin g_{res} + H_{FES}\sin g_{FES}}{H_{res}\cos g_{res} + H_{FES}\cos g_{FES}}\right)$$

where subscripts res and FES represent residual and FES2014 elements respectively. H_{total} and g_{total} can be rewritten in terms of in-phase and quadrature components as:

$$H_{total} = \sqrt{(A_{res} + A_{FES})^2 + (B_{res} + B_{FES})^2}$$

and the resulting phase is:

$$g_{total} = \tan^{-1}\left(\frac{B_{res} + B_{FES}}{A_{res} + A_{FES}}\right)$$

4.4 The error of the fit

A purely statistical error is computed for the residual amplitude and phase, and it is based on the standard error of the regression and the error propagation principles. With VCE the vector of the standard deviations of elements in X, σ_x, can already be found in the diagonal of the pseudo-inverse matrix:

$$\sigma_x = diag(N_x^{-1})$$

This is the VCE version of the expressions defined in (Heij et al., 2004), in which σ_x is weighted with the standard error σ_0 of the regression. With VCE instead, the weights are already applied to the main normal equation, and so to the N_x^{-1} diagonal (Amiri-Simkooei, 2013). The standard deviation of amplitude and phase are derived following the general rule of error propagation, that says that the error of a function $f(q)$ is directly proportional to the product of the error of q and the derivative of f in q (Taylor, 1997):

$$\sigma_f(q) = \sigma_q \frac{\partial f(q)}{\partial q} \tag{4.8}$$

The standard deviation of the amplitude, σ_H of a certain constituent n, is defined as the standard deviation of equation 2.28:

$$\sigma_H = \sigma\left[\sqrt{A^2 + B^2}\right]$$

The amplitude can be written as a function of K ($f(K) = \sqrt{K}$) so that:

$$\sigma_H = \sigma\left[\sqrt{K}\right] = \sigma_K \frac{\partial\sqrt{K}}{\partial K} = \sigma_K \frac{1}{2\sqrt{K}}$$

The error σ_K is the sum in quadrature of two errors (Taylor, 1997):

$$\sigma_K = \sqrt{(\sigma\left[A^2\right])^2 + (\left[B^2\right])^2}$$

that are computed as:

$$\sigma\left[A^2\right] = \sigma_A \frac{\partial A^2}{\partial A} = \sigma_A 2A$$

$$\sigma\left[B^2\right] = \sigma_B \frac{\partial B^2}{\partial A} = \sigma_B 2B$$

where σ_A and σ_B that are two elements of the standard deviation vector σ_x, and correspond to the standard deviation of in-phase and quadrature coefficients A and B computed in X. Note that here, A and B are intended for a certain constituent n, but the subscript for A_n and B_n, and for their relative standard deviation, is avoided for simplification. So, σ_K becomes:

$$\sigma_K = \sqrt{(\sigma_A 2A)^2 + (\sigma_B 2B)^2}$$

And the standard deviation of the amplitude is:

$$\sigma_H = \frac{\sqrt{(\sigma_A 2A)^2 + (\sigma_B 2B)^2}}{2\sqrt{A^2 + B^2}}$$

The same reasoning is done to compute the standard deviation of the phase σ_g:

$$\sigma_g = \sigma\left[\tan^{-1}\frac{B}{A}\right] = \sigma\left[\tan^{-1} K\right]$$

So:

$$\sigma\left[\tan^{-1} K\right] = \sigma_K \frac{\partial \tan^{-1} K}{\partial K} = \sigma_K \frac{1}{1 + K^2}$$

and according to the definition of the error of a quotient:

$$\sigma_K = \sigma\left[\frac{B}{A}\right] = \left|\frac{B}{A}\right| \sqrt{\left(\frac{\sigma_A}{A}\right)^2 + \left(\frac{\sigma_B}{B}\right)^2}$$

That gives:

$$\sigma_g = \frac{1}{1 + \left(\frac{B}{A}\right)^2} \left|\frac{B}{A}\right| \sqrt{\left(\frac{\sigma_A}{A}\right)^2 + \left(\frac{\sigma_B}{B}\right)^2}$$

Finally, the expressions of σ_H and σ_g can be further rearranged for a better reading as:

$$\sigma_H = \sqrt{\frac{A^2\sigma_A^2 + B^2\sigma_B^2}{A^2 + B^2}} \tag{4.9}$$

$$\sigma_g = \frac{\sqrt{B^2\sigma_A^2 + A^2\sigma_B^2}}{A^2 + B^2} \tag{4.10}$$

Considerations on the error of the fit

Tide model errors find an important application in gravimetry studies. An extensive research has been carried out about the impact of tide model errors on gravity field measurements (e.g. Ray et al., 2001, Knudsen and Andersen, 2002, and Ray et al., 2003), and the ongoing TIDUS project is also focused on such issue. Tide model uncertainties are rarely released with their tide models, and their computation is not often discussed in literature. Statistical errors that are generally derived from least-square-based tide models heavily depend on

number of samples used for tidal estimates (k in this case), and are therefore not enough to obtain realistic errors intended as the precision estimation of the models. These formulae are too simplistic, and a high number of observations causes standard deviation values to be too small, and therefore with no significance in terms of precision. The other problem is that for a tide model like EOT, the error computation requires the sum of the errors of FES2014 background model with the errors of the residual tides. Unfortunately, uncertainties of FES2014 are not available globally, but only at locations where observations are assimilated. Also, the derivation of the a posteriori covariance matrix on the whole grid would demand new and substantial developments in the assimilation code, and then a supplementary assimilation process (M. Cancet, personal communication). Cancet has explained that this procedure is not planned for the moment, but she suggested to use the approach of tide model differences, which has been extensively used to derive global tide uncertainties. This method is illustrated in Andersen, 1995 and St14, and it is a sort of computation of standard deviation (SD) between models:

$$SD = \frac{1}{N}\sum_{i=1}^{N}\sqrt{\frac{1}{2}\left[\left(H_n\cos g_n - \overline{H}\cos\overline{g}\right)^2 + \left(H_n\sin g_n - \overline{H}\sin\overline{g}\right)^2\right]} \tag{4.11}$$

where H_n and g_n are the amplitude and phase of each model n, and $\overline{H}$ and $\overline{g}$ are the average amplitude and phase computed over the N models. This would give an approximation of the model uncertainties, with optimistic values in regions where models are based on the same altimetric dataset, and pessimistic values everywhere else Ray et al., 2003. This method may be problematic, for example when differences between models are due to artefacts contained in other models (see section 6.1 where along-track features appear in open ocean due to OSU12 model). Also, these differences are generally computed onto a common grid with coarser resolution and therefore the error map may not have same resolution as the model. Moreover, the models involved may not provide the same number of constituents, reducing the available amount of error estimates.

Another suggestion comes from R. Ray, and it is similar to what Pugh and Woodworth, 2014a illustrate. Uncertainties are considered as a sort of signal-to-noise ratio of the tidal constituent of interest, with respect to its tidal band. In the frequency domain, the tide of interest and its neighbour frequencies are selected. The variance density of the background noise of the tidal band selected, S^2 defines the standard error of the amplitude and phase:

$$\sigma_H = \frac{S}{\sqrt{2}}$$

$$\sigma_g = \frac{S}{H\sqrt{2}}$$

S^2 depends on the width of the tidal band considered $\Delta\omega$, the timeseries length T, and the variance of the noise of the tidal band $S^2_{\Delta\omega}$:

$$S^2 = \frac{S^2_{\Delta\omega}}{T\Delta\omega}$$

It must be said that this approach is generally applied to tide gauge data, from which it is easier to distinguish between tidal signal and noise than altimetry data. However, it would be worth to test a similar approach for empirical tide models.

4.5 Additional studies

Improvements of tidal estimates in coastal areas are the main focus of this work. Different algorithms and datasets were tested, in order to achieve the wanted results. In this section, the author has collected few examples of failed attempts and an in-between exercise that have been carried out through these years. The *failed attempts* are alternative cap size choices; the *in-between exercise* is a test of EOT algorithm applied along track, that demonstrates that the use of a coast-dedicated altimetric product, i.e. ALES retracker, improves tidal estimates at the coast. This experiment is crucial, in the sense that, it justifies the further use of coastal altimetric products for EOT. In this section, the theory behind these studies is shortly summarized. In chapter 6 few results are also discussed for completeness.

4.5.1 The cap size choice: innovative failures

The first tests for EOT grids were done on a fixed cap size of 330 km. Before reaching the empirical conclusion that a latitude-dependent cap size was the best solution found so far, other approaches have been implemented - and later discarded - in favour of algorithms with better computation and error performance. In this section, two solutions are summarized: the variable cap size according to ocean depth, and the coastal cap with selective mask.

Variable cap size according to ocean depth

The idea behind an alternative cap size is based on the fact that tides in shallow and coastal waters are affected by more local regimes, that can't be described by tide models because of their too-coarse resolution. Moreover, it has been observed that the standard error σ_0 [1] of the least squares algorithm is highly correlated with bathymetry. In figure 4.6 the geographical distribution of σ_0 can be visually compared with the bathymetry in the North Sea[2] area, while in figure 4.7, σ_0 is plotted against the depth. Below 400 m depth, σ_0 increases fast, reaching values above 10 cm.

As already mentioned, the increase of σ_0 is also justified by its strict dependency on the number of observations, which become sparser at coastal areas (e.g. figure 4.8). One hypothesis for a better description of the tidal local behaviour was to reduce the cap size of

[1] σ_0 for VCE is defined as: $\sigma_0 = \left(\frac{\sum_{m=1}^{M} \varepsilon_m' W_m \varepsilon_m}{\sum_{m=1}^{M} k_m - j} \right)^{\frac{1}{2}}$

[2] In this thesis the North Sea is intended as the area surrounding the United Kingdom and Ireland, which includes the western part of the North Sea and the northern part of the North West European Shelf.

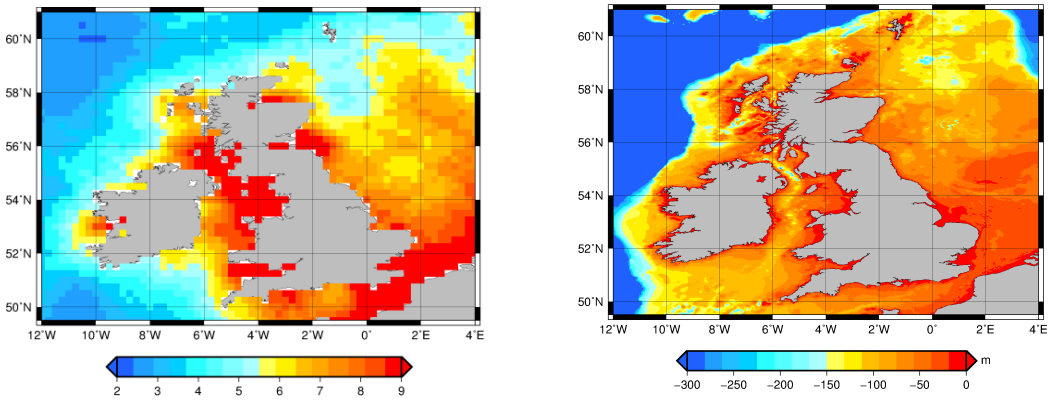

(a) (b)

Figure 4.6: Visual comparison between the internal error σ_0 (in cm) of the weighted least squares (a) and the bathymetry map of the North Sea (b).

each node according to a linear depth-dependence. Among all the solutions tested, the best was:

$$\psi_{max} = 100 + 0.575Z \tag{4.12}$$

where Z is the ocean depth. The choice of the numbers are the result of a compromise between the cap-size reduction and the collection of enough number of observations that could allow constituent resolution. From figure 4.9, it can be observed that a variable cap size do not affect the values of σ_0 at shallow depths despite the lower number of observations involved at each node. Some accuracy tests were also run, showing a lower performance with respect to a fixed cap-size choice (chapter 6).

Cap with selective mask

Large cap sizes close to land may include different tidal regimes that belong to coasts oriented in different directions. For example, over the extremes of peninsulas, or around large islands. Therefore, also in this case the idea was to isolate a more local behaviour of tides, using a sort of directional mask, that includes only observations that are not separated from the node with land. In figure 4.10 the concept of selective masks is illustrated. The algorithm first finds the nearest land point to the node within a search radius of 330 km (a). All observations found within this minimum distance are all accepted. The remaining observations undergo a selection process, that checks whether along a straight line between the node and each observation there is a land point (b). If yes, the observation is discarded. In figure 4.11 two examples of selective masks are shown for Jason-series tracks. The yellow asterisk represents the grid node of interest, the white dots mark the location of CTOH track observations, and the red markers represent the observations accepted within the mask. It is easy to see that all observations "not seen" by the node because "behind" land are discarded.

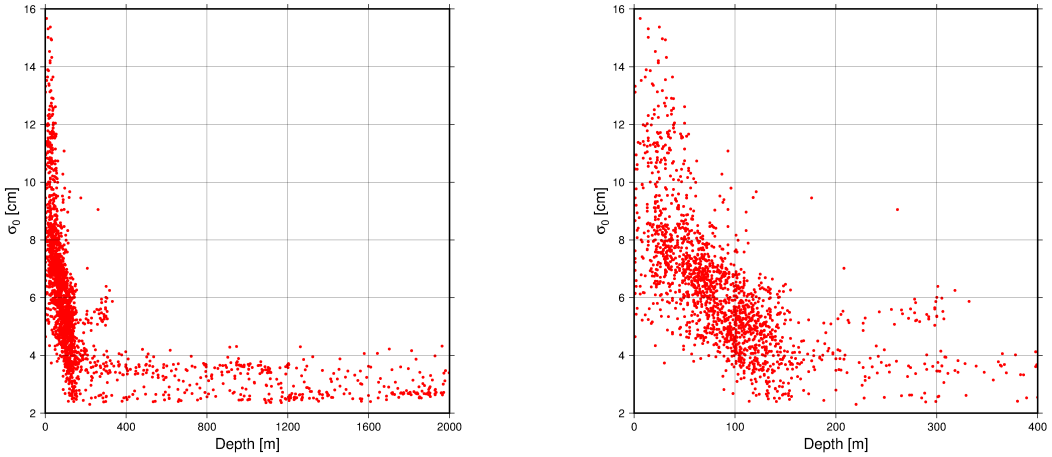

(a) (b)

Figure 4.7: The internal error σ_0 plotted against ocean depth (a), with zoom on depths below 400 m (b).

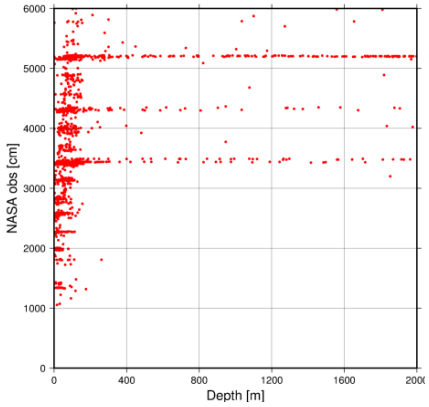

Figure 4.8: Number of observations of Jason-series missions plotted against depth in the North Sea.

4.5.2 Focus on the coast: the along-track test

The choice of altimetry products plays a crucial role in sea level determination at the coast, with consequent impacts on coastal tide estimation. The purpose of this test is to assess the influence of a tailored coastal retracking method on the quality of an ocean tide model. ● In other words, we want to quantify the difference at the coast between tidal constituents estimated with a dedicated coastal retracker and the same constituents derived with an ordinary open ocean retracker (based on the MLE4 algorithm which adopts the Brown-Hayne functional form, Brown, 1977, Hayne, 1980). The coastal retracker used for this experiment is ALES retracker (Passaro et al., 2014). For such aim, an along-track solution was preferred compared to the classical grids, in order to study the evolution of the performances and the impact of the retrackers with respect to the distance to the coast. The method used to

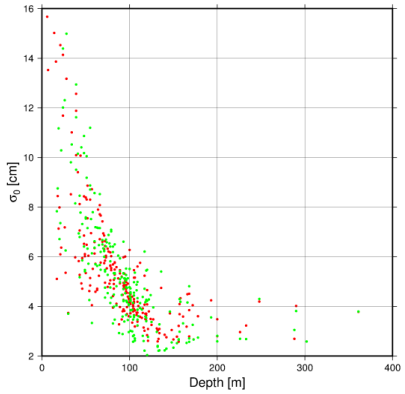

Figure 4.9: Comparison between σ_0 values obtained with fixed cap size (in red) and the ones computed with depth-dependent cap size (green).

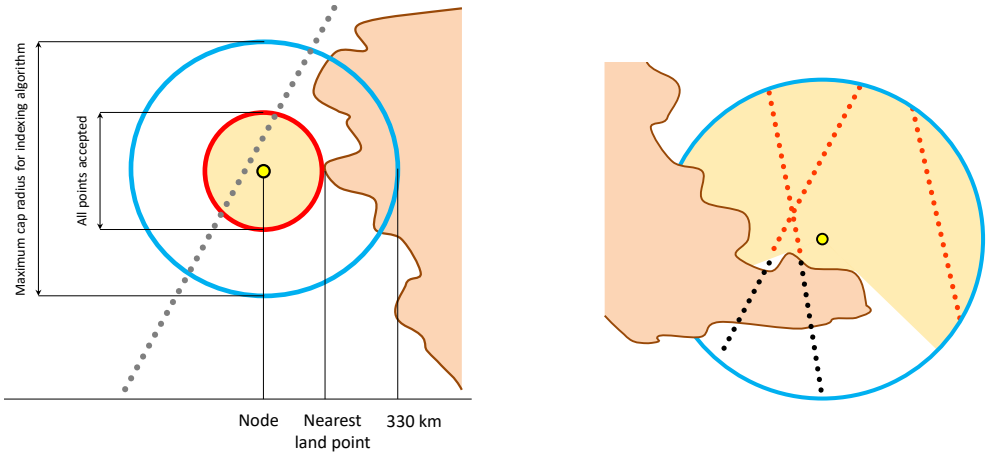

(a) (b)

Figure 4.10: Schemes of the algorithm (a) and wanted result (b) of selective mask. In (b) the yellow shaded area represent the mask within all observations are accepted for that node. Accepted observations are in red and discarded observations in black.

compute the tidal constants is based on the EOT model, however, the nodes are selected along Jason-1 and Jason-2 tracks, and correspond to the 1 Hz points of CTOH nominal tracks. Each node represents the center of the circular cap. In this case, ψ_{max} measures 15 km. Within ψ_{max} 20 Hz observations are used (version SGDR-E for Jason-1 and SGDR-D for Jason-2). High-rate data allow a ground spatial resolution of circa 350 m along-track, which is preferred over 1 Hz products for this dedicated investigation along-track and at coastal areas. SLA values are flagged with the following criteria:

- -2.5 m $\leq$ SLA $\leq$ 2.5 m ((Savcenko and Bosch, 2012))
- SWH $<$ 11 m ((Picot et al., 2012))
- 7 dB $<$ BS $<$ 30 dB ((Picot et al., 2012))

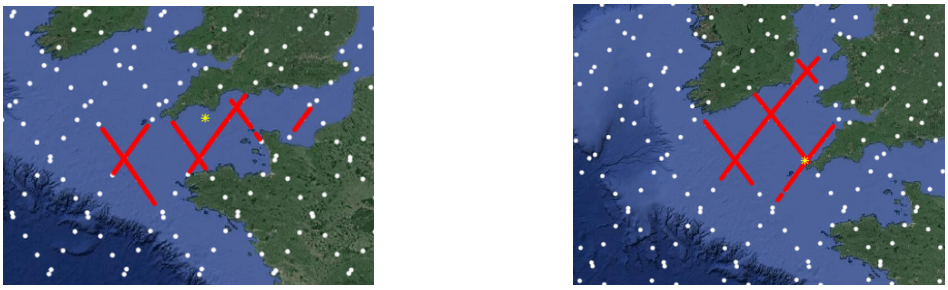

(a) (b)

Figure 4.11: Results of selective cap in the North Sea. The yellow star is the node. The white markers represent observations along Jason nominal tracks and the red markers are the observations included in the selective mask.

- Distance to coast > 3 km

where SWH is the Significant Wave Height and BS is the backscatter coefficient. Note that the backscatter coefficient is commonly defined in literature as σ_0, however in this case BS is used to avoid ambiguities with the standard error of the least-squares algorithm. The harmonic constants resulting from the along-track model are compared against in situ data, selected according to the following criteria:

- Maximum distance to satellite track: 50 km
- Tide gauge data already assimilated in FES2014 model (Cancet, personal communication) are discarded
- Stations near estuaries are discarded. Exceptions for fjords (e.g., Finnish and Canadian coasts)
- Final manual screening on the selected stations: tide gauges with timeseries shorter than one year are discarded while part of the timeseries containing doubtful offsets are not considered

For each site, one or two crossing tracks were found, obtaining a total of 85 tracks for 70 tide gauges. In chapter 6 results of this experiment are summarized ●. More details can be found in Piccioni et al., 2018.

Chapter 5

Validation: data and methods

Data and statistical methods used to validate and compare EOT with other tide models are illustrated in this chapter. The validation approaches used for tide models follow the standard procedures that can be found in literature (e.g. St14, Ray, 2013, Cheng and Andersen, 2011, etc.), and are summarized in section 5.1. In section 5.2 the in situ validation dataset created ad hoc for tide model validation is described, and the validation of the dataset itself is also discussed.

5.1 Evaluation methods

The performance of tide models is usually assessed through comparison with harmonic constants of in situ data. The statistical quantities found in literature are mainly two. For each constituent n, one can compute:

- the Root Mean Square (RMS) error, which compares the in-phase and quadrature coefficients of one model (A_{mod}, B_{mod}) and one tide gauge station p (A_p, B_p) for a constituent n:

$$RMS_{n,p} = \sqrt{(A_{mod} - A_p)^2 + (B_{mod} - B_p)^2} \tag{5.1}$$

  that becomes, when averaged for all P in situ stations considered:

$$RMS_n = \sqrt{\frac{\sum_{p=1}^{P} RMS_{n,p}^2}{2P^2}} \tag{5.2}$$

- the Median Absolute Differences (MAD), which are less sensitive to outliers and can be useful at coastal areas, where poor model performance at few stations may affect the entire result (St14). In this work, geometric MAD are used, which follow the formula:

$$MAD_n = \sqrt{< |A_{mod} - A_p| >^2 + < |B_{mod} - B_p| >^2} \tag{5.3}$$

  where the symbol $< x >$ represents the median value of quantity x over all in situ stations and $|x|$ the absolute value of x.

For an overall performance, the Root Sum Square (RSS) error of the available n constituents is also calculated:

$$RSS = \sqrt{\sum_{k=1}^{n} {E_n}^2} \tag{5.4}$$

where E_n can be RMS_n or MAD_n values.

In addition, for pairwise differences between models (identified as $mod1$ and $mod2$), the relative RMS is calculated as:

$$\Delta RMS_n[\%] = \frac{\Delta RMS_n}{RMS_{n,mod1}} \cdot 100 \tag{5.5}$$

where $\Delta RMS_n = RMS_{n,mod1} - RMS_{n,mod2}$. $\Delta RMS_n[\%]$ is used to quantify the improvement of one model relative to another - in this case, of $mod2$ relative to $mod1$; if $\Delta RMS_n[\%]$ is positive, it means that the RMS error of $mod2$ is smaller, thus shows an improvement with respect to $mod1$.

Finally, the tidal elevation differences (equation 4.11) are used to derive the global error of the models, as already discussed in section 4.4.

5.2 Construction of a validation dataset

It is a standard practice to derive tide model accuracy from comparisons with in situ data such as tide gauges or bottom pressure gauges. For this reason, it is essential to have a reliable, validated, and extensive dataset, and possibly easy to use. For this reason, an up-to-date validation dataset with documented sources has been created (Piccioni et al., 2019a). Part of the dataset was computed with an in-house algorithm starting from an existing tide gauge project (see section 5.2.1). The dataset has been then integrated using data from other sources, which are shortly described in section 5.2.3.

5.2.1 TICON

▲ The TIdal CONstants (TICON) dataset was created at DGFI-TUM using tide gauges of the Global Extreme Sea Level Analysis (GESLA) project. It contains information on 40 harmonic constants computed from 1145 sites. The latest version of GESLA (GESLA-2) contains 1355 harmonized records, collected among 30 different sources, such as national authorities, research institutions, and international projects. An exhaustive description of the different datasets involved, together with the corresponding source reference, can be found in (Woodworth et al., 2017). 1276 of these records are publicly available and were used to build the TICON dataset. The remaining 77 "private"records were not used, as the intention of TICON authors was to guarantee a free and public access to the data. GESLA public stations have a quasi-global extent, with a higher data coverage in the Northern Hemisphere, in particular: North America, Europe and Japan. A preliminary screening was performed

on all records to analyze the average duration of the measurements and the distribution of the temporal gaps. It was observed that the records span from a minimum of 150 days, to a maximum of 168.6 years, with a median length of 22.2 years, and distribution shown in figure 5.1. The TICON algorithm developed at DGFI-TUM computes tidal constants for all the records. At first, the program exploits information on GESLA data quality to remove single corrupted observations. GESLA flags characterize the quality and the possible usage of the individual measurements. Only measurements assigned as "correct" or "interpolated value" were selected as valid. In addition, data gaps due to missing physical observations can occur. After flagging, 417 records have missing data less than 2% of the total number of observations, 624 records contain missing data between 2% and 25%, 170 records between 25% and 50%, and only 65 records have gaps above 50% (figure 5.2). Because of the different nature of these temporal gaps, their lengths may also vary, ranging between a few samples (in general some hours) and years. The algorithm performs a first selection of records

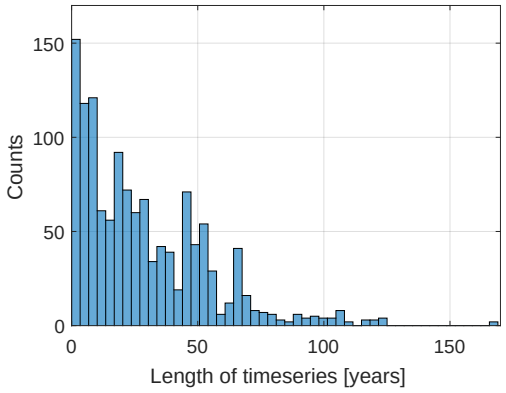

Figure 5.1: Overview of the length (in years) of the GESLA time series

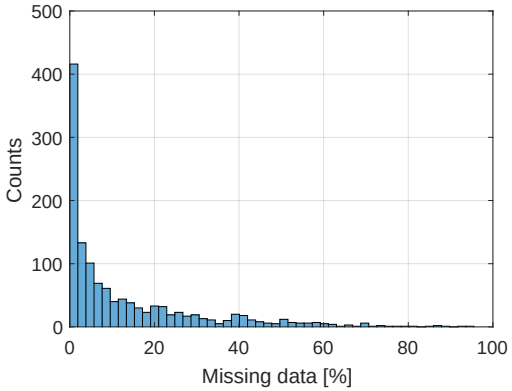

Figure 5.2: Overview of missing data in GESLA records

suitable for least-squares harmonic analysis, that is: the period of the observations of each record must be larger than one year. The choice of this minimum duration is based on the Rayleigh criterion for tidal constituent separation (Pugh and Woodworth, 2014a). The time

series length is measured after rejecting individual observations for unsuitable flags. This is done because temporal gaps due to flagging may occur at time series extremes, shortening their extent. In figure 5.3 a comparison of the length of time series before and after flagging rejection is shown. 513 files show no difference after flagging, 625 are reduced up to one year and 138 records are shorter by more than one year. Two extreme cases occur for the Canadian stations of Port Hardy and New Westminster, whose time series, despite a reduction of 10 and 19 years after flagging, are still respectively 50.7 and 45.7 years long. 44 records - which correspond to 3.45% of the public GESLA dataset - do not reach the minimum time span required and are discarded from the tidal analysis and the final dataset. A second selection is made in relation to the amount of missing data within each record. The distribution of missing data for time series longer than one year is shown in figure 5.4. After removing flagged values at record extremes, the amount of missing data for more than 500 records is below 3%. In the scatter plot of figure 5.5 the percentage of missing data is plotted against the time series length. The maximum length of temporal gaps is represented by the marker color. In general, records below 50 years duration do not show large gaps, and in the majority of cases missing data are below 30%. Few long records are characterized by extensive temporal gaps that exceed 20 years, that may cause a loss of data larger than 40%. The authors wanted to select the full original records with the longest time series possible. For this reason, a threshold of 70% of valid observations was set, above which the records are processed for their full length. This criterion is used to compute tidal harmonics for the full time series, reducing the risk of processing records with highly scattered observations.(A similar method was used by Ruiz Etcheverry et al., 2015 to sort and compare the annual and semi-annual signal of tide gauge observations against satellite data). In total, 1145 records were processed with this condition, while 87 were excluded from the dataset. The overall number of discarded records (due to short time series or missing observations) is 131, that corresponds to 10.3% of the full GESLA dataset. In figure 5.6 the geographical distribution of TICON data is shown. It was chosen to compute harmonic constants for 40 tidal con-

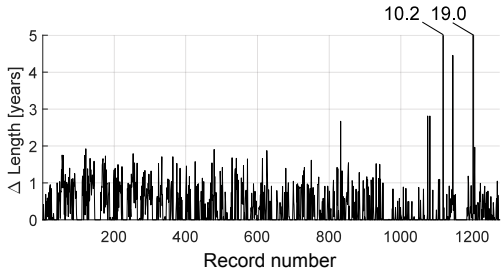

Figure 5.3: Difference of timeseries length before and after flagging rejection. The record numbers on the x-axis are sorted according to the length of the original timeseries, from the shortest to the longest.

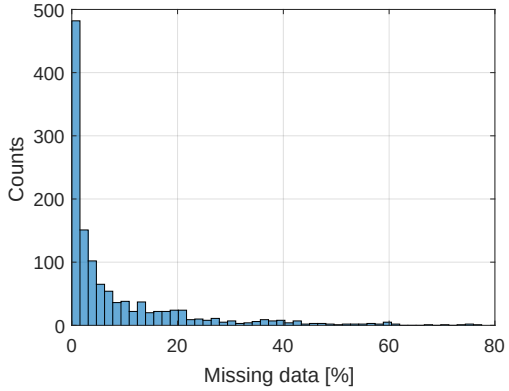

Figure 5.4: Overview of missing data in GESLA records after removing the flagged data.

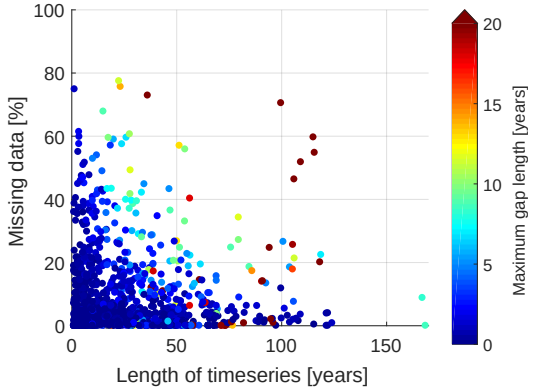

Figure 5.5: Percentage of missing data plotted against the time series length. The maximum gap length is color-coded. The plot shows the records after the removal of flagged data at each end of their time series.

stituents because this dataset was made to evaluate ocean tide models. Generally, modern tide models include no more than 15 tidal constituents; however, there are exceptions such as FES2014 model, that provides 34 constituents Carrère et al., 2015). Thus, providing the 40 most important constituents should be sufficient for an adequate model evaluation. The harmonic constants were derived using the least-squares approach, which is often preferred over the spectral analysis because it allows to perform tidal estimation on incomplete time series (Ponchaut et al., 2001). A matrix system, and the fitting error computation, was set up according to equations illustrated in chapter 4. It is important to say that the error of the fit calculated in TICON is related to the number of observations analyzed (because of the degrees of freedom in the standard error of the regression), and therefore for long time series too small errors are computed. Considerations of section 4.4 are also valid in this case.

Finally, the results are merged and saved in a user-friendly text file, together with supplementary information relevant to the tide gauge station and the time series. TICON

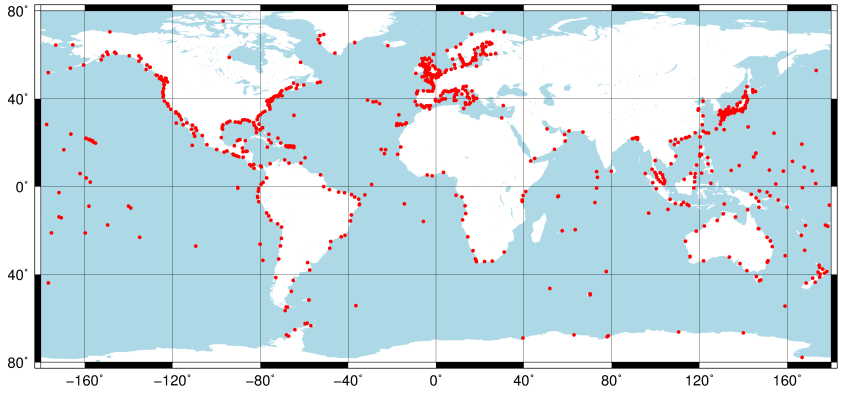

Figure 5.6: Geographical distribution of TICON data.

algorithm is fully described in Piccioni et al., 2019a and the dataset is stored in the PANGAEA public repository as a text/ASCII format, and it is freely available for any research purpose (PANGAEA identifier: *https://doi.pangaea.de/10.1594/PANGAEA.896587*). The dataset is a single file that contains the harmonic constants of 40 tidal constituents and their related errors. An example of part of the TICON file is shown in table 5.1 for the station of Port Angeles, Washington, USA. The file has a tab-separated column structure and the columns display information on: left to right you have latitude and longitude (with domain 0 to 360) of the station's location, constituent's name, amplitude of the tidal constituent in cm, phase lag (Greenwich lag) of the tidal constituent in degrees, percentage of missing data within the time series analyzed, number of observations used for the least-squares estimation, length in days of the largest gap found in the record, date of the first and the last observation, and a code that corresponds to the source of the record. The constituents are sorted in ascending order, according to their frequency ▲.

Lat	Lon	Constituent	Amplitude	Phase Lag	σ_{am}	σ_{ph}	Missing	Observations	Maximum	First	Last	Record
[deg]	[deg]	Symbol	[cm]	[deg]	[cm]	[°]	Data [%]	Analyzed	Gap [days]	Observation	Observation	Source
48.1250	236.5600	SA	10.612	3.834	0.003	0.001	28.01	210913	3408.25	01/08/1979	31/12/2012	gesla.uhslc
48.1250	236.5600	SSA	1.896	220.888	0.001	0.004	28.01	210913	3408.25	01/08/1979	31/12/2012	gesla.uhslc
48.1250	236.5600	MM	2.024	197.866	0.001	0.004	28.01	210913	3408.25	01/08/1979	31/12/2012	gesla.uhslc
48.1250	236.5600	MSF	0.596	216.913	0.000	0.013	28.01	210913	3408.25	01/08/1979	31/12/2012	gesla.uhslc
48.1250	236.5600	MF	1.298	164.147	0.000	0.005	28.01	210913	3408.25	01/08/1979	31/12/2012	gesla.uhslc
48.1250	236.5600	MTM	0.460	183.835	0.000	0.017	28.01	210913	3408.25	01/08/1979	31/12/2012	gesla.uhslc
48.1250	236.5600	MSQ	0.128	180.800	0.000	0.062	28.01	210913	3408.25	01/08/1979	31/12/2012	gesla.uhslc
48.1250	236.5600	2Q1	0.804	231.874	0.000	0.009	28.01	210913	3408.25	01/08/1979	31/12/2012	gesla.uhslc
48.1250	236.5600	Q1	6.649	232.570	0.002	0.001	28.01	210913	3408.25	01/08/1979	31/12/2012	gesla.uhslc
48.1250	236.5600	O1	38.670	241.412	0.010	0.000	28.01	210913	3408.25	01/08/1979	31/12/2012	gesla.uhslc
48.1250	236.5600	M1	2.145	347.220	0.000	0.001	28.01	210913	3408.25	01/08/1979	31/12/2012	gesla.uhslc
48.1250	236.5600	P1	20.848	259.529	0.006	0.000	28.01	210913	3408.25	01/08/1979	31/12/2012	gesla.uhslc
48.1250	236.5600	S1	2.062	33.524	0.001	0.004	28.01	210913	3408.25	01/08/1979	31/12/2012	gesla.uhslc
48.1250	236.5600	K1	66.796	261.405	0.018	0.000	28.01	210913	3408.25	01/08/1979	31/12/2012	gesla.uhslc
48.1250	236.5600	J1	3.402	284.364	0.001	0.002	28.01	210913	3408.25	01/08/1979	31/12/2012	gesla.uhslc
48.1250	236.5600	OO1	2.499	304.029	0.001	0.002	28.01	210913	3408.25	01/08/1979	31/12/2012	gesla.uhslc
48.1250	236.5600	EP2	0.665	200.423	0.000	0.012	28.01	210913	3408.25	01/08/1979	31/12/2012	gesla.uhslc
48.1250	236.5600	2N2	1.462	248.399	0.000	0.005	28.01	210913	3408.25	01/08/1979	31/12/2012	gesla.uhslc
48.1250	236.5600	MI2	2.754	233.646	0.001	0.003	28.01	210913	3408.25	01/08/1979	31/12/2012	gesla.uhslc

Lat	Lon	Constituent	Amplitude	Phase Lag	σ_{am}	σ_{ph}	Missing	Observations	Maximum	First	Last	Record
[deg]	[deg]	Symbol	[cm]	[deg]	[cm]	[°]	Data [%]	Analyzed	Gap [days]	Observation	Observation	Source
48.1250	236.5600	N2	11.756	280.099	0.003	0.001	28.01	210913	3408.25	01/08/1979	31/12/2012	gesla.uhslc
48.1250	236.5600	NI2	2.100	287.739	0.001	0.004	28.01	210913	3408.25	01/08/1979	31/12/2012	gesla.uhslc
48.1250	236.5600	MA2	1.101	145.594	0.000	0.007	28.01	210913	3408.25	01/08/1979	31/12/2012	gesla.uhslc
48.1250	236.5600	M2	51.586	307.293	0.014	0.000	28.01	210913	3408.25	01/08/1979	31/12/2012	gesla.uhslc
48.1250	236.5600	MB2	0.823	57.938	0.000	0.010	28.01	210913	3408.25	01/08/1979	31/12/2012	gesla.uhslc
48.1250	236.5600	MKS	0.324	169.525	0.000	0.022	28.01	210913	3408.25	01/08/1979	31/12/2012	gesla.uhslc
48.1250	236.5600	LM2	0.616	54.276	0.000	0.013	28.01	210913	3408.25	01/08/1979	31/12/2012	gesla.uhslc
48.1250	236.5600	L2	1.124	29.774	0.000	0.007	28.01	210913	3408.25	01/08/1979	31/12/2012	gesla.uhslc
48.1250	236.5600	T2	0.814	335.278	0.000	0.010	28.01	210913	3408.25	01/08/1979	31/12/2012	gesla.uhslc
48.1250	236.5600	S2	14.611	326.503	0.004	0.001	28.01	210913	3408.25	01/08/1979	31/12/2012	gesla.uhslc
48.1250	236.5600	R2	0.275	327.092	0.000	0.029	28.01	210913	3408.25	01/08/1979	31/12/2012	gesla.uhslc
48.1250	236.5600	K2	2.843	333.255	0.001	0.003	28.01	210913	3408.25	01/08/1979	31/12/2012	gesla.uhslc
48.1250	236.5600	M3	0.138	341.120	0.000	0.058	28.01	210913	3408.25	01/08/1979	31/12/2012	gesla.uhslc
48.1250	236.5600	S3	0.043	108.247	0.000	0.185	28.01	210913	3408.25	01/08/1979	31/12/2012	gesla.uhslc
48.1250	236.5600	N4	0.156	28.526	0.000	0.051	28.01	210913	3408.25	01/08/1979	31/12/2012	gesla.uhslc
48.1250	236.5600	MN4	0.711	63.974	0.000	0.011	28.01	210913	3408.25	01/08/1979	31/12/2012	gesla.uhslc
48.1250	236.5600	M4	1.463	96.914	0.000	0.005	28.01	210913	3408.25	01/08/1979	31/12/2012	gesla.uhslc
48.1250	236.5600	MS4	0.858	112.900	0.000	0.009	28.01	210913	3408.25	01/08/1979	31/12/2012	gesla.uhslc

48.1250	236.5600	S4	0.197	114.431	0.000	0.040	28.01	210913	3408.25	01/08/1979	31/12/2012	gesla.uhslc
48.1250	236.5600	M6	1.510	198.201	0.000	0.005	28.01	210913	3408.25	01/08/1979	31/12/2012	gesla.uhslc
48.1250	236.5600	M8	0.026	153.469	0.000	0.300	28.01	210913	3408.25	01/08/1979	31/12/2012	gesla.uhslc

Table 5.1: Part of the TICON dataset for the station of Port Angeles, Washington, USA. EP2, MI2, NI2, and LM2 correspond to constituents ε_2, μ_2, ν_2, and λ_2 respectively.

5.2.2 TICON validation

While tide models are validated through comparison with in-situ data, in-situ data are validated with tide models (Woodworth, personal communication). n order to validate the TICON tidal constants, a comparison with FES2014 was performed. Additional comparisons are shown between two or more "duplicate" records, i.e. records at the same location coming from different GESLA-2 sources, but are not shown in this thesis. The results are described in detail in Piccioni et al., 2019a. The validation exercise followed the methods used in St14 to compare modern tide models and tide gauge data in terms of RMS and RSS differences. Not all TICON tide gauges were used for this validation: tide gauges assimilated in FES2014 were discarded, in order to have an independent comparison; in total 923 tide gauges were used. FES2014 was chosen because it is the model with highest performances over complex areas. However, it is expected to see larger differences between FES2014 and TICON close to large rivers (e.g. Amazon River, Bay of Bengal), shelf seas (e.g. North Sea, Argentinian Shelf), and areas with complex bathymetry and/or geometry of the coast (e.g. Indonesian Sea). Figure 5.7 shows the geographical distribution of the RSS computed for the main tidal constituents (M2, S2, N2, K2, K1, P1, O1, and Q1). For the same locations shown in figure 1, computed the averaged RMS and RSS differences (table 3). These numbers are relatively small, if compared to the coastal tide gauges in St14. This may be due to the fact that TICON and FES2014 averaged differences are computed also for tide gauges in open ocean, where stronger agreement between the two is expected. Also, in areas with low tidal amplitudes such as the Baltic Sea and the Mediterranean Sea we expect smaller RMS differences. These areas are densely populated by tide gauges, and this may overweight the statistics, lowering the RMS differences. Because of the possibility of such overweight, we also performed regional comparisons. Figures 5.8 and 5.9 show areas (coasts of North Sea, and Indonesian region, respectively) where TICON and FES2014 constants show higher disagreement. In particular, in the North Sea, large RSS are found in narrow areas, such as the English Channel, in front of Northern Ireland, and inlets with river estuaries, like the Bristol Channel, and the Humber estuary. The plots are coupled with tables 5.3a 5.3b showing the regional average RMS and RSS, and the magnitude of the signal (St14) of each constituent. Constituents M2 and S2 have large tidal signals that bring also the largest differences between tide gauge and model results, with RMS of 11.72 and 5.37 cm in the North Sea, and 2.39 and 1.51 cm in the Malay Archipelago respectively.

5.2.3 The complete DGFI-TUM in situ dataset

TICON data are only at the coast. In order to ensure the best in situ data coverage possible, TICON was integrated with other datasets, with stations located at deep, shelf and coastal waters. A deep-ocean dataset was kindly provided by R. Ray, and contains harmonic

	Differences	Signal
M2	2.19	59.24
N2	1.04	11.72
S2	1.33	20.63
K2	0.73	5.85
K1	0.98	13.01
O1	0.84	9.39
P1	0.59	4.07
Q1	0.42	1.95
RSS	3.22	

Table 5.2: RMS and RSS differences between TICON and FES2014 averaged on 923 tide gauges. Values in cm.

(a)	Differences	Signal
M2	11.72	151.76
N2	2.63	28.43
S2	5.37	52.39
K2	1.54	15.06
K1	0.63	6.84
O1	0.56	6.44
P1	0.49	2.29
Q1	0.26	2.16
RSS	13.29	

(b)	Differences	Signal
M2	2.39	37.36
N2	0.64	7.20
S2	1.51	18.56
K2	0.49	5.31
K1	0.99	19.28
O1	1.09	13.85
P1	0.44	6.11
Q1	0.22	2.75
RSS	3.33	

Table 5.3: RMS and RSS differences between TICON and FES2014 averaged for tide gauges in the North Sea (a) and Malay Archipelago (b). Values in cm.

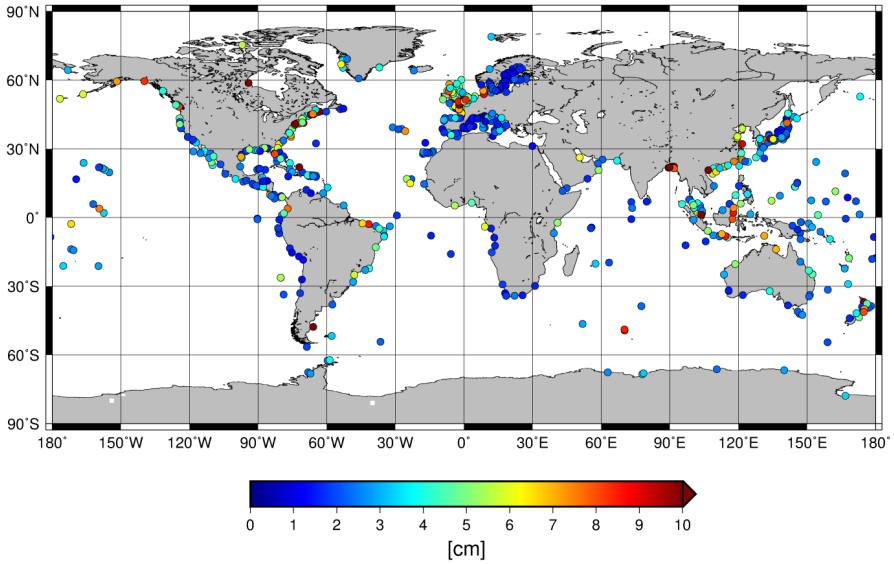

Figure 5.7: Geographical distribution of RSS differences between TICON and FES2014 for 923 tide gauges.

constants of 151 bottom-pressure gauges. In Ray, 2013, a detailed dataset description, with validation tests and comparison with former data is found. Shelf-water gauge data were also provided by R. Ray, and consist of harmonic constants of 195 stations located at waters shallower than 200 m (coastline excluded). Both deep-ocean and shelf-water datasets were used in St14. Finally, the World Ocean Circulation Experiment (WOCE) sea level observation network is also included. This dataset contains 177 stations located at the coast and on islands (Ponchaut et al., 2001). WOCE is already part of the GESLA (thus, TICON) dataset. However, the WOCE harmonic constants available at DGFI-TUM are the ones used in St14, and were added to the final dataset for completeness. All data are merged into a file with same format as TICON (table 5.1).

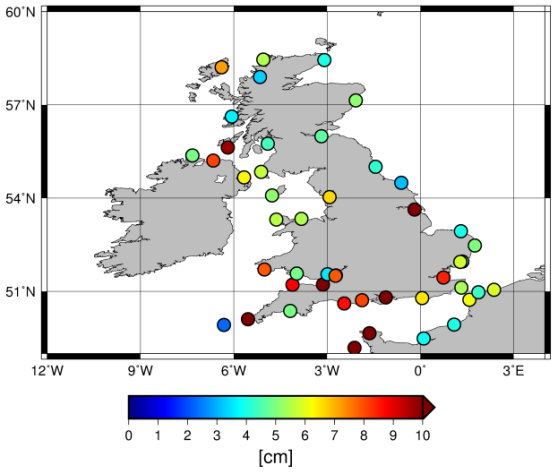

Figure 5.8: RSS differences between TICON and FES2014 for tide gauges located in the North Sea.

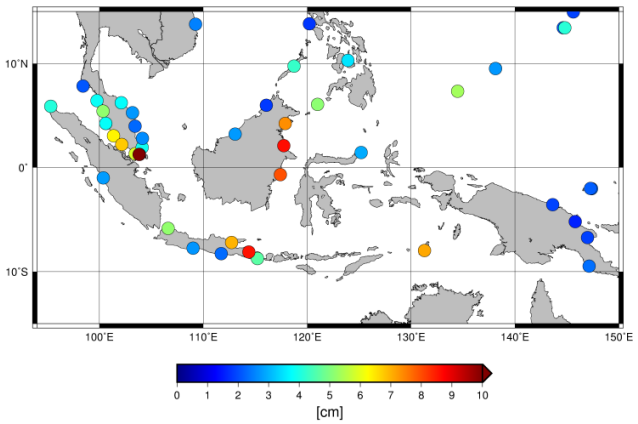

Figure 5.9: RSS differences between TICON and FES2014 for tide gauges located in the Malay Archipelago.

Chapter 6

Results and discussion

During the last decades, improvements in oceanographic models and observation techniques brought remarkable results in tide models. In open ocean their accuracy has reached values below 1 cm, while larger errors are still found in shallow waters ($\sim$ 5 cm in shelf seas and $>$ 6.5 cm at coastal areas, St14), where tidal constituents are highly dependent on bathymetry and the shape of the oceanic shelf (Andersen, 1999). Such errors can be detected also from the analysis of SD between models (cf. equation 4.11), that shows high discrepancies in these areas (St14). With new tide models available after St14, the SD exercise has been reproduced (section 6.1) and similar disagreement was found in the same regions, in particular: at high latitudes, shelf seas, semi-enclosed seas, and coasts with complex geometries. In order to assess the performance of EOT19p, two among these critical areas, individuated through the analysis of the global SD, were selected: the Malay Archipelago and the North Sea. In section 6.2, EOT19p is compared regionally with its previous version and other tide models. Results of additional studies presented in 4.5 are shown in section 6.3.

6.1 Comparison of global models

A first analysis was made on semi-empirical and assimilative tide models. With SD maps we have an overview of the spatial discrepancies of the tidal grids on a global scale. The global models included in this comparison are FES2014, EOT11a, TPXO8, DTU16 ,OSU12v1.1 (henceforth OSU12), HAMTIDE11a, GOT4.8. Note that the purely hydrodynamic models were not included in this comparison, because they are known to be less accurate than data-constrained models. An example with these models will be shown later for completeness. Figure 6.1 shows the results obtained for the major constituents N2, M2, S2, K2, Q1, O1, P1, and K1. The SD appears higher than the one shown in St14, and it is especially visible in open ocean, where the models are supposed to agree best. These higher values have patterns due to altimetry tracks, which is a feature mainly contained in model OSU12. In

figure 6.2 the SD is shown without OSU12 model for constituents M2 and K1: there is a clear improvement in open ocean areas, in particular for constituent K1. These issues in OSU12 may be related to the aforementioned errors found in the prior models, and the need of updating altimetric data. However, track residuals are still visible for constituent M2 only, and they can be attributed to DTU16 model (see figure 6.3 that shows SD without OSU12 and DTU16). This feature may be due to the fact that the harmonic constants in DTU16 are computed for bins along-track, and interpolated on a grid in a second moment. In open ocean, residual current signals are still observed. In table 6.1 the total SD between models is shown for results containing OSU12 (second column), and the ones without OSU12 (third column), for all constituents analyzed. An SD larger than 8 cm is found when OSU12 is used. This indicates that the model's disagreement is not only in open ocean, where the maximum SD observed is of ~ 0.5 cm, but also at coastal areas, where heavy differences with other models can give such high total values. SD values without DTU16 are not displayed, as they are similar to the ones without OSU12. Results without OSU12 show SD lower than the cm, and an RSS of 1.14, against the one obtained in St14 of 2.46 cm; these improved agreements may be justified by the presence of FES2014 and DTU16, instead of their previous versions (FES2012 and DTU10) used in St14, which have similar behavior at coastal areas.

The purely hydrodynamic models are known to be less accurate than semi-empirical or assimilative models (St14), as they are based solely on the mathematical description of ocean phenomena, and are not constrained by altimetry or in situ observations. Also, the level of agreement between models of the same type is much lower than the one shown for the previous models. In figure 6.4, the SD of STORMTIDE, HIM, and HYCOM model is shown for constituent M2. The SD range in this case goes from 0 to 18 cm, with values up to 4 cm in the open ocean. In addition, high differences, of 9 to 12 cm are not only observed at shelf areas (e.g. in Patagonia or West New Zealand), but also in regions where e.g. large river inflow occur (like in the Amazonian delta). The weighted average of the SD for these models is 13.03 cm, which is not comparable to the one obtained with constrained models. (Note that for HD models the common latitude range used to compute SD values is $\pm$80 degrees, because of HYCOM model ranges $\pm$80.48 in latitude). It was expected to see that both model types show high differences in shelf, coastal and polar areas, which are challenging for purely HD models and HD-based models, because the physics of the models alone is still not enough to fully describe the ocean dynamics, especially in these areas, where complex phenomena occur. Another issue is related to bathymetry information, that can be insufficient due to coarse resolution grids. This becomes problematic especially in shallow waters, where tidal motion is not linear, and in some cases overtides and compound tides can reach 15 mm (Andersen et al., 2006). For constrained models, it is important to remember that in certain areas, altimetry observations may not complement the tidal description of

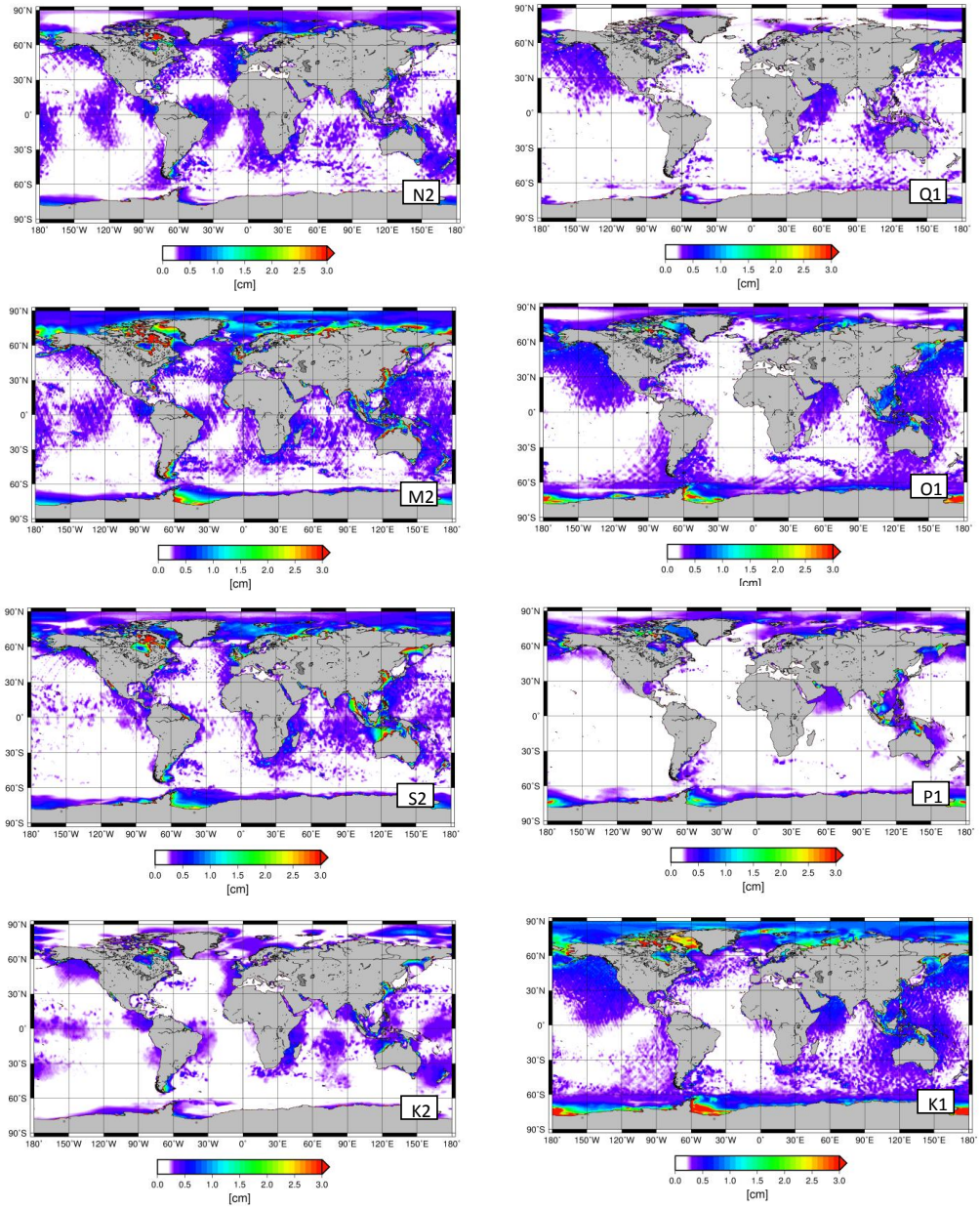

Figure 6.1: SD of major tidal constituents from semi-empirical and assimilative hydrodynamic models.

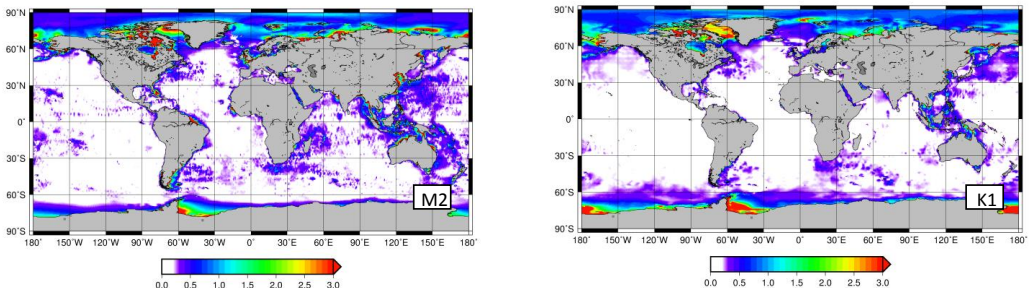

Figure 6.2: SD of M2 and K1 tidal constituents from semi-empirical and assimilative hydrodynamic models, OSU12 excluded.

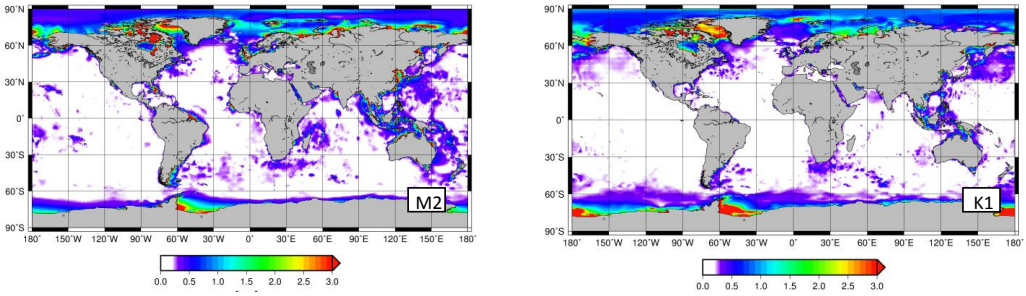

Figure 6.3: SD of M2 and K1 tidal constituents from semi-empirical and assimilative hydrodynamic models, OSU12 and DTU16 excluded.

Tidal Constituent	SD with OSU12	SD without OSU12
M2	8.50	0.88
N2	8.39	0.21
S2	8.44	0.46
K2	8.34	0.19
K1	8.42	0.38
O1	8.40	0.23
Q1	8.31	0.08
P1	8.35	0.20
RSS	23.74	1.14

Table 6.1: Global SD of modern models in cm, with OSU12 (first column) and without OSU12 (second column).

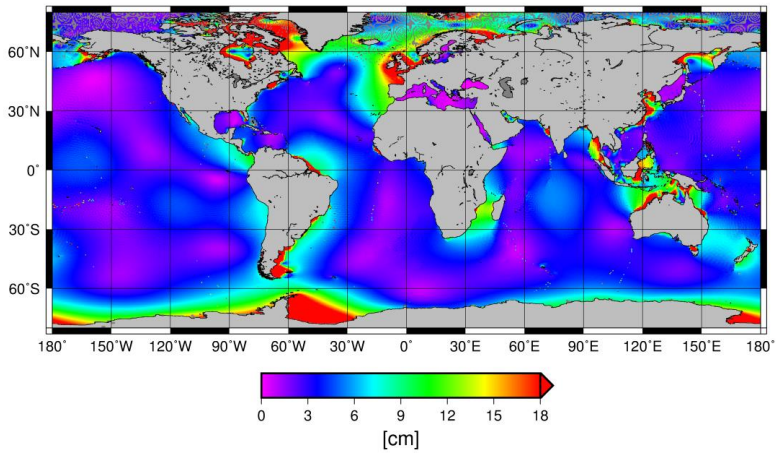

Figure 6.4: SD of M2 tidal constituent between STORMTIDE, HIM, and HYCOM models.

a model, as the quality and quantity of the data may decrease due to the presence of ice, or complex coastal geometry. Also estuarine coastlines are hard to model, as the effects of frictional distortion, sediment transport, and intertidal storage in tidal flats and marshes lead to non-linear tidal distortions (Friedrichs and Aubrey, 1988 and Dronkers, 1986).
In particular, high discrepancies are observed in the Patagonian Shelf, which is a macrotidal region where single-constituent tides like M2 can reach heights of 2.5 m. In this area, it is observed an additional intermittent semi-diurnal signal that cannot be represented by the linear combination of tidal constituents and still remains unpredictable by models (Lago et al., 2017). Another shelf sea characterized by high tidal amplitudes is the North Sea. With a predominant semi-diurnal regime, the lunar component M2 has an average amplitude of 1 m (Huthnance, 1991), and it can reach 3 m in extreme cases. Tides in this area are mainly affected by co-oscillation with the Atlantic, and their complexity is due to the highly variable shape and depth of the basin (Roos et al., 2011). The disagreement between models is primarily in tidal amplitudes of single constituents, especially at distances close to the coast. A similar situation occurs in the semi-enclosed Yellow Sea, which is characterized by shallow depths ranging 90-20 m within 50 km from the coast, high tide ranges along the west coast of Korea, dominant semi-diurnal waves, and three amphidromic systems (Teague et al., 1998). The high tidal amplitudes in this region are hard to model, and altimetry data (especially T/P and Jason-series tracks, which do not have a pathological aliasing) are not helpful in model constraint, as they completely miss the crucial features of this area (Ray et al., 2011). In the Malay Archipelago, diurnal components are strong and predominant at the coast (Ray et al., 2005), and the combination of shallow water, the presence of many islands, and complex ocean dynamics, makes tide modeling challenging. Often, altimetry assimilation in this area is not enough to compensate model errors, as difficult coastal features may hinder the data quality. A special situation occurs in the deep Okhotsk Sea,

where tide models have to face not only large tidal sea-level oscillations that can reach 13 m, but also the presence of pack ice during winter (Kowalik and Polyakov, 1998). Finally, another high disagreement between models is found at coastal areas surrounding Amazon river mouth. The Amazon is defined as a tidal river, i.e. a fluvial environment subject to dynamic tidal action (Freitas et al., 2012), which probably affects models with tidal signal distortion.

These areas are all characterized by specific physical phenomena and complexities, and dedicated regional studies would be of high interest for tide model research and assessment. In this thesis, the author focused on two areas, the North Sea and the Malay Archipelago, where a suitable number of in situ data is available for tide model assessment and comparison.

6.2 Regional analysis of EOT19p model

The EOT algorithm is able to estimate up to 15 tidal components (M2, S2, N2, K2, 2N2, O1, K1, Q1, P1, S1, M4, MM, MF, SA, SSA). However, in this work only the performance for eight major constituents (M2, S2, N2, K2, O1, K1, Q1, P1) is evaluated, in order to compare only constituents in common with other models. Comparisons with EOT11a, FES2014, GOT4.8, and TPXO8 are based on exercises presented in St14, and focus on the agreement analysis between the models and in situ data. Results are displayed in two areas: the North Sea, with geographical extension from -12 to 4 degrees in longitude, and between 49 and 61 degrees latitude; and the Malay Archipelago, ranging between 90 and 150 degrees in longitude, and -15 to 15 degrees in latitude. The choice of performing regional tests on EOT19p, instead of global ones, is justified by one practical limitation: a global solution requires considerable computational time, that makes it difficult to test different approaches within an acceptable time frame.

6.2.1 Tidal elevation differences

Since St14 (and at the time of this study), only three models are available with their new version: FES2014, DTU16, and the regional EOT19p. ■ The SD between these models (henceforth SD2019) has been computed on a common grid of 1/8 degree resolution for all major constituents, and it is compared with the one obtained with their former versions (SD2014), namely FES2012, DTU10, and EOT11a. Figure 6.5 and figure 6.6 show the SD for constituent M2 in the North Sea and the Malay Archipelago respectively. In both regions higher agreement is found for SD2019 at coastal areas, with heavy improvements in complex areas such as the English Channel, or the Java Sea. The SD found in these regions were also computed with respect to the distance to coast: SD grid points within 100 km to the coast were divided and averaged in bins ranging 10 km. Results comparing SD2014 and SD2019

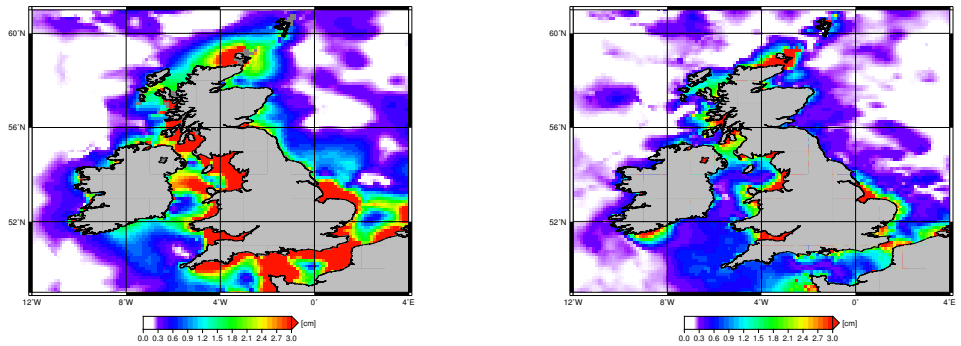

(a) (b)

Figure 6.5: SD2014 (a) and SD2019 (b) for M2 tidal constituent over North Sea in cm.

for M2 tidal constituent are displayed in figure 6.7. Lower disagreement occur with SD2019 in both areas, especially at 15 km to the coast, where there is maximum improvement of 1.6 cm in the North Sea and 0.8 cm in the Malay Archipelago. In tables 6.2 and 6.3 the average of SD computed for both the areas of interest are shown for eight of the major tidal constituents, and the associated Root Sum Squared (RSS) values. The SD is reduced for all constituents in both areas, showing that higher agreement is achieved with the new models. The largest improvements can be observed for M2 and S2 constituents: model agreement for M2 has improved of 2.8 cm in the North Sea and 1.3 cm in the Malay Archipelago, while for S2 there is an improvement of ~1 cm in both regions. SD2019 RSS values show an overall agreement of 0.70 cm in the North Sea and of 1.44 cm in the Malay Archipelago, reducing the differences of 3 cm and 1.6 cm with respect to SD2014 respectively. It must be said that such higher agreement between the new models was expected. Both EOT19p and DTU16 are semi-empirical models, that means that they apply a correction to their background models - FES2014 and FES2012 respectively - by computing residual tidal estimations from altimetric data. FES2014 and FES2012 have not only an enhanced performance with respect to their former version FES2004, but they are also able to estimate a higher number of constituents, most likely reducing the tidal residual signal that can be detected using altimetry. It is thus possible that the residual correction applied by EOT19p and DTU16 is much smaller than in EOT11a and DTU10, making the models more similar to each other, and to FES2014, which is the third model involved in SD2019.

6.2.2 Comparison against in situ data

Tide models are evaluated using tide gauge and shallow water gauge stations. The original grids of every model are bilinearly interpolated at each station, and their performance is compared for eight major tidal constituents.

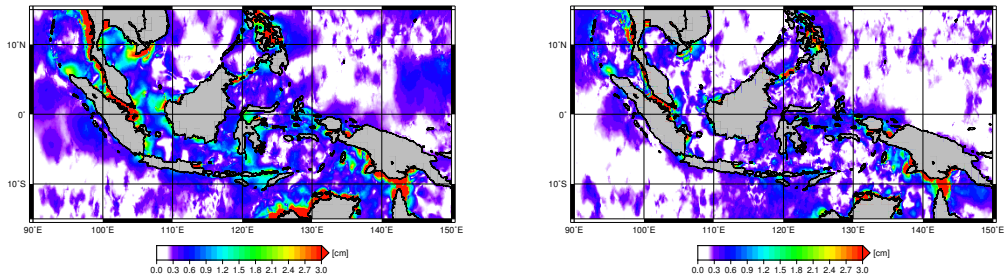

(a) (b)

Figure 6.6: SD2014 (a) and SD2019 (b) for M2 tidal constituent over the Malay Archipelago in cm.

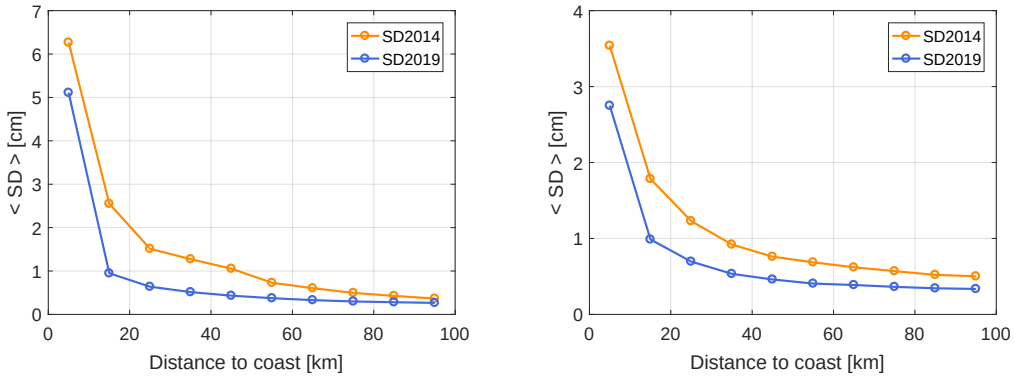

(a) (b)

Figure 6.7: SD2014 (orange) and SD2019 (blue) averaged values with respect to distance to coast for M2 tidal constituent, in the North Sea (a) and in the Malay Archipelago (b).

Constituent	**SD2014 [cm]**	**SD2019 [cm]**
M2	3.33	0.57
N2	0.66	0.19
S2	1.23	0.28
K2	0.41	0.12
K1	0.17	0.09
O1	0.15	0.10
P1	0.91	0.10
Q1	0.12	0.06
RSS	3.75	0.70

Table 6.2: Comparison of SD2014 and SD2019 in the North Sea.

Constituent	SD2014 [cm]	SD2019 [cm]
M2	2.37	1.12
N2	0.52	0.25
S2	1.34	0.49
K2	0.48	0.23
K1	0.81	0.46
O1	0.61	0.39
P1	0.40	0.30
Q1	0.20	0.15
RSS	3.02	1.44

Table 6.3: Comparison of SD2014 and SD2019 in the Malay Archipelago.

Comparison between EOT19p and EOT11a against in situ data

The performance of EOT19p is tested against its former version, EOT11a, through the geometric MAD of in-phase and quadrature components (cf. equation 5.3) and their percentage of relative improvement. In figure 6.8 and figure 6.9 the relative improvement of RSS values, obtained from the RMS of major constituents are shown for both areas of interest. The red markers represent improvements for EOT19p with respect to EOT11a. In general, EOT19p has better performance at the coast, with few exceptions. In the North Sea, strong improvements are observed at gauges located in the English Channel, the Bristol Channel, and the Irish Sea. The shallow water gauge in proximity of Cork shows a worsening with EOT19p, and this is due to a lower accuracy in the phase estimation of S2 and K2 constituents in that area. In the Malay Archipelago moderate improvements are seen below the Equator. The best estimates are found in the Malay Peninsula; however, larger model errors occur in the Malacca Strait where issues for K1 constituent are found for both EOT19p and its background model FES2014. At tide gauges located in Bintulu (113.07E, 3.22N) and Jolo (121E, 6.07N) a lower performance is due to an underestimation of M2 phase. These problems can be attributed to different factors. For example, Jolo station is located in an area where M2 phase changes rapidly between -90 and +70 degrees (Ray et al., 2005), and probably the resolution of the model is not enough to estimate the same phase as the tide gauge. In addition, the quality and the quantity of altimetry data in narrow channels such as the Malacca Strait may not be adequate to resolve tidal residuals - and thus correct the background model. In tables 6.4 and 6.5, MAD values and their relative improvement ΔRMS are displayed for single constituents. MAD values were preferred over averaged root mean square errors because they are less sensitive to outliers, which may occur more often when tide models are compared at coastal areas (St14). In the North Sea, ΔRMS

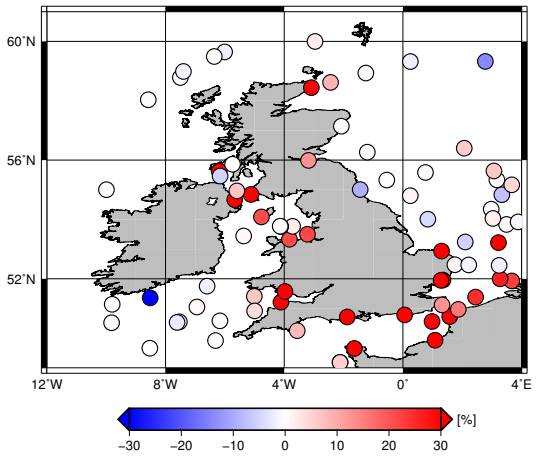

Figure 6.8: RSS relative improvement of EOT19p with respect to EOT11a at single in situ stations in the North Sea.

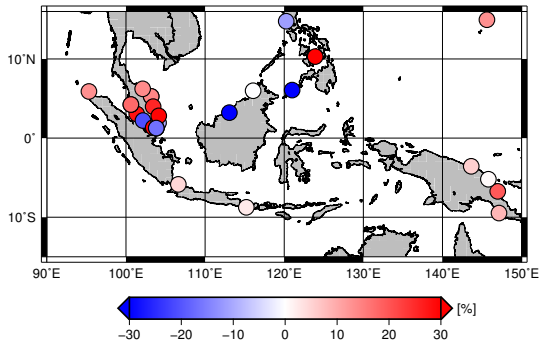

Figure 6.9: RSS relative improvement of EOT19p with respect to EOT11a at single in situ stations in the Malay Archipelago.

values are all positive, indicating better performance of 35.39% for EOT19p with respect to EOT11a, especially for K2 and M2 constituents, with improvements of 51.93% and 32.65% respectively. A similar situation is observed also for the Malay Archipelago. However, a lower performance is observed for K1 constituent, confirming the issue seen at single tide gauge stations.

Performance of EOT19p in comparison with other models

The regional MAD values of EOT19p are compared with the latest version of other existing models in tables 6.6 and 6.7. Note that version 4.8 of GOT model was used instead of its latest release (GOT4.10, Ray, 2013) because of its better performance in shallow water and near coasts (Richard Ray, personal communication). The lowest MAD value of each constituent, and the best RSS are highlighted in bold. In the North Sea DTU16, EOT19p and FES2014 models show best values for single constituents and RSS values. EOT19p

Constituent	**EOT11a [cm]**	**EOT19p [cm]**	ΔRMS [%]
M2	3.40	2.29	32.65
N2	1.13	0.85	24.78
S2	1.81	1.36	24.86
K2	3.89	1.87	51.93
K1	3.15	2.23	29.21
O1	2.22	1.51	31.98
P1	0.95	0.79	16.84
Q1	1.15	1.00	13.04
RSS	6.95	4.49	35.39

Table 6.4: Comparison of MAD for EOT19p and EOT11a in the North Sea.

Constituent	**EOT11a [cm]**	**EOT19p [cm]**	ΔRMS [%]
M2	2.44	1.63	33.26
N2	0.74	0.65	12.51
S2	1.27	1.20	5.37
K2	0.69	0.28	60.42
K1	1.38	1.62	-17.68
O1	1.08	0.58	46.19
P1	0.73	0.47	35.85
Q1	0.27	0.23	16.65
RSS	3.50	2.79	20.07

Table 6.5: Comparison of MAD for EOT19p and EOT11a in the Malay Archipelago.

improves its background model, for single constituents such as M2, of ~ 0.7 cm, and for the total error, with RSS of 4.49 cm. In the Malay Archipelago EOT19p shows a similar behaviour, and larger improvements are observed for M2 and K2 constituents. DTU16 shows lower performance, in comparison with the North Sea, and this is mainly due to a MAD of 4.04 cm for M2. It is worth to notice that the best model for K1 constituent is GOT4.8 with a MAD below the centimetre. The other models range between 1.34 and 2.09 cm, indicating a possible common problem for this particular constituent. Andersen and Knudsen, 1997 showed that issues with K1 occur for altimetry-based tidal models because of the correlation between K1 alias period and the semi-annual and annual cycles. This may also be a reason why EOT19p does not improve its background model in both areas ■. Problems with K1 in Indonesia were also highlighted in Lyard's presentation for 25 years of altimetry, as already mentioned in section 2.4.

Constituent	EOT11a	EOT19p	FES2014	TPXO8	DTU16	GOT4.8
M2	3.40	2.29	2.98	3.02	**2.26**	5.01
N2	1.13	**0.85**	0.96	1.50	1.04	1.77
S2	1.81	1.36	1.32	1.34	1.29	2.34
K2	3.89	1.87	**1.86**	3.08	2.66	4.36
K1	3.15	2.23	**2.05**	2.41	2.27	3.25
O1	2.22	**1.51**	1.66	**1.51**	1.58	2.87
P1	0.95	0.79	**0.73**	1.16	0.94	1.07
Q1	1.15	1.00	**0.98**	1.08	1.09	1.12
RSS	6.95	**4.49**	4.84	5.77	4.97	8.59

Table 6.6: MAD comparison between existing models in the North Sea. Values are in cm.

6.3 Additional studies

6.3.1 The along-track test

Results form the along-track test illustrated in section 4.5.2 are shown in this paragraph. ● One of the most advantageous features of ALES retracker is the large amount of valid coastal measurements available along track. This benefit is shown in terms of observations available for each node. In Figure 6.10 the difference between the number of observations of ALES and the ones retrieved with SGDR are displayed. This difference is expressed as: Δ_{obs}, i.e., observations of ALES minus observations of SGDR. Each dot represents a node along the tracks, plotted against the distance to the coast. The red markers highlight the positive values, that is, the nodes for which ALES provides a larger amount of data with respect to

Constituent	EOT11a	EOT19p	FES2014	TPXO8	DTU16	GOT4.8
M2	2.44	**1.63**	1.98	2.71	4.03	2.95
N2	0.74	0.65	**0.52**	0.84	1.29	1.35
S2	1.27	1.20	**1.05**	1.53	1.60	1.81
K2	0.69	**0.28**	0.42	0.49	1.34	0.83
K1	1.38	1.62	1.34	2.09	1.95	**0.91**
O1	1.08	**0.58**	0.78	1.85	0.98	1.29
P1	0.73	**0.47**	0.50	0.61	1.55	0.86
Q1	0.27	**0.23**	**0.23**	0.48	0.34	0.33
RSS	3.50	**2.79**	2.86	4.36	5.44	4.22

Table 6.7: MAD comparison between existing models in the Malay Archipelago. Values are in cm.

SGDR. The blue dots are used for the negative values. An interesting, yet expected behavior is observed for values below 20 km from the coast: far more observations are available with ALES while approaching the coast, with some exceptions for few points.

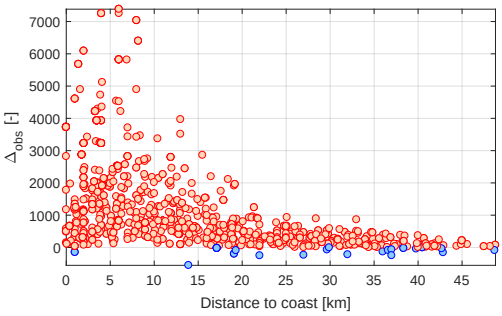

Figure 6.10: Difference in the number of observations between ALES and SGDR at each node against the distance to coast. The blue dots show the cases for which less observations are available for ALES, while the red dots correspond to a larger amount of data for ALES.

An analogous comparison is shown for the variable σ_0, that represents the quality of the least squares fit. In Figure 6.11 a the difference at each node between the σ_0 computed for the SGDR solutions and σ_0 obtained from ALES is shown. A positive value on the y-axis (highlighted with red dots) corresponds to a larger fitting error for the SGDR solutions, and negative values (blue dots) for the contrary. From the plot it is clear that in most cases an improvement for σ_0 is achieved with ALES, with exception for few coastal points. The dependence of σ_0 on the number of observations may explain the smaller errors for ALES. However, from Figure 6.11b one can notice that large improvements in σ_0 are reached also for a lower amount of data. On the other hand, the few cases with larger internal errors may be

found at nodes with more data availability. These special cases, which account for only the 1.5% of the cases, may be justified by residual erroneous estimations in the ALES data, which were not identified by the outlier analysis. In Figure 6.12, the spatial distribution of the

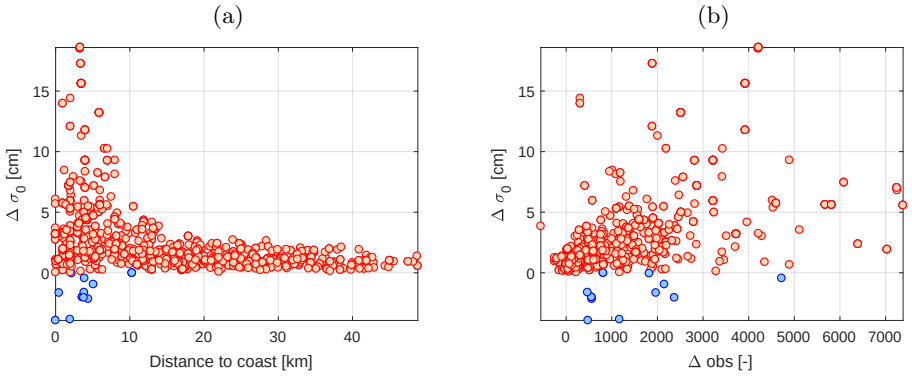

Figure 6.11: Difference of σ_0 values between SGDR minus ALES at each node against the distance to coast (**a**), and against difference in number of observations between ALES and SGDR (**b**).

ΔRSS is shown. The differences are computed using the closest along-track node to the tide gauge (CNTG) that interest each of the 85 tracks. In general, improvements are found for 66 tracks, with an average of 0.4 cm and a maximum value of 1.9 cm. The red dots indicate the highest improvements for the ALES solutions, which are located unevenly between Europe and the American continent. These higher values may be due to improvements to only few single constituents. This can be observed in Figure 6.13, where the absolute ΔRMS of the closest nodes to the tide gauge of interest are plotted against the longitude of the in situ site. The plot is divided in three rows for an easier visualization, and the ΔRMS of each tidal constant is color-coded according to the legend. An example of large improvements for single constituents can be seen at Prince Rupert, western Canada, or Ringhals, Sweden (respectively longitudes: -130.32° and 12.11°), where the values of ΔRMS for M2 and S2 for Prince Rupert, or Q1 and O1 are larger than 2.5 cm. In contrast, there are locations such as La Union, El Salvador, and Swansea, UK (longitudes -87.82° and -3.98°) where the ALES solution shows a loss in performance—again differences larger than 2.5 cm—for constituent M2. The RMS differences for all the 85 tracks are summarized in Table 6.8. The average values were computed using the single RMS values obtained at each site, at the CNTG. A mean improvement of 2 mm can be measured for the ALES solutions with respect to SGDR. It is important to stress that in the global average, results based on ALES are superior to results based on SGDR for every constituent. For K2, O1 and P1 the improvement is over 10%. For Q1, the improvement is over 25%. For larger RMS (such as M2 and S2) a minor

effect of ALES is observed for the relative differences.

Constituents	RMS_{ALES} [cm]	RMS_{SGDR} [cm]	ΔRMS %
M2	8.0	8.2	2.4
N2	2.1	2.3	8.7
S2	3.5	3.7	5.4
K2	1.4	1.6	12.5
K1	2.1	2.2	4.5
O1	1.4	1.6	12.5
Q1	0.8	1.1	27.3
P1	1.2	1.4	14.3

Table 6.8: Average of RMS for major constituents for the closest points to the tide gauges. The values are expressed in cm. The last column shows the relative difference between the two solutions.

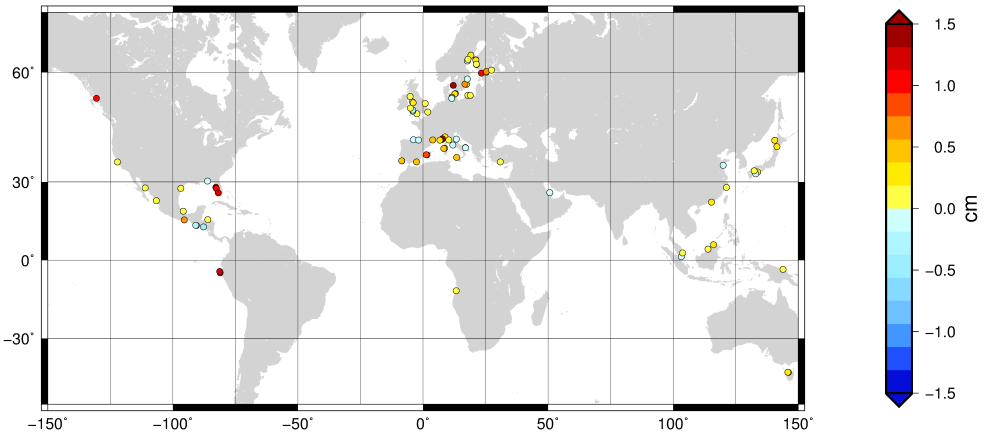

Figure 6.12: Geographical distribution of the ΔRSS (in cm) for the closest nodes to the tide gauge of interest.

Study of the Dependencies

Also in this section, the CNTGs are used to study the performances of the two retracker solutions. It must be pointed out that the CNTGs may not coincide with the closest points to the coast, as they depend on the position of the track with respect to land. For this reason, it was chosen to analyze the ΔRSS values against the distance to coast (Figure 6.14a) as well as against the distance to the tide gauge of interest (Figure 6.14b). The first plot shows not only that the nodes are mostly concentrated within 10 km to the coast, but also that improvements with ALES larger than 0.5 cm occur for nodes closer than 5 km. On the other

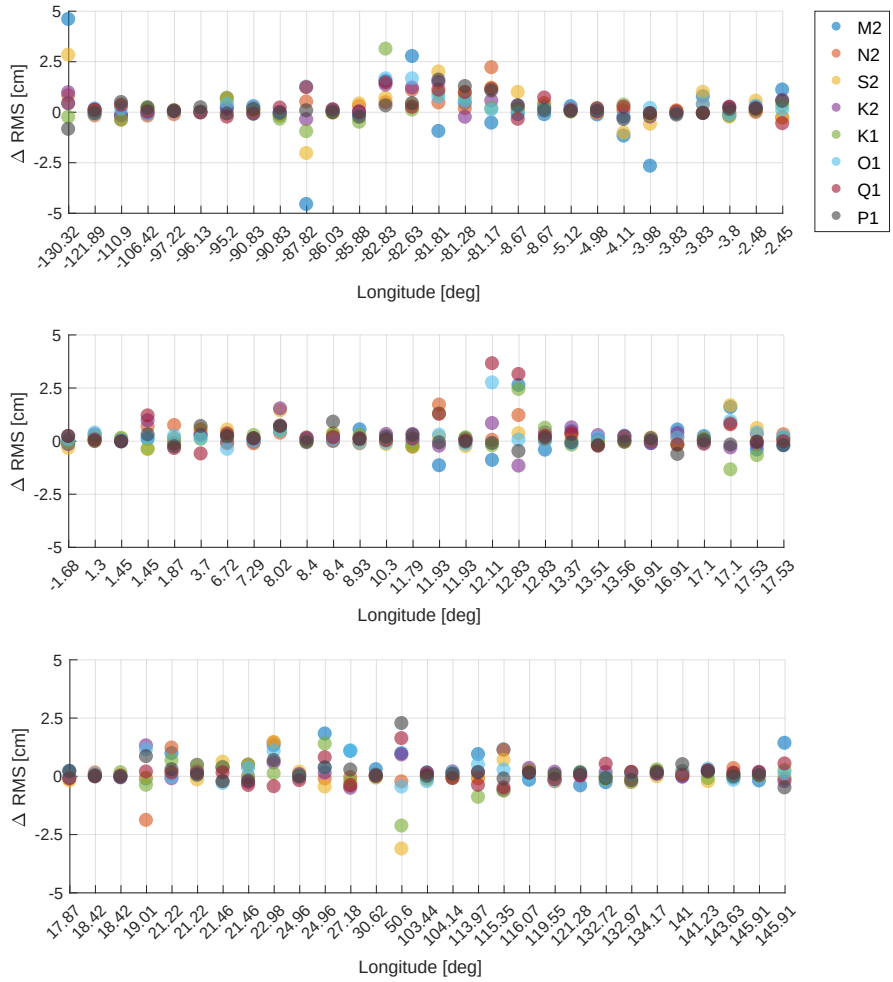

Figure 6.13: Difference of RMS for major constituents at the CNTG. The values are plotted against the longitude of their location.

hand, no visible dependency is observed between the values of ΔRSS and their distance from the tide gauge: in fact, the same improvements over 0.5 cm appear also for distances above 20 km. The dependency on the distance to the coast is also shown for the ΔRMS of the single constituents, Figure 6.15. Within 10 km from the coast, improvements below 2 cm can be found for all constituents. Larger variability is observed for the major constituents, and single values can reach e.g., ±5 cm for M2 and ±3 cm for S2. Another aspect analyzed is the influence of the track direction on the results, because the performance of a retracker may change whether the satellite approaches land from ocean or flies from ocean to land, as well as if there is a bay (case: land-ocean-land) or the coast is parallel to the track (case: parallel to land). These results are shown in Table 6.9. The four main headers indicate the track position and the number of tracks used for the RMS average. The RSS computed from the RMS averages for each case are also displayed in the last row of the table. In general, lower values are found for the ALES solution, with exception of few constituents. An interesting

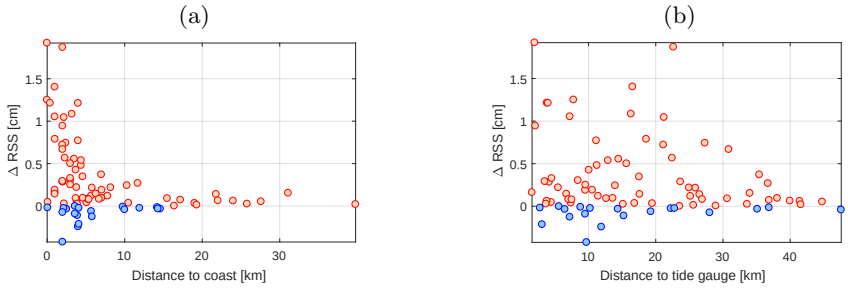

Figure 6.14: Difference of RSS against distance to coast (**a**) and tide gauge (**b**) in km. The values are shown for the closest nodes to the tide gauge of interest.

result regards the transition land/ocean (i.e., the first four columns): both SGDR and ALES solutions show a higher performance for all constituents for the case ocean-to-land, against the land-to-ocean results, reaching differences larger than 1 cm for single constituents. This can be seen also from the averaged RSS, which show discrepancies of 26 mm between the ALES solutions and 21 mm for SGDR. This situation may be justified by a different behavior of the on-board tracker according to the flight direction, which may consequently influence the performance of the retrackers (Passaro et al., 2014). A clear example is presented in Figure 6.16, where the RMS of constituent M2, computed for the ALES solution, is plotted for the nodes of tracks 111 and 92. Track 111 is ascending, and it goes from ocean to land, while track 92 is descending, going from land to ocean. It can be observed, that even though few nodes at track 92 are closer to the tide gauge, they still show a larger RMS with respect to nodes belonging to track 111. Moreover, larger discrepancies are found between ALES and SGDR for the case ocean-to-land, for which RSS values differ of 6 mm against 1 mm in the land-to-ocean case. Unfortunately, for the cases land-ocean-land and parallel-to-land only few tracks were available. However, from both the single RMS and the RSS values similar performance is found between ALES and SGDR solutions. Finally, the sea state dependency is shown for the absolute ΔRSS. It was chosen to represent the sea state as the average of the SWH at each node, plus its standard deviation. The SWH values are taken from the ALES product. While the improvement of the ALES data for calm sea states (<2.5 m) is expected (Passaro, 2015), the available literature concerning data quality in comparison with SGDR for wavy seas is still scarce. Indeed, from Figure 6.17, relevant improvements (>0.5 cm) are observed for sea states within 2.5 m, while only few examples are available for high states. However, ΔRMS > 1 cm are found above 3 m, showing no sensitive relation between the sea state and the data analyzed ●.

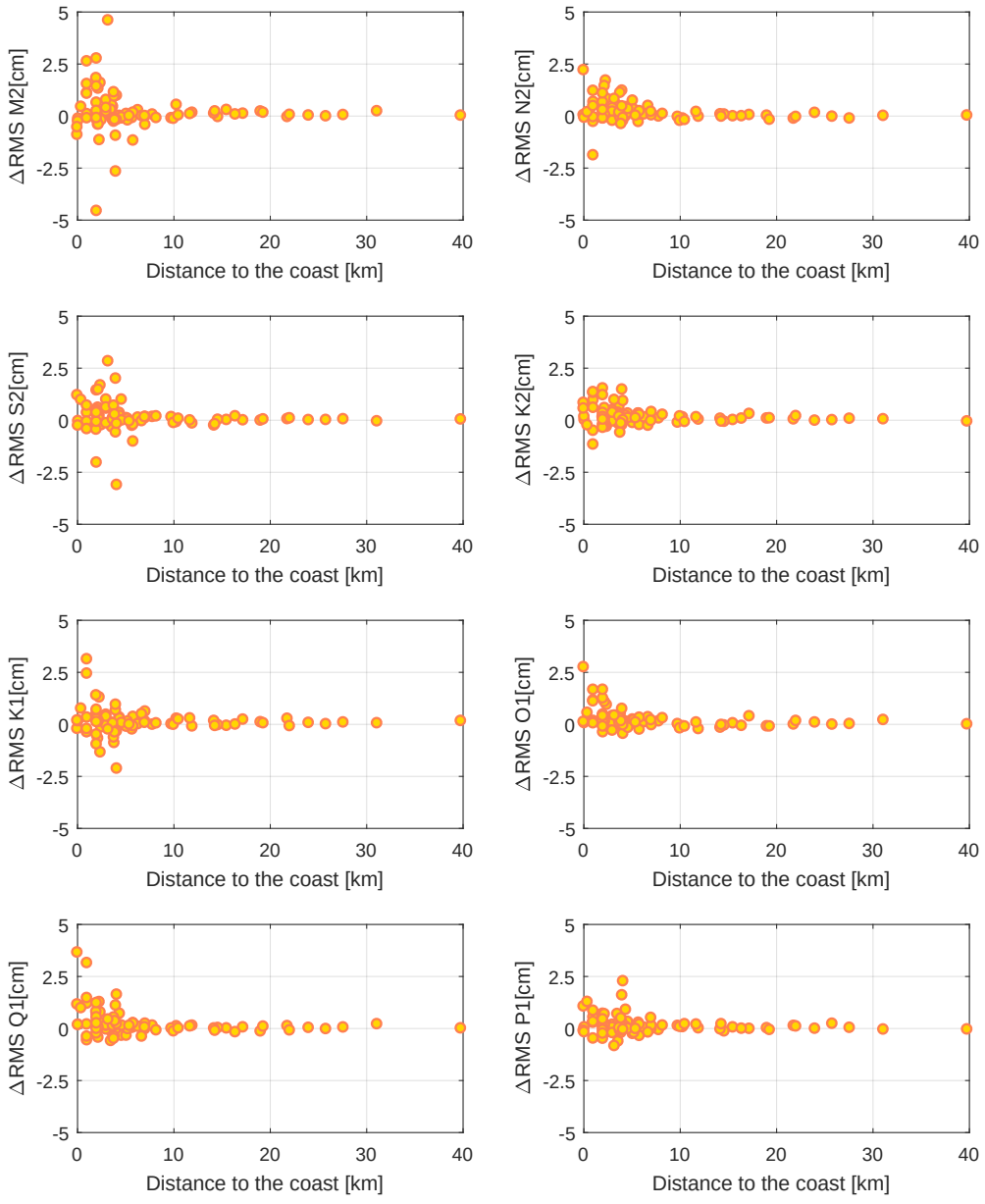

Figure 6.15: Absolute ΔRMS of major constituents at the CNTG. The values are plotted against the distance to the coast (in km).

Constituents	Land to Ocean: 30		Ocean to Land: 34		Land-Ocean-Land: 15		Parallel to Land: 6	
	RMS_{ALES}	RMS_{SGDR}	RMS_{ALES}	RMS_{SGDR}	RMS_{ALES}	RMS_{SGDR}	RMS_{ALES}	RMS_{SGDR}
M2	6.6	6.9	4.8	5.0	19.3	19.2	4.6	4.7
N2	1.7	1.8	1.3	1.6	4.8	5.2	1.4	1.4
S2	3.1	3.2	2.1	2.4	7.7	7.8	2.6	2.5
K2	1.2	1.3	1.0	1.3	2.8	2.9	1.7	1.7
K1	1.9	1.9	1.4	1.5	3.8	4.2	2.2	2.2
O1	1.2	1.3	1.0	1.3	2.5	2.7	1.6	1.6
Q1	0.8	0.9	0.7	1.0	1.3	1.8	0.9	1.0
P1	1.5	1.7	0.7	0.9	1.9	1.9	1.1	1.2
RSS	8.4	8.5	5.8	6.4	22.1	22.8	6.5	6.6

Table 6.9: Average of RMS computed for major constituents at the closest points to the tide gauges. The averages are computed after dividing the tracks according to their position with respect to the coast. The values are in cm.

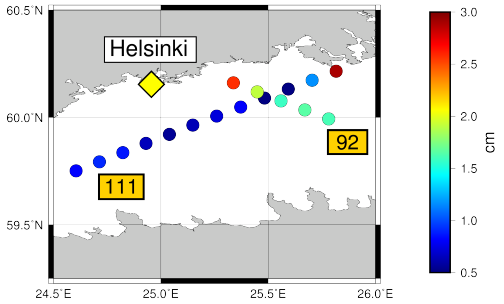

Figure 6.16: RMS values for M2 constituent computed with ALES solutions for tracks 111 (ascending) and 92 (descending). The diamond-shape marker represent the tide gauge station of Helsinki. The round markers are the along-track nodes and the RMS with respect to the tide gauge is color-coded.

6.3.2 Tests with alternative cap size choice

At the time of these tests, the algorithm was not yet optimized, and therefore computation of tidal estimates was highly time-demanding. For this reason, these alternative solutions on grid node caps were tested on a limited area in the North Sea, between 10E and 2E longitude and 50N and 52N in latitude. In this area, shelf-water and coastal gauges were available for the assessment. Results obtained with fixed cap size at each grid node (EOT_{FC}), are compared with alternative solutions derived from node cap size that vary according to bathymetry (EOT_{VC}) and from node caps with selective mask (EOT_{SM}), cf. 4.5.1. In table 6.10 the RMS and RSS errors of EOT_{FC}, EOT_{VC}, and EOT_{SM} against in situ stations are shown, together with results got from EOT11a and FES2014 global models. The value $< RSS >$ represents the average of RSS values obtained at single stations. All solutions computed with the EOT algorithm presented beforehand, have a lower error than the former EOT11a, with large differences for constituents M2 and M4, and improve both RSS values of 1.5–2 cm. Improvements are also observed against their background model, which shows a higher error for M2 constituent. This result holds at single in situ stations (figure 6.18), where all solutions clearly outperform EOT11a im most locations. However, EOT_{VC} and EOT_{SM} alternative solutions have still higher errors than EOT_{FC}, which outperforms all models for constituents M2 and S2, with a consequent improvement of RSS values. A possible explanation for a lower performance of these alternative solutions may be related to the use of a lower amount of altimetry data at each node. Less data could give problems with aliasing or constituent separation. Also, smaller (or selective) cap sizes may cut out Jason tracks, that have lower spatial resolution than ESA missions. Jason tracks are by construction more suitable for tide observation, and if left out, constituents like S2 may not be well represented with only ESA data, characterized by tide-pathological orbits.

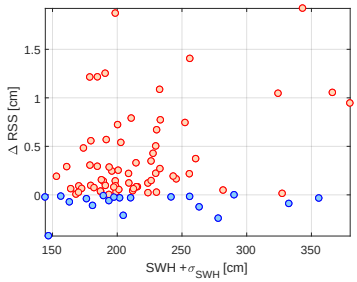

Figure 6.17: ΔRSS absolute values for the closest node to the tide gauge against the sea state, represented as the averaged SWH computed at each node plus its standard deviation.

Constituent	EOT_{FC}	EOT_{VC}	EOT_{SM}	$EOT11a$	$FES2014$
M2	**3.84**	3.94	3.88	5.29	4.43
N2	2.04	2.04	2.03	2.02	**1.82**
S2	**1.67**	1.69	2.08	2.38	1.80
K1	1.06	0.99	1.17	0.91	**0.89**
O1	0.73	0.75	0.78	0.69	**0.68**
Q1	0.74	**0.73**	0.75	0.88	0.84
M4	0.57	0.59	0.73	2.22	**0.39**
RSS	**4.92**	5.00	5.16	6.62	5.32
$< RSS >$	**6.14**	6.23	6.51	7.97	6.68

Table 6.10: Comparison of RMS and RSS values of EOT_{FC}, EOT_{VC}, and EOT_{SM} results with $EOT11a$ and $FES2014$ models in Bristol Channel area. Results in cm.

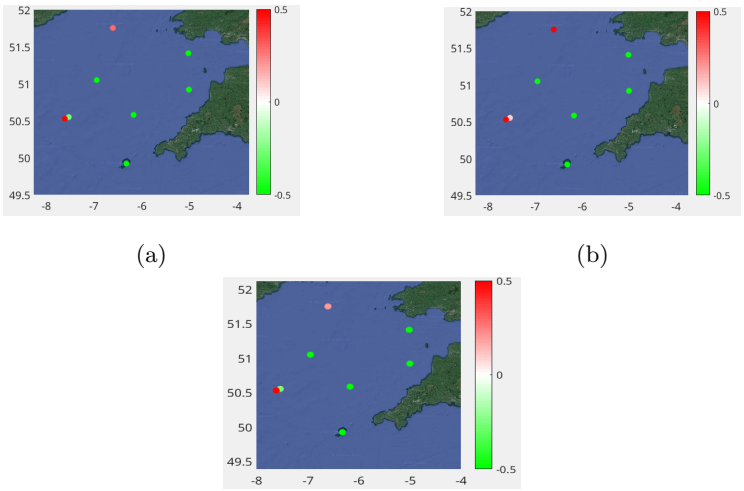

(a) (b)

(c)

Figure 6.18: ΔRSS values at in situ stations. $EOT_{FC} - EOT11a$ in (a), $EOT_{VC} - EOT11a$ in (b), and $EOT_{SM} - EOT11a$ (c). The green markers represent in situ stations where EOT_{FC}, EOT_{VC}, and EOT_{SM} improve EOT11a. Colorbar in cm.

Chapter 7

Conclusion and future work

7.1 Conclusion

This work was dedicated to the research of improved solutions for tide estimation at coastal areas. It has been demonstrated that coast-dedicated products can make the difference, at both along-track and grid points, and results at regional scales showed that the algorithm presented can improve tide model performances with respect to state-of-the art models. In particular, the research questions formulated in chapter 1 have been addressed throughout this thesis, and can be summarised in the following points:

- The impact analysis of dedicated coastal products on tide estimation has been focused on retrackers, and especially on the ALES retracker. In this experiment, ALES has been compared against the SGDR ocean retracker. The experiment shows that the largest improvements obtained with ALES are detected at distances within 10 km to the coast, independently from the geographical location and the sea state. In addition, no evident dependency is found for the RMS improvements to the distance to tide gauges. The results over the track nodes showed an average improvement of 0.4 cm for 66 tracks. Also, the averaged RMS suggest a mean impact of few mm for all tidal constants. The ΔRMS highlighted a positive impact of ALES for single constituents, which can reach values >2.5 cm. In conclusion, improvements independent from the node position, together with a lower fitting error and a large data availability, make ALES a favorable choice for coastal tidal analysis. Indeed, the retracker has been exploited within the EOT19p algorithm.

- The research towards improved solutions for coastal tide estimates with respect to the former algorithm started with the choice of a new, coast-dedicated altimetric dataset. After assessing the impact of ALES coastal retracker, other coastal products have been used to build this new dataset. In particular, the FES2014 hydrodynamic model

was used as background correction, in order to exploit its higher performance at shelf and coastal areas. Together with the VCE, these specific corrections are crucial at the coast, where sea level observations are often scarce or poor. Also, instead of a regular grid, it has been adopted a special grid for tidal residual computation, which was a compromise between computational time reduction and resolution; finally, a latitude-variable radius of interest for each grid node was chosen rather than a fixed-size radius, so that the selection of SLA observations at high latitudes is not affected by denser data distribution. Other solutions were researched to improve coastal tide estimates: variable node cap sizes depending on the ocean depth, and on the presence of land, were also tested, but they didn't show significant improvements and remained particularly time-demanding in comparison with other solutions.

- The new algorithm has been tested on regional scales, in particular in the Malay Archipelago and in the North Sea. It shows higher performance with respect to EOT11a with RSS relative improvements of 35.39% in the North Sea and 20.07% in the Malay Archipelago. Heavy improvements occur at gauges located in complex coastal areas, such as the English Channel or the Irish Sea. With this algorithm is it possible to obtain the lowest error compared to the latest models, and improvements for single constituents with respect to its background model, in particular for M2 constituent, in both regions (improvements of 0.7 cm and 0.35 cm in the North Sea and the Malay Archipelago respectively), and the final RSS values. The results obtained with EOT19p algorithm in such challenging regions are clearly supported by an enhanced performance of its background model. However, the improvements of the model with respect to FES2014 indicate that the use of updated altimetric products, specific for coastal purposes, represent an asset for tidal estimation in complex areas. This conclusion is further encouraged by the results obtained in the along-track study, where tidal estimates at single tracks could improve up to ~1.5 cm.

7.2 Future work

The improvements shown in this study were found despite the ALES retracking strategy was only applied in the residual analysis of the EOT procedure, while the original FES2014 model, which corrects for most of the tidal variability, is still based on SGDR data. It is therefore expected that the use of ALES data could bring a decisive improvement in coastal tide modeling if used as a data source to estimate the full tidal component of the sea level variability. Also, it is important to highlight that sea level residuals were derived using the FES2014 values interpolated on a regular grid with 1/16 degree resolution. Nevertheless, the original FES2014 model is characterized by a much higher resolution, that becomes finer

at coastal zones. The use of this mesh would be of great benefit for coastal altimetry, which could also be exploited at higher resolution itself (at 20 Hz instead of 1 Hz). Further investigations in this direction, and those aimed to quantify the impact of additional altimetric corrections on the tidal estimation at the coast, are highly recommended by the author.
Moreover, a further study about the impact of EOT19p on the reduction of SLA variances is recommended. This test would tell whether the predicted tidal corrections effectively reduce the noise of altimetry measurements. However, SLA variance reduction close to the coast shall be analysed carefully, because other signals typical of these areas may be removed, and the noise is systematically reduced. In fact, this kind of test shall be coupled with a global analysis of ground-track crossover residuals, which is a standard practice used as key indicator of data quality (Passaro, 2015).
An additional validation could be extended to the exploitation of EOT19p in synergistic ocean products, in order to evaluate its performance within ocean models.
The author's considerations about the calculation of the error of the model have been already summarized in chapter 4. However, it is important to stress that at the moment, ocean tide models are provided without associated error estimates. However, a precision measurement of ocean tides is highly desirable, especially for the different applications in which tides are involved, such as operational forecasts.
In addition, few words must be spent about the fact that in this work the loading component has not been considered. Altimeters observe the elastic tide, which is the result of ocean and loading tides. These components are separated in a second moment after processing the tide model, through the spherical harmonic analysis. For this step, it is necessary that the tide model (or its residual part) has a global coverage. At the moment EOT19p is available only at regional scale and it was not possible to remove the loading residuals from the elastic residual. At this point one can make the following considerations: first, we are working on tidal residuals that can be assumed to be small, as the main tidal signal should be already removed with FES2014 model; secondly, the loading tide is generally between $4-6\%$ of the elastic tide (Cheng and Andersen, 2011). This means that for a residual tide of 1 cm, the value of the loading tide should be around ~0.5 mm, which is negligible with respect to the pure ocean tidal signal. So, the global version of EOT19p would be beneficial also in terms of loading tide determination, which is not only needed in altimetry corrections, but also for the update of geodetic products, such as the International Terrestrial Reference Frame.
Another issue to be faced is the computation of S1 tidal constituent. S1 is classified as "radiational" tide, as its main cause is the daily insolation of the atmosphere, that entails a variation of the atmospheric pressure, and a consequent variation of sea level. The gravitational component of S1 also exists, however, it has been shown that its contribution to the total signal is of no significance (Ray and Egbert, 2004). For this reason, nowadays GOT

tide models (namely, versions 4.8a and 4.10a) contain an ad-hoc correction for radiational tides based on global barometric models, such as the one illustrated in Ray and Ponte, 2003. This correction is generally no higher than 1.4 mm (Ray, 2013), however, it represents a critical aspect in geodetic applications which nowadays require a high level of precision from tide models (Ray and Egbert, 2004). Therefore such correction would be crucial in current tide models.

Finally, it is worth to mention that the interest of the tide community is currently moving toward the concept of internal tides, river-driven tides, and tidal currents. Investigations on these specific phenomena shall be considered, as they would have a crucial role in the next years, with the launch of the SWOT mission. Therefore, it is hoped that the promising results obtained with EOT19p will encourage the community to improve and exploit the model for further studies in specific tidal applications and coastal oceanography.

Appendix A

Acronyms and Abbreviations

ALES	Adaptive Leading Edge Subwaveform
BPR	Bottom Pressure Recorders
CLS	Collect Localisation Satellites
CNES	Centre National d'Études Spatiales
CNTG	Closest Point to Tide Gauge
CTOH	Center for Topographic studies of the Ocean and Hydrosphere
DAC	Dynamic Atmospheric Correction
DTU16	Technical University of Denmark tide model
ECMWF	European Centre for Medium-Range Weather Forecasts
EOT	Empirical Ocean Tide model
EOT19p	EOT 2019 preliminary version
ERA	ECMWF Re-Analysis
ERS	European Remote Sensing mission
FES	Finite Element Solution tide model
GDR	Geophysical Data Records
GESLA	Global Extreme Sea Level Analysis
GOT	Goddard Ocean Tide model
HAMTIDE	Hamburg direct data Assimilation Methods for TIDEs
HICOM	HYbrid Coordinate Ocean Model
HIM	Hallberg Isopycnal Model
LEGOS	Laboratoire d'Études en Géophysique et Océanographie Spatiales
LTE	Laplace Tidal Equations
MAD	Median Absolute Differences
MOG2D	2D Gravity Waves model
NIC09	NOAA Ionosphere Climatology 2009
NOAA	National Oceanic and Atmospheric Administration
OpenADB	Open Altimetry DataBase

OSU	Oregon State University tide model
PISTACH	Prototype Innovant de Système de Traitement pour les Applications Côtières et l'Hydrologie
RMS	Root Mean Square
RSS	Root Sum Squared
SD	Standard Deviation
SDR	Sensor Data Records
SLA	Sea Level Anomaly
SWOT	Surface Water and Ocean Topography mission
TICON	TIdal CONstants dataset
TPXO8	TOPEX/Poseidon Crossover (XO) solution 8
T-UGO	Toulouse Unstructured Grid Ocean model
VCE	Variance Component Estimation
VMF	Vienna Mapping Function
WLS	Weighted Least Squares
WOCE	World Ocean Circulation Experiment

Bibliography

Amiri-Simkooei, A. (2013). Application of least squares variance component estimation to errors-in-variables models. *Journal of Geodesy*, 87:935–944.

Andersen, O. A., Knudsen, P., and Stenseng, L. (2018). The DTU18MSS Mean Sea Surface technical description. Oral presentation at OSTST Meeting, 27–28 Sept., Ponta Delgada, Azores, Portugal.

Andersen, O. A. and Scharroo, R. (2011). Range and geophysical corrections in coastal regions: and implications for mean sea surface determination. In Vignudelli, S., Kostianoy, A. G., Cipollini, P., and Benveniste, J., editors, *Coastal Altimetry*, chapter 5, pages 103–145. Springer-Verlag.

Andersen, O. B. (1995). Global ocean tides from ERS 1 and TOPEX/POSEIDON altimetry. *Journal of Geophysical Research,*, 100:25249–25260.

Andersen, O. B. (1999). Shallow water tides in the northwest European shelf region from TOPEX/POSEIDON altimetry. *Journal of Geophysical Research*, 104(C4):7729–7741.

Andersen, O. B., Egbert, G. D., Erofeeva, S. Y., and Ray, R. D. (2006). Mapping nonlinear shallow-water tides: A look at the past and future. *Ocean Dynamics*, 56(5-6):416–429.

Andersen, O. B. and Knudsen, P. (1997). Multi-satellite ocean tide modelling - The K1constituent. *Progress in Oceanography*, 40(1-4):197–216.

Andersen, O. B. and Knudsen, P. (2009). Dnsc08 mean sea surface and mean dynamic topography models. *Journal of Geophysical Research: Oceans*, 114(C11).

Andersen, O. B. and Piccioni, G. (2016). Recent Arctic Sea Level Variations from Satellites. *Frontiers in Marine Science*, 3(2296-7745).

Anderson, J. (2006). *Digital Transmission Engineering*. IEEE Series on Digital & Mobile Communication. Wiley.

Arbic, B. K., Arbor, A., Richman, J. G., F., S., Timko, P. G., Metzger, E. J., and Wallcraft, A. J. (2012). Global modeling of internal tides within an eddying ocean general circulation model. *Oceanography*, 25.

Arbic, B. K., Wallcraft, A. J., and Metzger, E. J. (2010). Concurrent simulation of the eddying general circulation and tides in a global ocean model. *Ocean Modelling*, 32(3):175 – 187.

AVI-NT-02-101-CN (1996). *AVISO user handbook for merged TOPEX/Poseidon products. Edition 3.0*.

Batoula, S. (2009). *ENVISAT RA-2/MWR Level 2 User Manual. Version 1.3*. Féménias, P. Ed.

Bonnefond, P., Haines, B. J., and Watson, C. (2011). In situ Absolute Calibration and Validation: A Link from Coastal to Open-Ocean Altimetry. In Vignudelli, S., Kostianoy, G. A., Cipollini, P., and Benveniste, J., editors, *Coastal Altimetry*, pages 259–296. Springer Berlin Heidelberg, Berlin, Heidelberg.

Bosch, W., Dettmering, D., and Schwatke, C. (2014). Multi-mission cross-calibration of satellite altimeters: Constructing a long-term data record for global and regional sea level change studies. *Remote Sensing*, 6(3):2255–2281.

Bosch, W., Savcenko, R., Flechtner, F., Dahle, C., Mayer-Gürr, T., Stammer, D., Taguchi, E., and Ilk, K.-H. (2009). Residual ocean tide signals from satellite altimetry, GRACE gravity fields, and hydrodynamic modelling. *Geophysical Journal International*, 178(3):1185–1192.

Brandt, S. (2014). *Data Analysis – Statistical and Computational Methods for Scientists and Engineers*. Springer International Publishing.

Brown, G. (1977). The average impulse response of a rough surface and its applications. *IEEE Transactions on Antennas and Propagation*, 25(1):67–74.

Cancet, M., Andersen, O. B., Lyard, F., Schultz, A., Cotton, D., and Benveniste, J. (2016). A new high resolution tidal model in the Arctic Ocean. Proceeding for ESA Living Planet Symposium 2016, Prague, Czech Republic.

Carrère, L., Faugère, Y., and Ablain, M. (2016). Major improvement of altimetry sea level estimations using pressure-derived corrections based on ERA-Interim atmospheric reanalysis. *Ocean Science*, 12(3):825–842.

Carrère, L. and Lyard, F. (2003). Modeling the barotropic response of the global ocean to atmospheric wind and pressure forcing - comparisons with observations. *Geophysical Research Letters*, 30(6).

Carrère, L., Lyard, F., Cancet, M., and Guillot, A. (2015). FES 2014, a new tidal model on the global ocean with enhanced accuracy in shallow seas and in the Arctic region.

Cartwright, D. E. (1999). *Tides: A Scientific History*. Cambridge University Press.

Cartwright, D. E. and Edden, A. C. (1973). Corrected tables of tidal harmonics. *Geophysical Journal of the Royal Astronomical Society*, 33(3):253–264.

Cartwright, D. E. and Ray, R. D. (1991). Energetics of global ocean tides from Geosat altimetry. *Journal of Geophysical Research*, 96(C9):16897–16912.

Cartwright, D. E. and Tayler, R. J. (1971). New computations of the tide-generating potential. *Geophysical Journal of the Royal Astronomical Society*, 23(1):45–73.

Chelton, D. B., Walsh, E. J., and MacArthur, J. L. (1989). Pulse compression and sea level tracking in satellite altimetry. *Journal of Atmospheric and Oceanic Technology*, 6(3):407–438.

Cheng, Y. and Andersen, O. A. (2017). Towards further improving dtu global ocean tide model in shallow waters and polar seas. poster at ostst meeting, miami, fl, usa.

Cheng, Y. and Andersen, O. B. (2011). Multimission empirical ocean tide modeling for shallow waters and polar seas. *Journal of Geophysical Research*, 116(C11):C11001.

Cheng, Y., Andersen, O. B., and Knudsen, P. (2015). An Improved 20-Year Arctic Ocean Altimetric Sea Level Data Record. *Marine Geodesy*, 38(2):146–162.

Chitode, J. S. (2008). *Principles of Communication*. Technical Publications.

Cipollini, P., Calafat, F. M., Jevrejeva, S., Melet, A., and Prandi, P. (2017). Monitoring Sea Level in the Coastal Zone with Satellite Altimetry and Tide Gauges. *Surveys in Geophysics*, 38(1):33–57.

Cipollini, P. and Snaith, H. (2015). A short course on altimetry. 4th ESA advanced training on ocean remote sensing. IFREMER, Brest, France.

Darwin, G. (1875–1889). Tides – encyclopaedia britannica 9th edition.

Darwin, G. (1899). *The tides and kindred phenomena in the solar system*. Boston, Houghton.

Deng, X. (2004). Improvement of geodetic parameter estimation in coastal regions from satellite radar altimetry. PhD thesis. Curtin University of Technology, Perth, Australia.

Dettmering, D. and Bosch, W. (2010). Global calibration of jason-2 by multi-mission crossover analysis. *Marine Geodesy*, 33(sup1):150–161.

Di Bella, A. (2019). Measurement of arctic sea ice from satellite altimetry: the potential and limitations of cryosat-2 sarin mode. PhD thesis. Technical University of Denmark, Lyngby, Denmark.

Doodson, A. T. (1921). The Harmonic Development of the Tide-Generating Potential. *Proceedings of the Royal Society A: Mathematical, Physical and Engineering Sciences*, 100(704):305–329.

Doodson, A. T. and Warburg, H. D. (1941). *Admiralty manual of tides*. Hydrographic Department, Admiralty.

Dronkers, J. (1986). Tidal asymmetry and estuarine morphology. *Netherlands Journal of Sea Research*, 20(2):117 – 131.

Egbert, G. D. and Erofeeva, S. Y. (2002). Efficient inverse modeling of barotropic ocean tides. *Journal of Atmospheric and Oceanic Technology*, 19(2):183–204.

Egido, A. and Smith, W. H. F. (2017). Fully focused sar altimetry: Theory and applications. *IEEE Transactions on Geoscience and Remote Sensing*, 55(1):392–406.

Eicker, A. (2008). Gravity Field Refinement by Radial Basis Functions from In-situ Satellite Data. PhD thesis, Institut für Geodäsie und Geoinformation der Universität Bonn, Bonn, Germany.

ESA (1993). *ERS user handbook*. ESA Publications Division c/o ESTEC, Noordwijk, The Netherlands. Battrick, B. Ed.

Fernandes, M. J., L., Ablain, M., and Pires, N. (2015). Improved wet path delays for all esa and reference altimetric missions. *Remote Sensing of Environment*, 169:50–74.

Fernandes, M. J. and Lázaro, C. (2016). GPD+ wet tropospheric corrections for Cryosat-2 and GFO altimetry missions. *Remote Sensing*, 8(10).

Fok, H. S. (2012). Ocean tides modeling using satellite altimetry. geodetic science rep. no. 501, ohio state univ., columbus.

Foreman, M. G. G., Cherniawsky, J. Y., and Ballantyne, V. A. (2009). Versatile harmonic tidal analysis: Improvements and applications. *Journal of Atmospheric and Oceanic Technology*, 26(4):806–817.

Foreman, M. G. G. and Henry, R. F. (1989). The harmonic analysis of tidal model time series. *Advances in Water Resources*, 12(3):109–120.

Francis, O. and Mazzega, P. (1990). Global charts of ocean tide loading effects. *Journal of Geophysical Research: Oceans*, 95(C7):11411–11424.

Freitas, P. T. A., Silveira, O. F. M., and Asp, N. E. (2012). Tide distortion and attenuation in an Amazonian tidal river. *Brazilian Journal of Oceanography*, 60:429 – 446.

Friedrichs, C. T. and Aubrey, D. G. (1988). Non-linear tidal distortion in shallow well-mixed estuaries: a synthesis. *Estuarine, Coastal and Shelf Science*, 27(5):521 – 545.

Fu, L. and Cazenave, A. (2001). *Satellite Altimetry and Earth Sciences*. Academic Press, San Diego.

Gill, A. E. (2016). *Atmosphere—Ocean Dynamics*. Elsevier Science.

Godin, G. (1972). *The Analysis of Tides*. University of Toronto Press.

Golub, G. and Van Loan, C. (2013). *Matrix Computations*. Johns Hopkins Studies in the Mathematical Sciences. Johns Hopkins University Press.

Gómez-Enri, J., Vignudelli, S., Quartly, G. D., Gommenginger, C. P., Cipollini, P., Challenor, P. G., and Benveniste, J. (2010). Modeling envisat ra-2 waveforms in the coastal zone: Case study of calm water contamination. *IEEE Geoscience and Remote Sensing Letters*, 7(3):474–478.

Gommenginger, C., Thibaut, P., Fenoglio-Marc, L., Quartly, G., Deng, X., Gómez-Enri, J., Challenor, P., and Gao, Y. (2011). Retracking altimeter waveforms near the coasts. In Vignudelli, S., Kostianoy, A. G., Cipollini, P., and Benveniste, J., editors, *Coastal Altimetry*, chapter 4, pages 61–101. Springer-Verlag.

Haigh, I. D. (2017). Tides and water levels. In Carlton, J., Jukes, P., and Choo, Y. S., editors, *Encyclopedia of Maritime and Offshore Engineering*, chapter 4, pages 57–70. John Wiley & Sons, Ltd.

Hartmann, T. and Wenzel, H.-G. (1995). The HW95 tidal potential catalogue. *Geophysical Research Letters*, 22(24):3553–3556.

Hayne, G. S. (1980). Radar altimeter mean return waveforms from near-normal-incidence ocean surface scattering. *IEEE Transactions on Antennas and Propagation*, 28:687–692.

Heij, C., De Boer, P., Franses, P. H., Kloek, T., and Van Dijk, H. K. (2004). Least squares in matrix form. In *Econometric Methods with Applications in Business and Economics*, chapter 3, pages 118–133. Oxford University Press.

Hendershott, M. C. (1981). Long waves and ocean tides. *Evolution of Physical Oceanography*, pages 292–341.

Hitchcock, R. T. (2004). *Radio-frequency and Microwave Radiation*. American Industrial Hygiene Assn.

Huthnance, J. (1991). Physical oceanography of the north sea. *Ocean and Shoreline Management*, 16(3):199 – 231. North Sea: Environment and Sea Use Planning.

IHO (2006). Harmonic Constants product specification. Version 1.0. Tides Committee of the International Hydrographic Organization. Dated November 2006. 29 pp. *Harmonic Constants*, 1(November).

Jee, G., Lee, H.-B., Kim, Y. H., Chung, J.-K., and Cho, J. (2010). Assessment of GPS global ionosphere maps (GIM) by comparison between CODE GIM and TOPEX/Jason TEC data: Ionospheric perspective. *Journal of Geophysical Research: Space Physics*, 115(A10).

King, M. A. and Padman, L. (2005). Accuracy assessment of ocean tide models around antarctica. *Geophysical Research Letters*, 32(23).

Knudsen, P. and Andersen, O. (2002). Correcting grace gravity fields for ocean tide effects. *Geophysical Research Letters*, 29(8):19–1–19–4.

Koch, K.-R. and Kusche, J. (2002). Regularization of geopotential determination from satellite data by variance components. *Journal of Geodesy*, 76(5):259–268.

Kowalik, Z. and Polyakov, I. (1998). Tides in the sea of okhotsk. *Journal of Physical Oceanography*, 28(7):1389–1409.

Kowalik, Z. and Proshutinsky, A. Y. (1993). Diurnal tides in the arctic ocean. *Journal of Geophysical Research: Oceans*, 98(C9):16449–16468.

Lago, L. S., Saraceno, M., Ruiz-Etcheverry, L. A., Passaro, M., Oreiro, F. A., DOnofrio, E. E., and Gonzalez, R. A. (2017). Improved Sea Surface Height From Satellite Altimetry in Coastal Zones: A Case Study in Southern Patagonia. *IEEE Journal of Selected Topics in Applied Earth Observations and Remote Sensing*, 10(8):3493–3503.

Landskron, D. and Böhm, J. (2018). VMF3/GPT3: refined discrete and empirical troposphere mapping functions. *Journal of Geodesy*, 92(4):349–360.

Lauffenburger, D. and Dedon, P. (2006). 20.400J Perspectives in Biological Engineering. Massachusetts Institute of Technology: MIT OpenCourseWare. License: Creative Commons BY-NC-S.

Le Provost, C. (2001). Ocean tides. In Fu, L. and Cazenave, A., editors, *Satellite Altimetry and Earth Sciences*, chapter 6, pages 267–303. Academic Press, San Diego.

Marcos, M., Calafat, F. M., Llovel, W., Gomis, D., and Meyssignac, B. (2011). Regional distribution of steric and mass contributions to sea level changes. *Global and Planetary Change*, 76(3):206 – 218.

Morrow, R., Blumstein, D., and Dibarboure, G. (2018). Fine-scale altimetry and the future swot mission. In Chassignet, E., Pascual, A., Tintoré, J., and Verron, J., editors, *New Frontiers in Operational Oceanography*, pages 191–226. GODAE OceanView.

Müller, F. L., Dettmering, D., Bosch, W., and Seitz, F. (2017). Monitoring the arctic seas: How satellite altimetry can be used to detect open water in sea-ice regions. *Remote Sensing*, 9(6).

Müller, M., Cherniawsky, J. Y., Foreman, M. G. G., and von Storch, J.-S. (2014). Seasonal variation of the M2 tide. *Ocean Dynamics*, 64(2):159–177.

Munk, W. H. and Cartwright, D. E. (1966). Tidal Spectroscopy and Prediction. *Philosophical Transactions of the Royal Society A: Mathematical, Physical and Engineering Sciences*, 259(1105):533–581.

NASA (2013). Topex/poseidon fact sheet.

Obligis, E., Desportes, C., Eymard, L., Fernandes, M., Lázaro, C., and Nunes, A. L. (2011). Tropospheric corrections for coastal altimetry. In Vignudelli, S., Kostianoy, A. G., Cipollini, P., and Benveniste, J., editors, *Coastal Altimetry*, chapter 6, pages 147–176. Springer-Verlag.

Passaro, M. (2015). Design, validation and application of a new coastal altimetry strategy. PhD thesis, Faculty of Natural and Environmental Sciences School of Ocean and Earth Science, Southampton, UK.

Passaro, M., Cipollini, P., and Benveniste, J. (2015). Annual sea level variability of the coastal ocean: The Baltic Sea- North Sea transition zone. *Journal of Geophysical Research: Oceans*, pages 3061–3078.

Passaro, M., Cipollini, P., Vignudelli, S., Quartly, G. D., and Snaith, H. M. (2014). ALES: A multi-mission adaptive subwaveform retracker for coastal and open ocean altimetry. *Remote Sensing of Environment*, 145:173–189.

Passaro, M., Dinardo, S., Quartly, G. D., Snaith, H. M., Benveniste, J., Cipollini, P., and Lucas, B. (2016). Cross-calibrating ales envisat and cryosat-2 delay–doppler: A coastal altimetry study in the indonesian seas. *Advances in Space Research*, 58(3):289 – 303.

Passaro, M., Nadzir, Z. A., and Quartly, G. D. (2018). Improving the precision of sea level data from satellite altimetry with high-frequency and regional sea state bias corrections. *Remote Sensing of Environment*, 218:245 – 254.

Penrose, R. (1955). A generalized inverse for matrices. *Mathematical Proceedings of the Cambridge Philosophical Society*, 51(3):406–413.

Petit, G. and Luzum, B. E. (2010). *IERS Conventions*. Verlag des Bundesamts für Kartographie und Geodäsie, Frankfurt, Germany.

Piccioni, G., Dettmering, D., Bosch, W., and Seitz, F. (2019a). TICON: TIdal CONstants based on GESLA sea-level records from globally located tide gauges. *Geoscience Data Journal*, 6(2):97–104.

Piccioni, G., Dettmering, D., Passaro, M., Schwatke, C., Bosch, W., and Seitz, F. (2018). Coastal improvements for tide models: The impact of ALES retracker. *Remote Sensing*, 10(5).

Piccioni, G., Dettmering, D., Schwatke, C., Passaro, M., and Seitz, F. (2019b). Design and regional assessment of an empirical tidal model based on FES2014 and coastal altimetry. *Advances in Space Research, in press*.

Picot, N., Case, K., Desai, S., Vincent, P., and Bronner, E. (2012). AVISO and PODAAC User Handbook. IGDR and GDR Jason Products; SALP-MU-M5-OP-13184-CN (AVISO), JPL D-21352 (PODAAC); Physical Oceanography Distributed Active Archive Center: Pasadena, CA, USA.

Pires, N., Fernandes, M. J., Gommenginger, C., and Scharroo, R. (2019). Improved sea state bias estimation for altimeter reference missions with altimeter-only three-parameter models. *IEEE Transactions on Geoscience and Remote Sensing*, 57(3):1448–1462.

Ponchaut, F., Lyard, F., and Le Provost, C. (2001). An analysis of the tidal signal in the WOCE Sea Level Dataset. *Journal of Atmospheric and Oceanic Technology*, 18(1):77–91.

Pugh, D. and Woodworth, P. (2014a). *Sea-Level Science: Understanding Tides, Surges, Tsunamis and Mean Sea-Level Changes*. Cambridge University Press, Cambridge.

Pugh, D. and Woodworth, P. (2014b). Tidal analysis and prediction. In *Sea-Level Science: Understanding Tides, Surges, Tsunamis and Mean Sea-Level Changes*, pages 60–96. Cambridge University Press, Cambridge.

Raney, R. K. (1998). The delay/doppler radar altimeter. *IEEE Transactions on Geoscience and Remote Sensing*, 36(5):1578–1588.

Raney, R. K. and Phalippou, L. (2011). The future of coastal altimetry. In Vignudelli, S., Kostianoy, A. G., Cipollini, P., and Benveniste, J., editors, *Coastal Altimetry*, chapter 20, pages 535–560. Springer-Verlag.

Ray, R., Egbert, G., and Erofeeva, S. (2011). Tide predictions in shelf and coastal waters: status and prospects. In Vignudelli, S., Kostianoy, A. G., Cipollini, P., and Benveniste, J., editors, *Coastal Altimetry*, chapter 8, pages 191–216. Springer-Verlag.

Ray, R. D. (2008). Tide corrections for shallow-water altimetry: a quick overview. Oral presentation at the 2nd Coastal Altimetry Workshop, Pisa, Italy, 6–7 November 2008.

Ray, R. D. (2013). Precise comparisons of bottom-pressure and altimetric ocean tides. *Journal of Geophysical Research: Oceans*, 118(9):4570–4584.

Ray, R. D., Eanes, R. J., Egbert, G. D., and Pavlis, N. K. (2001). Error spectrum for the global m2 ocean tide. *Geophysical Research Letters*, 28(1):21–24.

Ray, R. D. and Egbert, G. D. (2004). The Global S1 Tide. *Journal of Physical Oceanography*, 34(8):1922–1935.

Ray, R. D., Egbert, G. D., and Erofeeva, S. Y. (2005). A brief overview of tides in the indonesian seas. *Oceanography*, 18.

Ray, R. D. and Ponte, R. M. (2003). Barometric tides from ECMWF operational analyses. *Annales Geophysicae*, 21(8):1897–1910.

Ray, R. D., Rowlands, D. D., and Egbert, G. D. (2003). Tidal models in a new era of satellite gravimetry. *Space Science Reviews*, 108(1):271–282.

Ray, R. D. and Sanchez, B. V. (1989). Radial Deformation of the Earth by Oceanic Tidal Loading. *NASA Technical Memorandum*, pages 1–51.

REA-UG-PHB-7003 (2014). REAPER Product Handbook for ERS Altimetry Reprocessed Products. Mullard Space Science Laboratory (MSSL), University College Londo.

Roos, P. C., Velema, J. J., Hulscher, S. J. M. H., and Stolk, A. (2011). An idealized model of tidal dynamics in the north sea: resonance properties and response to large-scale changes. *Ocean Dynamics*, 61(12):2019–2035.

Rosmorduc, V., Benveniste, J., Bronner, E., Dinardo, S. Lauret, O., Maheu, C., Milagro, M., Picot, N., Ambrozio, A. Escolà, R., Garcia-Mondejar, A., Restano, M., Schrama, E., and Terra-Homem, M. (2016). *Radar Altimetry Tutorial*.

Ruiz Etcheverry, L. A., Saraceno, M., Piola, A. R., Valladeau, G., and Möller, O. O. (2015). A comparison of the annual cycle of sea level in coastal areas from gridded satellite altimetry and tide gauges. *Continental Shelf Research*, 92:87–97.

SALP-MU-M-OP-15815-CN (2011). *OSTM/Jason-2 Products Handbook. Issue 1, rev. 8.*

SALP-MU-M-OP-16118-CN (2018). *Jason-3 Products Handbook. Issue 1, rev. 5.*

SALP-MU-M5-OP-13184-CN (2016). *Jason-1 Products Handbook. Issue 5, rev. 1.*

Savcenko, R. and Bosch, W. (2012). EOT11a – Empirical ocean tide model from multi-mission satellite altimetry. *Deutsches Geodätisches Forschungsinstitut, Munich, Report N. 89, 49 pp. 2010.*

Schaeffer, P., Pujol, I., Faugère, Y., Guillot, A., and Picot, N. (2016). New Mean Sea Surface CNES CLS 2015 Focusing on the use of Geodetic Missions of Cryosat-2 and Jason-1. Oral Presentation at OSTST Meeting, 31 Oct.–4 Nov., La Rochelle, France.

Scharroo, R. (2018). From range retrieval to sea surface height anomaly. 11th Coastal Altimetry Workshop - coastal altimetry training. ESA/ESRIN, Frascati, Italy.

Scharroo, R., Lillibridge, J. L., Smith, W. H. F., and Schrama, E. J. O. (2004). Cross-calibration and long-term monitoring of the microwave radiometers of ERS, TOPEX, GFO, Jason, and Envisat. *Marine Geodesy*, 27(1-2):279–297.

Scharroo, R. and Smith, W. H. F. (2010). A global positioning system–based climatology for the total electron content in the ionosphere. *Journal of Geophysical Research: Space Physics*, 115(A10).

Schureman, P. (1971). *Manual of harmonic analysis and prediction of tides.* U.S. Coast and Geodetic Survey. Washington D.C., USA.

Scozzari, A., Gómez-Enri, J., Vignudelli, S., and Soldovieri, F. (2012). Understanding target-like signals in coastal altimetry: Experimentation of a tomographic imaging technique. *Geophysical Research Letters*, 39(2).

Seidelmann, P., Guinot, B., and Dogget, L. (1992). Time. In Seidelmann, P., editor, *Explanatory Supplement to the Astronomical Almanac*, chapter 2. U. S. Naval Observatory, University Science Books, Mill Valley, CA.

Shum, C. K., Woodworth, P. L., Andersen, O. B., Egbert, G. D., Francis, O., King, C., Klosko, S. M., Le Provost, C., Li, X., Molines, J.-m., Parke, M. E., Ray, R. D., Schlax, M. G., Stammer, D., Tierney, C. C., Vincent, P., and Wunsch, C. I. (1997). Accuracy assessment of recent ocean tide models. *Journal of Geophysical Research: Oceans*, 102(C11):25173–25194.

Smith, A. J. E. (1999). Application of Satellite Altimetry for Global Ocean Tide Modeling. PhD thesis. Delft University of Technology, Faculty of Aerospace Engineering, Delft, the Netherlands.

Stammer, D., Ray, R. D., Andersen, O. B., Arbic, B. K., Bosch, W., Carrère, L., Cheng, Y., Chinn, D. S., Dushaw, B. D., Egbert, G. D., Erofeeva, S. Y., Fok, H. S., Green, J. A. M., Griffiths, S., King, M. A., Lapin, V., Lemoine, F. G., Luthcke, S. B., Lyard, F., Morison,

J., Müller, M., Padman, L., Richman, J. G., Shriver, J. F., Shum, C. K., Taguchi, E., and Yi, Y. (2014). Accuracy assessment of global barotropic ocean tide models. *Reviews of Geophysics*, 52(3):243–282.

Stewart, R. H. (2004). *Introduction to Physical Oceanography*. Department of Oceanography, Texas A & M University.

Stocker, T. F., Qin, D., Plattner, G.-K., Tignor, M., Allen, S., Boschung, J., Nauels, A., Xia, Y., V., B., and P.M., M., editors (2013). *IPCC, 2013: Climate Change 2013: The Physical Science Basis. Contribution of Working Group I to the Fifth Assessment Report of the Intergovernmental Panel on Climate Change*. Cambridge University Press.

Tamura, Y. (1987). A harmonic development of the tide-generating potential. *Bulletin d' Informations Maries Terrestres*, 99(99):6813–6855.

Taylor, J. R. (1997). *An Introduction to Error Analysis*. University Science Books, 2nd edition.

Teague, W. J., Perkins, H. T., Hallock, Z. R., and Jacobs, G. A. (1998). Current and tide observations in the southern yellow sea. *Journal of Geophysical Research: Oceans*, 103(C12):27783–27793.

Teisseyre, R. (2013). *Gravity and Low-Frequency Geodynamics*. Physics and Evolution of the Earth's Interior. Elsevier Science.

Teunissen, P. and Amiri-Simkooei, A. (2008). *Variance component estimation by the method of least-squares.*, pages 297–330. Springer, Berlin, Germany.

Tran, N., Vandemark, D., Chapron, B., Labroue, S., Feng, H., Beckley, B., and Vincent, P. (2006). New models for satellite altimeter sea state bias correction developed using global wave model data. *Journal of Geophysical Research: Oceans*, 111(C9).

Treccani (2017). Marea. In *Enciclopedia Treccani*. Istituto Treccani della Enciclopedia Italiana.

Van de Geer, S. A. (2005). Least squares estimation. In *Encyclopedia of Statistics in Behavioral Science*. American Cancer Society.

Wahr, J. M. (1985). Deformation induced by polar motion. *Journal of Geophysical Research: Solid Earth*, 90(B11):9363–9368.

Wenninger, M. (2014). *Spherical Models*. Dover Publications.

Wenzel, H.-G. (1997). Tide-generating potential for the earth. *Tidal Phenomena*, 66:9–26.

Wilkin, J. L., Arango, H. G., Haidvogel, D. B., Lichtenwalner, C. S., Glenn, S. M., and Hedström, K. S. (2005). A regional ocean modeling system for the long-term ecosystem observatory. *Journal of Geophysical Research: Oceans*, 110(C6).

Woodworth, P. L., Hunter, J. R., Marcos, M., Caldwell, P., Menéndez, M., and Haigh, I. (2017). Towards a global higher-frequency sea level dataset. *Geoscience Data Journal*, 3(2):50–59.

Wooldridge, J. (2008). *Introductory Econometrics: A Modern Approach*. ISE - International Student Edition. Cengage Learning.

Zahel, W. (1995). Assimilating ocean tide determined data into global tidal models. *Journal of Marine Systems*, 6(1):3 – 13. Data Assimilation in Manine Science.